Haptic Control for Low-cost Remotely Operated Vehicles (ROVs)

By

Khoa Duy Le, M.Sc. (Mechatronics)

National Centre for Maritime Engineering and Hydrodynamics

Australian Maritime College

Submitted in fulfilment of the requirements for the degree of Doctor of Philosophy

University of Tasmania

March 2016

DECLARATIONS

Declaration of Originality and Authority of Access

This thesis contains no material which has been accepted for a degree or diploma by the University or any other institution, except by way of background information and duly acknowledged in the thesis, and to the best of my knowledge and belief no material previously published or written by another person except where due acknowledgement is made in the text of the thesis, nor does the thesis contain any material that infringes copyright.

This thesis may be made available for loan and limited copying and communication in accordance with the Copyright Act 1968.

……...

Khoa Duy Le (29/3/2016)

Statement of Published Work Contained in Thesis

The publishers of the papers comprising Chapter 2 to Chapter 4-part B hold the copyright for that content, and access to the material should be sought from the respective journals and conference proceedings. The remaining non published content of the thesis, Chapter 5, is submitted and under review, and may be made available for loan and limited copying and communication in accordance with the Copyright Act 1968.

Statement of Co-Authorship

The following people and institutions contributed to the publication of work undertaken as part of this thesis:

- Khoa Duy Le, University of Tasmania (Candidate)
- Dr Hung Nguyen, University of Tasmania (Author 1)
- Prof. Dev Ranmuthugala, University of Tasmania (Author 2)
- Dr Alexander Forrest, University of Tasmania (Author 3)

Publication list and proportion of work details:

Chapter 2-part A (Paper 1) **"Development and Control of a Low Cost Three-Thruster Remotely Operated Underwater Vehicle"** Candidate was the primary author. Author 1 and Author 2 assisted with refinement and presentation. [Candidate: 80%, Author 1: 15%, Author 2: 5%]
Chapter 2-part B (Paper 2) **"Design, Modelling and Simulation of a Remotely Operated Vehicle – Part 2"** Candidate was the primary author. Author 1 and Author 2assisted with refinement and presentation. [Candidate: 80%, Author 1: 10%, Author 2: 10%]
Chapter 3-part A (Paper 3) **"A Heading Observer for Underwater Vehicles under Roll and Pitch Fluctuation and Acceleration Disturbances using Low Cost Sensors"** Candidate was the primary author. Author 1, Author 2, and Author 3 assisted with refinement and presentation. [Candidate: 80%, Author 1: 7.5%, Author 2: 7.5%, Author 3: 5%]
Chapter 3-part B (Paper 4) **"A Self-tuning Nonlinear PID Controller for a Three-Thruster Remotely Operated Underwater Vehicle"**

Candidate was the primary author. Author 1 and Author 2assisted with refinement and presentation. [Candidate: 80%, Author 1: 10%, Author 2: 10%]
Chapter 4-part A (Paper 5) **"Haptic Driving System for Surge Motion Control of Remotely Operated Underwater Vehicles"** Candidate was the primary author. Author 1, Author 2, and Author 3 assisted with refinement and presentation. [Candidate: 80%, Author 1: 7.5%, Author 2: 7.5%, Author 3: 5%]
Chapter 4-part B (Paper 6) **"Artificial Potential Field for ROV haptic control in dynamic environment"** Candidate was the primary author. Author 1, Author 2, and Author 3 assisted with refinement and presentation. [Candidate: 80%, Author 1: 7.5%, Author 2: 7.5%, Author 3: 5%]
Chapter 5-part A (Paper 7) **"Robust Model Reference Adaptive Control for ROV Haptic Driving System"** Candidate was the primary author. Author 1, Author 2, and Author 3 assisted with refinement and presentation. [Candidate: 80%, Author 1: 7.5%, Author 2: 7.5%, Author 3: 5%]
Appendix I (Paper 8) **"Development and Modelling of a Three-Thruster Remotely Operated Vehicle Using Open Source Hardware"** Candidate was the primary author. Author 1 and Author 2assisted with refinement and presentation. [Candidate: 80%, Author 1: 15%, Author 2: 5%]

We the undersigned agree with the above stated "proportion of work undertaken" for each of the above published (or submitted) peer-reviewed manuscripts contributing to this thesis

Signed:

……...	……...
Dr Hung Nguyen	Professor Dev Ranmuthugala
Primary Supervisor	Co-Supervisor
National Centre for Maritime	National Centre for Ports
Engineering and Hydrodynamics	and Shipping
University of Tasmania	University of Tasmania

Date: …30/3/2016…

Date: …30/3/2016…

Dr Alexander Forrest

Co-Supervisor

National Centre for Maritime

Engineering and Hydrodynamics

University of Tasmania

Date: 30.03.2016

Acknowledgments

I would like to thank my supervisors Dr Hung Nguyen, Professor Dev Ranmuthugala and Dr Alexander Forrest for their support and guidance during my research project.

To my family, I will be grateful and thankful to receive the great support from my mother, my father, my brother and my wife. They always stay with me and give me the wise advices in the hardest moments. Without them, the thesis cannot be completed.

To my son, Anh Duy Le. I love you.

Abstract

Contrary to submarine control strategies, pilots of Remotely Operated Vehicles (ROVs) remain remote to the vehicle while manoeuvring and manipulating them through their surrounding environments using tele-operation technology and visual feedback interface. However, due to the lack of three-dimensional (3D) information and limitations with quality and the field vision of the cameras, ROV pilots are not always able to observe and identify external hazards purely through visual feedback, especially when ROVs operate in environments littered with obstacles, which can thus result in collisions. To avoid such occurrences, a haptic controller including a tactile user interface was developed for ROVs in order to enhance the operators' awareness of the working environment and thus improve the performances of the vehicles within such environments.

The haptic control technique developed in this project was initially examined within a simulated environment and then applied to control a low-cost open source hardware-based ROV to validate its effectiveness. In the simulation phase, the haptic control interface hardware and software, including the haptic joystick and a novel Artificial Potential Field (APF) technique was developed to assist pilots to safely manoeuvre the simulated ROV through the surrounding environment containing both static and moving obstacles. A robust adaptive control algorithm for the haptic controller was also developed to improve the performance of the haptic control system while maintaining its stability. The proposed technique was then experimentally validated by applying the haptic controller to an observation class ROV, designed and developed for this project using open source hardware and low-cost equipment. To ensure the quality of the ROV's haptic drive system, a multi-layer Kalman filter and advanced control algorithms, such as adaptive PID and robust model-based algorithms, were designed to estimate the vehicle's states and to control its surge, yaw, and heave motions based on a host-target control structure.

The experimental results show that the host-target control structure was effectively employed to collect data and control the open source hardware-based ROV in real time. Additionally, the host-target structure was able to overcome the limitation associated with the computational power of the microcontroller, allowing the programmers to develop complex algorithms to process the raw data from low-cost sensors and deal with the nonlinear characteristics of the vehicles. The ROV performances observed from both the simulations and the experimental work indicate that the multi-layer Kalman filter and the adaptive PID algorithms provide acceptable state estimation for the ROV and thus assist the pilot in adequately manoeuvring the vehicle.

The simulation results show that the proposed APF technique has the ability to model the potential risk presented by both stationary and moving obstacles. The information is fed back and used as reference signals for the force controller incorporated within the haptic joystick system to generate a haptic force, which allows the ROV pilots to 'feel' the interaction with the surrounding environment. Finally, the simulation and experimental results show that adverse effects, such as parasitic forces and instability caused by model uncertainties and time delays, were effectively mitigated by the robust adaptive force control algorithm. The results and the findings show that haptic technology developed within this project is suitable to assist ROV pilots to safely control the vehicle within hazardous environments.

Table of Contents

List of Figures

List of Tables

Nomenclature

$\mathbf{C}(\mathbf{v})$	Coriolis matrix
C_D	Drag coefficient of the ROV body
$\mathbf{D}(\mathbf{v})$	Damping matrix
F_D	Drag force
F_{haptic}	Haptic force
f_{vir}	Virtual force presented by obstacles
$\mathbf{G}(\boldsymbol{\eta})$	Restoring force matrix
g	Gravity constant
i_a	Electrical armature current
$\mathbf{J}_\Theta$	Transformation matrix
K_t	Torque constant
K_b	Electromotive force constant
K_p	Proportional gain
K_i	Integral gain
K_d	Derivative gain
L_a	Electric inductance
$\mathbf{M}$	Inertial matrix
$\mathbf{P}_{\mathbf{APF}}(d_i, v_i)$	Artificial potential field vector
p, q, r	Angular velocities
Q	Torque of motor

R_a	Electric resistance
T	Thrust matrix
x, y, z	Body axis Cartesian coordinates in the x,y,z-direction
$X_{\dot{u}}$, $Y_{\dot{v}}$, $Z_{\dot{w}}$	Added mass coefficients
X_u, Y_v, Z_w	Linear damping coefficients
$X_{u\|u\|}$, $Y_{v\|v\|}$, $Z_{w\|w\|}$	Nonlinear damping coefficients
u, v, w	Linear velocities
ϕ, θ, ψ	Roll, pitch, yaw angle
ρ	Fluid density
ω	Rotational speed of DC motor

Abbreviations

AMC	Australian Maritime College
APF	Artificial Potential Field
AUV	Autonomous Underwater Vehicle
CFD	Computational Fluid Dynamics
DOF	Degree of Freedom
FCM	Fuzzy C-means
IMU	Inertial Measurement Unit
KF	Kalman Filter
LR	Learning rate
MRAC	Model Reference Adaptive Control
NED	North-East-Down
PID	Proportional-integral-derivative
QFT	Quantitative Feedback Theory
RMRAC	Robust Model Reference Adaptive Control
ROV	Remotely Operated Vehicle
UUV	Unmanned Underwater Vehicle
VR	Virtual Reality

Chapter 1 Thesis Introduction

The ocean is considered to encompass significant resources that can be utilised to meet the need of humans. However, there are many barriers that prevent humans from directly accessing these resources such as high surrounding water pressure, extreme temperatures, uncertain water currents, excessive operation depths, underwater obstacles, etc. A tool used in the exploration and exploitation of underwater resources is Remotely Operated Vehicles (ROVs), which can assist humans in accessing areas that are difficult and dangerous for divers or manned vehicles to operate. ROVs are remotely controlled by human with the help of tele-communication links through either a tether (e.g. fibre optic cables) or wireless control (e.g. high frequency transmission in air or acoustic transmission in water), with significant development in the science and technology related to the vehicles. Control stations of ROVs are relatively diverse depending on the scale and complexity of the vehicle, specific operational environments and mission requirements. They can be suitcase-sized control boxes with buttons, joysticks, and a monitor (**Fig. 1.1a**) for small observation class ROVs or multi-display control cabins that require multiple pilots to operate and manoeuvre heavy work-class vehicles (**Fig. 1.1b**).

a. ROV control box b. ROV control cabin

Fig. 1.1 Control device for small and large scale ROVs (Seabotix, 2013)

Generally, driving ROVs is complex due to highly nonlinear performance characteristics of the vehicles and external environmental disturbances such as the surrounding water current, the influence of surface waves, water temperatures and pressure variations. All of these factors will influence the performance of the vehicle thus requiring ROVs to be equipped with adequate sensors to provide information on the vehicles status and environmental conditions. Additionally, ROV pilots need to be sufficiently skilled in order to accurately interpret the information provided by the sensors and control the vehicle to successfully complete mission objectives. The development of these skills requires a

multi-phase training regime, which includes understanding of the behaviour and response of the vehicle that is best provided through real time operation of the vehicle.

1.1 Problem definition

To reduce the workload of ROV pilots during real-time operations and improve the reliability of ROV control systems, modern ROVs have incorporated closed-loop control to assist in manoeuvrability of the vehicle while experiencing external disturbances. The general structure of the closed-loop control is shown in **Fig 1.2**, consisting of three main systems: (1) guidance, (2) navigation, and (3) control systems. ROV driving commands generated by pilots in the guidance system are transmitted to the control system along with feedback states of ROVs obtained by the navigation system. Errors between the desired states, derived from the commands and the feedback states, are utilised within the control system to compute suitable control signals for the ROV thrusters to drive the vehicle along the commanded path.

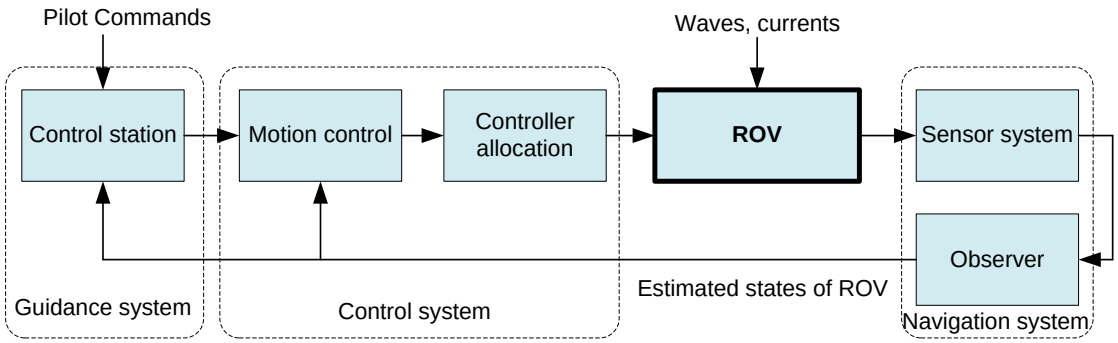

Fig. 1.2. The overview of closed-loop control strategy of ROVs (Fossen, 2011)

Closed-loop control enables manoeuvring of ROVs in response to commanded performance changes, while adequately reducing the effects of external disturbances. The performance of such a control depends on operator control, which generally includes visual feedback through on-board cameras. As a result of the lack of three dimensional information through this feedback mechanism, and limitations with quality and the field-of-vision of the cameras, ROV pilots are not always able to observe and identify external hazards purely through visual feedback, especially when ROVs operate in environments littered with obstacles, which can result in collision and mission failure.

A potential solution to augment tele-operations is to add one or more feedback senses, besides visual feedback, to assist pilots to safely manoeuvre through the surrounding hazards. One option is to include a tactile user interface that would enhance operator awareness of the working environment to improve performance. This is particularly true in the domain of collision avoidance. The virtues of a tactile user interface are that it allows pilots to 'feel' as if they are directly interacting with the surrounding environment. This technique is commonly known as haptic control and it has been widely

applied in tele-operation control systems for mobile robots, simulation training, and robotic manipulators (**Fig. 1.3**).

a. Control an excavator (Gatech) b. Interaction with virtual object (Sensable.com)

Fig. 1.3. Applications of haptic technology

Rösch et al. (2002) proposed a haptic interface for mobile robot controllers, which consisted of a force feedback joystick and ultrasonic sensors to create a force feedback loop. As the robot moves closer to an obstacle, the joystick actuators generate a force inversely proportional to the distance to the obstacle in order to warn the operator of the proximity to it and prevent collision. Ryu (2010) similarly fabricated a 6-DOF haptic master joystick for tele-operation of a mobile manipulator robot. Others (e.g. Brandt and Colton, 2010; Lam et al., 2009; and Lee et al., 2013) developed haptic collision avoidance systems for quadrotor aerial vehicles. For underwater vehicles, Zhenying (2012) proposed the use of haptic feedback to control a biomimetic fish robot. The work combined kinematic modelling and Computational Fluid Dynamics (CFD) analysis to provide force feedback to pilots enabling them to 'feel' the forces acting on the robot body and establish the field distribution maps such as velocity and pressure. Based on this previous research, haptic control has the ability to provide ROV designers with an advanced tool to improve the control of ROV operations, especially in low visibility and cluttered working environments. With tactile interaction, ROV operators have an ability to identify threats such as unexpected obstacles, enabling them to take appropriate action to avoid collision and improve mission outcomes.

1.2 Objectives and research questions

The aim of this research project is to make the driving task safer for operations of low-cost observation class ROVs. It is proposed to incorporate haptic technology into the ROV driving system to provide the pilots with additional information about the working environment, for example unexpected obstacles and water currents. Based on the generated tactile forces, ROV pilots are able to make decisions and provide appropriate commands to ensure the safe and efficient operations. The proposed driving system, including the motion and force feedback control, is illustrated in **Fig. 1.4**.

The former ensures that the ROV follows the commands given by the pilots, while the latter provides the tactile sensing feedback. Hence, ROV pilots are able to simultaneously give commands to ROVs and perceive the external environment via tactile feedback.

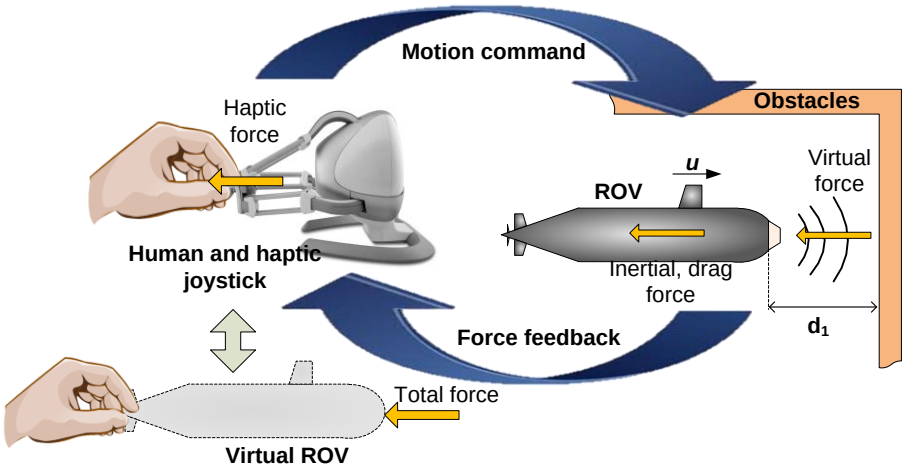

Fig. 1.4. ROV driving system employing haptic technology

The research objective is split into two research questions below:

(1) How to develop an accurate and fast responsive control system for the ROV which is based on open source hardware and equipped with low-cost devices?

(2) How can haptic technology be incorporated into a ROV joystick control to give a tactile feedback on the surrounding environment to the ROV operator?

The related research outcomes are:

- a reliable and flexible ROV control structure using open source hardware which assists designers to easily implement control algorithms to manipulate the ROV in real time;
- an effective signal processing algorithm to extract useful information from the raw data of low-cost sensory systems that are adversely affected by the noise and external disturbances;
- a motion control algorithms which provides responsive performance of the ROV, enabling pilots to effectively manoeuvre the vehicle within high disturbance environments;
- a haptic joystick system with the ability to provide information with regard to the ROV's surrounding environment to pilots via tactile sensation;
- a solution to detect potential threats to ROV's operations including both stationary and moving obstacles, and represent them under a risk avoidance vector form using haptic feedback information; and
- an effective haptic control algorithm which has the ability to provide high quality and robust haptic force performance for ROV systems with highly nonlinear characteristics, time delays, and external disturbances.

1.3 Methodology

1.3.1 Development of low-cost ROVs

In this research, both numerical and experimental approaches are utilised to develop the controller for a low-cost ROV system. The numerical approach consists of a simulation program based on the mathematical model of the ROV. Although validation is required, the main advantage of this approach is that it provides a good understanding of the performance of an ROV without the need for the physical model. In addition, various control algorithms can be tested using the simulation program before they are applied to the actual system. Data from the sensor system are combined with the mathematical model based predictive results to improve the accuracy of the data as well as to reduce noise. The research process is as listed below.

- Numerical approach consisting of:
    - establishing the mathematical model of the ROV with the hydrodynamic parameters obtained from Computational Fluid Dynamic (CFD) and analytical methods;
    - developing the control algorithm based on the mathematical model for surge, heave, and yaw motion control; and
    - employing the simulation to optimise the control parameters of the proposed algorithm.
- Experimental approach consisting of:
    - developing the ROV hardware system consisting of the control unit and a low-cost sensor system;
    - developing the observer algorithm to process the data from the low-cost sensors; and
    - conducting free running tests to validate the control algorithm derived through the numerical simulations.

1.3.2 Development of haptic control

To provide the tactile sensing feedback to the pilot, a haptic joystick was developed and incorporated into the ROV driving system in this research. The main part of the joystick is a force generating structure, which includes actuators, sensor systems, and force controllers. This structure converts the workspace information, i.e. the distance from obstacles and force imposed on the ROV body, into repulsive forces to be 'felt' by the ROV pilots (i.e., resistance on the joystick itself). Due to the 'real' feelings of external forces to the vehicle, pilots can make better informed decisions in real time control. The haptic joystick development process includes three steps below:

- to fabricate the haptic joystick by incorporating actuators into a conventional joystick;
- to develop an artificial potential field which replicates potential risks presented by underwater obstacles in the vicinity of the ROV; and

- to develop the robust adaptive control algorithm for haptic force control by analysing the uncertainty and time-delay effects of the ROV haptic driving system.

1.4 Novel aspects

There are two areas in which the project provides original contribution:

(1) A reliable low-cost solution for ROV control system

Contrary to previous low-cost ROV prototypes (e.g. OpenROV of openrov.com and BlueROV of bluerobotics.com), this project applies host-target control structure so that the computational workload of the ROV control process is distributed among on-board controller using open source hardware and an onshore computer. Such a strategy ensures that the real time constraints are met and that the use of computational resources is improved. Due to these merits, a novel sensor processing algorithm, namely two-layer Kalman filter, is developed based on low-cost sensors to reduce effects of external disturbances on the feedbacks signals; and an adaptive Proportional-Integral-Derivative (PID) control algorithm is used to control the motion of ROV in surge, heave, and yaw. The experimental results indicate that the proposed control structure can be used as a reference for future low-cost ROVs.

(2) A haptic driving system for collision avoidance task in dynamic environments

Although haptic technology has been widely applied in various applications such as simulation training, virtual reality, and endoscopic surgery, there is very little evidence showing that it has been applied to control ROVs. This work is a pioneering study that investigates the ROV haptic driving interface, including Artificial Potential Field (APF) techniques and robust adaptive force control algorithms, to assist the pilot to avoid obstacles. The APF technique, which is capable of modelling the risk presented by both stationary and moving obstacles, enables ROV pilots to enhance their awareness of the working environment and improve performance. The associated robust adaptive force control algorithm improves the transparent characteristics of the haptic performance while maintaining the stability of the entire system.

1.5 Closed-loop ROV control system

The general structure of the closed-loop control was given earlier in **Fig 1.2**. It consists of three main parts: guidance, navigation, and control systems, which are explained below.

- **The guidance system** converts pilot commands to the reference path, trajectory, or velocity that the ROV is required to follow. Generally, an interface of the guidance system includes monitor (see **Fig 1.5**) that display visual feedback captured from on-board cameras and data from on-board sensors detailing the states of ROVs such as heading, depth and position. ROV pilots interpret the

information and drive ROVs using a combination of touch displays, joystick, gamepad, and/or switching panels (Scaradozzi Conte & Sorbi, 2012).

Fig. 1.5. A typical ROV control interface (Fossen, 2011)

- **The navigation system** uses inputs from the sensor system to determine the states of the ROV, i.e. position, attitude, velocity, and acceleration. Several commonly used sensors include Inertial Measurement Unit (IMU, consisting of accelerometers and gyroscopes), digital compass, pressure sensor, and acoustic sensor (positioning system). The raw data from the sensor system are processed by the observer block to eliminate noise and extract meaningful information, which is then sent to the guidance and control system.

  Band-pass filter is one of the simplest strategies to purify sensor reading by retaining data whose frequencies within a certain range and attenuating noise whose frequencies outside that range. Due to the simplicity of application, this filter is extensively used in ROV sensory system (Christ & Wernli, 2013). Recursive filters, such as Kalman filter (Blain, Lemieux, & Houde, 2003; Steinke & Buckham, 2005), and Particle filter (Bo, Blanke, & Skjetne, 2012; McVicker et al., 2012), are also widely applied since they can reconstruct unmeasured states and remove white noise from the estimated states. Additionally, recursive filters have ability to combine readings from various sensor types, such as Inertial Navigation Systems (INS), Doppler Velocity Logs (DVL) and Ultra-short Based Line (USBL) systems, to improve the quality of data (Morgado, Oliveira, Silvestre, & Fernandes Vasconcelos, 2014; Snyder, 2010).

  To reduce the time required for the iteration process of the recursive algorithms Kinsey el al (2014) adopted a nonlinear observer derived from the Lyapunov stability condition to the ROV navigation system. Their experimental comparison between the nonlinear observer and an extended Kalman filter showed that the former provided superior performance with higher accuracy and convergence rate. In general, choosing the proper filter/observer algorithm for ROV navigation mainly depends on the characteristics of the sensory system, the requirement of data feedback quality, and the computational resources of the control unit.

- **The control system** receives the reference or desired commands from the guidance system and the current states from the navigation system. It is then able to determine the necessary forces or moments by the ROV thrusters to eliminate the error between desired commands and feedback data. Most control algorithms can be classified into three main categories: Proportional-Integral-Derivative (PID), modern (robust and adaptive algorithm), or intelligent controllers.

  Due to the simplicity of design, many ROVs utilise traditional PID controllers as the main controlling algorithm. Hoang and Kreuzer (2007) proposed a combination of linear Proportional Derivative (PD) and adaptive controllers for a six degree-of-freedom (6-DOF) work class ROV. In their work the traditional PD controller was improved so that it was able to adjust in line with the dynamic position of the ROV. To overcome large disturbance from the external environment and uncertain parameters in the dynamic model, Conte and Serrani (1998) proposed a robust control algorithm. They employed the scheduling of linear H infinity to the closed loop system enabling the ROV to operate in a broad range of working conditions. Feng and Allen (2004) decided to reduce the order of the H infinity control to make the controller simpler. They also presented the trade-off between the controller order and the performance of the closed loop system.

  Recently, intelligent control systems have been developed and widely applied to underwater systems (Antonelli & Chiaverini, 2003; Javadi-Moghaddam & Bagheri, 2010; Wang & Lee, 2003). Unlike modern controllers, where the design processes rely on the mathematical model of the dynamic system (i.e. of the underwater vehicle), which is hard to accurately model, intelligent algorithms generate the control law based on experiences and learning capability, leading to more reliable performance and higher adaptation in various working environments.

1.6 Thesis outline

The thesis is comprised of six chapters, where the cores (Chapters 2 to 5) are based on papers that have previously been published or are currently under review. The details of each of the chapters are presented below.

Chapter 1: The introductory chapter provides information on the background to the problem, identifying the research questions and the related objectives leading to the solution methodology and outlines the structure of the thesis. The chapter also provides a brief review of previous research with regard to ROV control systems and haptic technology clarifying the relevant architecture.

Chapter 2: Presents the development of a low-cost three-thruster ROV. Based on open source hardware, the host-target control structure is proposed to collect data from the ROV sensors and

provide control signals to the ROV thrusters. Free running tests, including surge, heave, and yaw motion control, were conducted to test the stability of the control structure and evaluate the associated performance. In addition, the kinematics and kinetics mathematical models of the ROV were investigated. The parameters of the mathematical models were identified to develop a virtual reality ROV simulation model used in Chapter 3, 4 and 5.

Chapter 3: Introduces the raw signal processing strategy and develops the adaptive control algorithm for the vehicles. The quality of the sensor feedback plays a crucial role in ROV controlling and the low-cost sensors used in the three-thruster ROV are extremely sensitive to noise and disturbances from the surrounding environment, such as waves and unexpected water currents. To overcome this, a novel observer is proposed consisting of two Kalman filter (KF) steps: one for acceleration elimination and the other for roll and pitch fluctuation compensation. After eliminating the noise and disturbances from the sensor feedback, a suitable control algorithm was developed for the ROV. This consists of a self-tuning nonlinear PID controller, which mimics the principle of neural cells whose parameters have the ability to adapt to the uncertainty of the controlled system. To validate the proposed technique, the novel self-tuning nonlinear PID algorithm was applied to control a simulated ROV developed in Chapter 2 within a virtual reality environment. The findings of this chapter including data processing and control algorithms are used to provide more accurate and faster responsive motion controllers incorporated within the ROV's haptic driving system in subsequent chapters.

Chapter 4: Presents the development of a haptic joystick and a novel Artificial Potential Field (APF) technique for a haptic controller of an underwater ROV to assist the pilot to avoid underwater obstacles. The APF technique is used to replicate potential risks presented by underwater obstacles in the vicinity of the ROV. Based on the APF technique, a risk avoidance vector is calculated and transmitted to a haptic joystick to generate the tactile feedback, which enables the ROV pilot to be alerted of potential dangers due to surrounding obstacles. This prompts the pilot through the joystick to avoid the dangers and safely navigation the vehicle. The novel APF technique can deal with both stationary and moving obstacles as it is combined with an obstacle motion detection algorithm based on Fuzzy C-Means (FCM) and Kalman Filter (KF) algorithms. These algorithms are applied to process raw data from the scanning sensors to identify the relative positions and velocities between the ROV and the obstacles, which are employed within the APF calculations. To validate the proposed technique, the haptic joystick and the novel APF formula were applied to control a simulated ROV developed in Chapter 2 within a virtual reality environment. The findings of this

chapter provide the basis and support for the robust adaptive control design process developed in Chapter 5.

Chapter 5: Presents the development of a novel robust adaptive control algorithm for a haptic controller of an ROV to deal with uncertainty, nonlinear characteristic of the system, and time delays caused by data transmission. These factors can adversely affect the performance of the haptic control, including transparency and stability, resulting in inaccurate manoeuvring of the ROV, which in extreme cases can lead to obstacle collision. The proposed control algorithm is able to address these issues by combining a robust control technique, known as the Quantitative Feedback Theory (QFT), and the Model Reference Adaptive Control (MRAC) algorithm, providing robust and responsive performance to the haptic drive system. Simulations and free running tests using the three thruster ROV developed in Chapter 2 were conducted to verify and validate the performance. Comparisons with other controllers, such as PID algorithms, were also made to verify the effectiveness of the proposed algorithm.

Chapter 6: This provides an overall summary of the project and concludes on the findings of the individual chapters, as well as discussing the implications and limitations of the research. Several future research directions are also discussed.

Appendices:

Appendix I - conference paper supporting the content of Chapter 2.

Appendix II - electronic configuration of the ROV.

Appendix III - control interface and virtual reality setup.

Appendix IV - ROV haptic drive system.

Chapter 2: Development of Low-cost ROVs based on Open Source Hardware

This chapter consists of two parts in which two low-cost ROV, namely AMC-ROV-IV and AMC-ROV-V are alternately presented. Whereas part A describes the hardware equipment and the free running tests conducted in AMC survival centre pool using AMC-ROV-IV, part B puts more focus on the development of the mathematical model of AMC-ROV-V and the simulation programs within virtual reality environments.

Chapter 2 - Part A: Development and Control of a Low Cost, Three-Thruster, Remotely Operated Underwater Vehicle

This subchapter has been published in International Journal of Automation Technology. The citation for the research article is

Le, KD and Nguyen, HD and Ranmuthugala, D, *Development and control of a low-cost, three-thruster, remotely operated underwater vehicle*, International Journal of Automation Technology, 9, (1) pp. 67-75. ISSN 1881-7629 (2015)

Chapter 2 - Part B: Design, Modelling and Simulation of a Remotely Operated Vehicle – Part 2

This subchapter has been published in Journal of Computer Science and Cybernetics. The citation for the research article is

Le, KD and Nguyen, HD and Ranmuthugala, D, *Design, modelling and simulation of a remotely operated vehicle - Part 2*, Journal of Computer Science and Cybernetics, 30, (2) pp. 106-116. ISSN 1813-9663 (2014)

Abstract

This paper is a continuity of the previously published Part 1 (Nguyen et al., 2013) and focuses on hardware and Virtual Reality (VR) model development of a three-thruster Remotely Operated Vehicle (ROV). The project included setting up an on-board electronic system with the associated suite of sensors and the required communication protocol. This system utilises a host-target structure, which consists of an onshore station computer and an on-board open source microcontroller. To improve the controllability of the driving system, a VR model of the ROV was developed to reflect the altitude and attitude of the physical vehicle. By using the feedback signals from the sensors, the VR model operates in a similar manner to the actual vehicle. Hence, it provides the operator with the capability to monitor the ROV operation within a virtual environment and enables the operator to control the ROV based on the visual inputs and feedback. Finally, real time simulations were carried out to validate the interaction between the ROV operator and the VR model. To provide realistic operational conditions, the effects of sensor noise and water current disturbances were included to the simulation programme. Results show that the performance of the VR ROV is stable even with these disturbances.

Keywords. Underwater vehicle, open source hardware, virtual reality model

2B.1 Introduction

Remotely Operated Vehicles (ROVs) used in the maritime industry are Unmanned Underwater Vehicles (UUVs) that are controlled by human input, usually via signal transmission cables, from control stations that are remote to the vehicle. Currently ROVs are used in the maritime industry for a diverse range of functions, including seabed and subsea exploration, underwater inspections, maintenance operations, security tasks, and defence activities. These ROVs are able to replace humans to carry out missions in hostile and hazardous underwater environments. However, controlling ROVs is not a straightforward task due to the highly nonlinear characteristics of the vehicles and external disturbances from the environment, such as water current, waves, temperature, and pressure that will influence the performance of the vehicle. In the past a number of algorithms have been proposed by researches to meet the control requirements, with some well-known examples given below.

Smallwood & Whitcom have proposed a combination between linear Proportional Derivative (PD) control and adaptive control for a six degree-of-freedom (6-DOF) ROV(Smallwood & Whitcomb, 2004). Besides linear approaches, intelligent control has also been widely applied to UUVs. For examples, Marzbanradand Kamali studied the robust adaptive fuzzy sliding mode for trajectory tracking(Marzbanrad, Eghtesad, & Kamali, 2011), while Ken et al. implemented fuzzy to develop a docking guidance system for an ROV operating in ocean currents(Ken et al., 2012).

In this project the ROV system described in Part 1 of this paper is modified and upgraded (Nguyen et al., 2013). The sensors systems including the Inertial Measurement Unit (IMU), magnetometer,

pressure sensor, etc., are installed on the ROV frame to acquire the states of the vehicle. The sensor data is collected by an Arduino board, a low cost open sources on-board electronics system. The low cost system can be developed on a personal computer or laptop using readily available peripheral devices such as a serial communication board and a microcontroller, thus easily lending itself for undergraduate student projects.

In order to improve the controllability of the driving system, a Virtual Reality (VR) model of the ROV was developed to simulate the behaviour of the vehicle to the different control algorithms (Gracanin, Valavanis, Tsourveloudis, & Matijasevic, 1999; Lin & Kuo, 1998). Based on the feedback signal from the sensor system, the VR model operates exactly in a similar manner to that of the actual vehicle. To validate the interaction between operators and the VR model, real time simulations were carried out using the relevant mathematical models. The 6-DOF vehicle model was developed using the appropriate kinetics, which included hydrodynamic and inertia coefficients obtained using a combination of experimental, analytical, and Computational Fluid Dynamics (CFD). In order to provide the effects of a typical marine environment, sensor noise and water currents were added to the simulation programme. Kalman filters and closed-loop control algorithms were utilised within the simulation to improve the controllability of the driving system.

2B.2 ROV system upgrade

2B.2.1 Control hardware

The ROV, namely AMC-ROV-V shown in **Fig. 2B.1**, is developed as a test vehicle for this project. It consists of a frame constructed from PVC pipes and aluminium, with three waterproof dc motor driven propellers, each having a maximum thrust force of 8N, providing two propulsion thrusters and one vertical thruster.

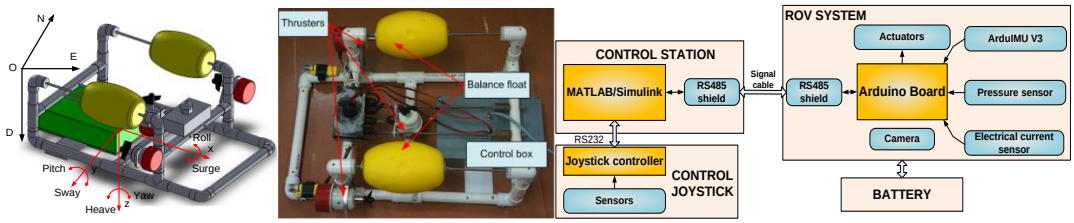

(a) Reference frames (b) Actual ROV (c) Structure of ROV control system

Fig. 2B.1 AMC-ROV-V system and control structure

The control structure of the ROV is shown in **Fig. 2B.1**, consisting of 3 main parts: ROV controller (on-board system), control station (onshore system) and joystick controller.

The operations of the first part are governed by the main Arduino Mega 2560 board. This microcontroller board is connected with the peripheral sensors such as an IMU, digital magnetometer and pressure sensor, which provide the states of the vehicle including acceleration, rotational rate,

depth, and direction. All information from the sensors is gathered by the Arduino microcontroller and sent to the control station via a RS-485 serial communication device at the baud rate of 115200bps. The main control algorithm within the station computer receives and processes the raw data, combining with the driving commands from the joystick to generate control signals to be sent back to the microcontroller via the transmission cable to activate the relevant thrusters. Thus, the microcontroller is required to have only one fixed program to carry out the mission, while the control algorithms, which require higher computational power, are developed and reside within the onshore computer.

The main advantage of the master-slave control structure is the flexibility. It is easier to modify the control algorithm in the station computer than to re-program the microcontroller inside the ROV. In addition, the proposed control structure can be considered as a low cost solution for ROV control, as it does not require any special devices such as embedded computers with high standard I/O interface cards. Complex algorithms can be developed within the onshore computer.

The resolution of the gyroscope and accelerometer within the IMU can be defined by modifying the value in the registers of the microprocessor. The measureable range and the resolution of the sensors on the AMC-ROV-V used in this project are given in **Table 2B.1**.

Table 2B.1 Sensors of the AMC-ROV-V

Sensor	Measureable range	Resolution
Gyroscope	$\pm$ 250^o/s	16 bit
Accelerometer	$\pm$ 2g	16 bit
Magnetometer	$\pm$ 1.3 gauss	12 bit
Pressure sensor	0 to 75psi	10 bit

2B.2.2 ROV and thruster modelling

In order to verify the control algorithm effects of the external disturbances due to the ocean currents were considered. The velocity vector of the irrational currents is defined as $\boldsymbol{v}_c = [u_c, v_c, w_c, 0, 0, 0]$ with the assumption that the vertical disturbances are neglected. The kinetic equation of the ROV including the current disturbance in (Fossen, 2011) can be re-written as,

$$\mathbf{M}\dot{\mathbf{v}}_\mathbf{r} + \mathbf{C}(\mathbf{v}_\mathbf{r})\mathbf{v}\mathbf{r} + \mathbf{D}(\mathbf{v}_\mathbf{r})\mathbf{v}_\mathbf{r} + \mathbf{G}(\eta) = \mathbf{T}, \tag{2B.1}$$

where *M, C, D, G* and *T* are the inertial, Coriolis, damping, restoring force and thrust matrices, respectively, and $\boldsymbol{v}_r$ defined as $\boldsymbol{v}_r = \boldsymbol{v} - \boldsymbol{v}_c$ is the relative velocity vector . The details of these matrices can be referred to (Fossen, 2011).

In AMC-ROV-V, the three thrusters consist of dc motors connected directly to propellers. Since the speed of an armature controlled dc motor is dependent on the armature voltage V_a, the differential equations of a dc motor are given by,

$$\frac{d}{dt}\begin{bmatrix}\omega \\ i_a\end{bmatrix} = \begin{bmatrix}-\frac{b}{I} & \frac{K_t}{I} \\ -\frac{R_a}{L_a} & -\frac{K_b}{L_a}\end{bmatrix}\begin{bmatrix}\omega \\ i_a\end{bmatrix} + \begin{bmatrix}0 \\ \frac{1}{L_a}\end{bmatrix}V_a + \begin{bmatrix}-\frac{1}{I} \\ 0\end{bmatrix}Q \quad . \tag{2B.2}$$

The parameters in Equation (2B.2) are defined in Nomenclature.

Based on the rotational speed of the motor shaft and the relative speed of the ROV, the advance ratio J_o for the ROV is obtained by,

$$J_o = \frac{u_r}{\rho D \omega |\omega|} \tag{2B.3}$$

where u_r , D and ρ are surge velocity, propeller diameter and fluid density, respectively.

Fossen (2011) showed that the thrust K_T and torque K_Q coefficients have a linear relationship to J_o. Thus, these coefficients are calculated using the following formulae,

$$K_T = \alpha_1 J_o + \alpha_2;\ K_Q = \beta_1 J_o + \beta_2, \tag{2B.4}$$

where α_i and $\beta_i\,(i = 1,2)$ are four non-dimensional constants, which are determined from experiments. Next, thrust *T* and torque *Q* are calculated from the rotational speed of the motor shaft as,

$$T = \rho D^4 K_T(J_o)\omega|\omega|;\ \ Q = \rho D^5 K_Q(J_o)\omega|\omega|, \tag{2B.5}$$

where *Q* is a propeller torque generated by the dc motor described in Equation (2B.2).

2B.2.3. Re-estimating the hydrodynamic coefficients

Due to the modification of the ROV frame, the CFD analysis and added mass calculation were conducted to re-estimate the coefficients of the system. Thus the coefficients in Part 1 of the paper (Nguyen et al., 2013) were modified as shown in **Table 2B.2**.

Table 2B.2 Estimated ROV coefficients

Coef	Value	Coef	Value	Coef	Value	Coef	Value
L	480mm	b	290mm	$Y_{\dot{v}}$	-2.322 kg	$Y_{v\|v\|}$	-19.37 kgm^{-1}
m	3.2 kg	I_x	0.091 kgm^2	$Z_{\dot{w}}$	-2.56 kg	$Z_{w\|w\|}$	-24.6 kgm^{-1}
I_y	0.153kgm^2	z	75mm	$K_{\dot{p}}$	-0.045 kgm^2	$K_{p\|p\|}$	-0.081kgm
B (Buoyancy force)	32.5N	l_1	0mm	$M_{\dot{q}}$	-0.068 kgm^2	$M_{q\|q\|}$	-0.26kgm
l_2	50mm	l_3	180mm	$N_{\dot{r}}$	0.038 kgm^2	$N_{r\|r\|}$	-0.198kgm
x_b	0mm	y_b	0mm	X_u	-0.65 kgs^{-1}	K_p	-0.029$kgms^{-1}$
z_b	0.07m	K	0.373Nm/V	Y_v	-0.73 kgs^{-1}	M_q	-0.075$kgms^{-1}$
$X_{\dot{u}}$	-1.536kg	$X_{u\|u\|}$	-12.6kgm^{-1}	Z_w	-0.75 kgs^{-1}	N_r	-0.052$kgms^{-1}$

2B.3. Control structure and ROV states observation

2B.3.1 Control structure

In Section 2, the complete dynamic model of the ROV was developed, with the voltages to the thruster motors as inputs and the ROV performance as outputs. This section will introduce the control algorithm for trajectory tracking, which is defined by the waypoints summarised in **Fig. 2B. 2**.

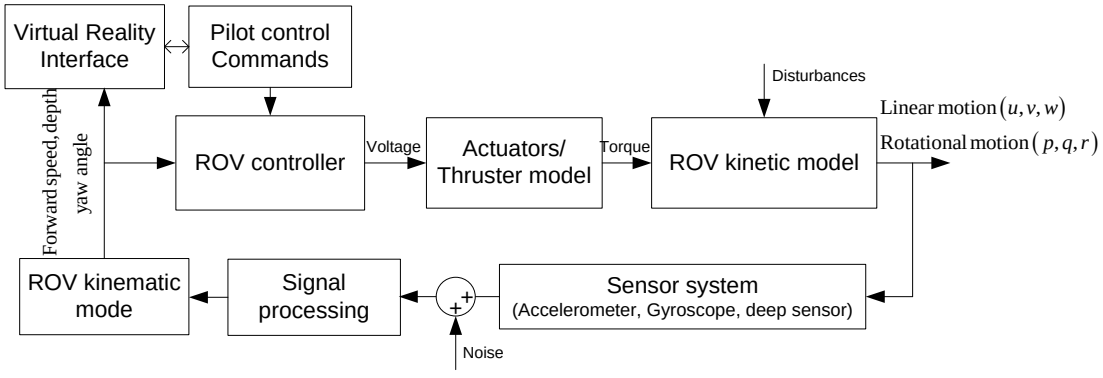

Fig. 2B.2 Control diagram of ROV system

The closed loop control system consists of the ROV model, the controller, and signal processing. The ROV operator gives the commands to the system via the multi-DOF joystick. The controller synthesises the operator's control commands and the feedback data to generate the appropriate control voltages for the thrusters, which provide the thrust forces to drive the ROV in accordance with the desired motions. The states of the vehicle is obtained by the sensors and filtered by a signal processing algorithm to eliminate random noise. These filtered signals are used for the next control iteration and the virtual reality monitor.

2B.3.2 Kalman filter for estimating ROV states

The Kalman filter is an efficient recursive filter that estimates the state of a linear or nonlinear dynamic system from a series of noisy measurement. In this project, the speeds and accelerations of the ROV are acquired by the 6-DOF IMU sensor, with the signals including noise and bias. By fusing the estimated velocities with the data from sensor system, a Kalman filter reduces the variation of the noise, thus providing a 'cleaner' and improved feedback signal to the controller. In this paper, the surge, yaw rates and depth are estimated using a Kalman filter.

2B.3.2.1 Estimation of surge, heave and yaw velocities

The estimated model and observation equation are presented as,

$$\dot{\mathbf{x}}_\mathbf{s} = \mathbf{A}\cdot\mathbf{x}_\mathbf{s} + \mathbf{B}(\mathbf{T}) + \mathbf{w}_\mathbf{noise};\ \ \mathbf{y}_\mathbf{s} = \mathbf{H}\cdot\mathbf{x}_\mathbf{s} + \mathbf{z}_\mathbf{sensor} + \mathbf{v}_\mathbf{noise}, \tag{2B.6}$$

where

$\boldsymbol{x}_\mathbf{s}$: state vector which includes the surge, heave velocity and yaw rate $\boldsymbol{x}_\mathbf{s} = [u_r \quad v_r \quad r_r]^T$

$\mathbf{B}(\mathbf{T})$: torque matrix whose values are estimated in the section below

$\boldsymbol{w}_{noise}$: process noise which is assumed to be a zero mean Gaussian white noise process with covariance matrix $\mathbf{Q}_\mathbf{noise} = \begin{bmatrix} Q_u & 0 & 0 \\ 0 & Q_w & 0 \\ 0 & 0 & Q_r \end{bmatrix}$

H : observer vector

$\mathbf{z}_\mathbf{sensor}$: state vector from the sensors

$\mathbf{v}_\mathbf{noise}$: noise vector whose covariance matrix is R.

Matrix *A* in equations (6) can be derived from the kinetic equations of the ROV in equation (2B.1) as follows:

$$\mathbf{A} = \mathbf{M}^{-1}\left[-\mathbf{C}(\mathbf{v}) - \mathbf{D}(\mathbf{v})\right];\ \mathbf{B}(\mathbf{T}) = \mathbf{M}^{-1}\mathbf{T}, \tag{2B.7}$$

Step 1: Define the initial state vector and covariance matrix as,

Covariance matrix of error $\mathbf{P}(0)=\mathbf{E}\left[\left(\mathbf{x}_s(0)-\hat{\mathbf{x}}_s(0)\right)\left(\mathbf{x}_s(0)-\hat{\mathbf{x}}_s(0)\right)^{\mathbf{T}}\right]$. (2B.8)

Initial state vector $\hat{\mathbf{x}}_s(0)=[\hat{u}(0) \quad \hat{w}(0) \quad \hat{r}(0)]^T$. (2B.9)

Step 2: Calculate the Kalman gain as,

$$\mathbf{K}(\mathbf{t})=\mathbf{P}(\mathbf{t})\cdot\mathbf{H}^{\mathbf{T}}\left(\mathbf{H}\cdot\mathbf{P}(\mathbf{t})\cdot\mathbf{H}^{\mathbf{T}}+\mathbf{R}\right)^{-1}, \tag{2B.10}$$

with $\mathbf{K}(t)=\left[K_1(t) \quad K_2(t)\right]^T$.

Step 3: Estimate state propagation by updating the new state vector as per the following formula,

$$\dot{\hat{\mathbf{x}}}_s(t)=\mathbf{A}\cdot\hat{\mathbf{x}}_s(t)+\mathbf{B}(\mathbf{T}(t))+\mathbf{K}(t)\left[\mathbf{y}_s(t)-\mathbf{C}\cdot\hat{\mathbf{x}}_s(t)\right], \tag{2B.11}$$

$$\hat{\mathbf{x}}_s(t)=\hat{\mathbf{x}}_s(t-1)+\dot{\hat{\mathbf{x}}}_s(t)dt. \tag{2B.12}$$

Step 4: Update error covariance matrix for the new iteration as,

$$\dot{\mathbf{P}}(t)=\mathbf{A}\cdot\mathbf{P}(t)+\mathbf{P}(t)\cdot\mathbf{A}^{\mathbf{T}}+\mathbf{Q}-\mathbf{P}(t)\cdot\mathbf{H}^{\mathbf{T}}\cdot\mathbf{R}^{-1}\cdot\mathbf{H}\cdot\mathbf{P}(t), \tag{2B.13}$$

$$\mathbf{P}(t)=\mathbf{P}(t\text{-}1)+\dot{\mathbf{P}}(t)dt. \tag{2B.14}$$

The loop is repeated from Step 2 until the end of the operating process.

2B.3.2.2 Estimation of the thrust force

It can be seen that the thrust forces are required as input variables for the ROV state estimation algorithm. These parameters cannot be measured directly, thus, in this section, an observer is developed to estimate the thrust forces from the measurable variables.

From equation (2B.2) the relationship between the input voltage V_a and torque Q is expressed as,

$$\frac{K_t}{L_aI}V_a=\ddot{\omega}+\left[\frac{R_a}{L_a}+\frac{b}{I}\right]\dot{\omega}+\left[\frac{R_ab}{L_aI}+\frac{K_bK_t}{L_aI}\right]\omega+\frac{1}{I}\dot{Q}+\frac{R_a}{L_aI}Q. \tag{2B.15}$$

To shorten the above equation, the parameters are redefined as follows,

$$b_1=\frac{K_t}{L_aI}V_a;\ a_1=\left[\frac{R_ab}{L_aI}+\frac{K_bK_t}{L_aI}\right];\ a_2=\left[\frac{R_a}{L_a}+\frac{b}{I}\right];c_1=\frac{R_a}{L_aI};\ c_2=\frac{1}{I}. \tag{2B.16}$$

Replacing the newly defined parameters in Equation (15) yields the following relationship,

$$b_1V_a=\ddot{\omega}+a_2\dot{\omega}+a_1\omega+c_2\dot{Q}+c_1Q. \tag{2B.17}$$

As previously mentioned, the parameters of a dc motor are known, except for the torque disturbances Q due to the environment. Thus, the observer is designed as,

$$b_1 V_a = \ddot{\hat{\omega}} + a_2\dot{\hat{\omega}} + a_1\hat{\omega} + c_2\dot{\hat{Q}} + c_1\hat{Q}, \tag{2B.18}$$

where $\hat{\omega}$ and $\hat{Q}$ are the rotational speed and estimated torque of the numerical actuator model respectively.

As shown in Section 2B.3, the resistant torque Q on the motor shaft has a linear relationship with the thrust force. Therefore, the thrust force T can be indirectly estimated from the torque Q. The error between the estimated rotational rate ($\hat{\omega}$) and the real rotational rate (ω), given in (2B.17) and (2B.18) respectively, must be minimised. According to (Srisertpol & Khajorntraidet, 2009), the following update rules were applied to satisfy this condition,

$$\frac{d^2\hat{Q}}{dt^2} = -\gamma_2 \dot{e}_\omega c_2;\ \frac{d\hat{Q}}{dt} = -\gamma_1 \dot{e}_\omega c_1. \tag{2B.19}$$

Thus, the formulae representing the thrust force observation are presented as follows:

$$\dot{\hat{Q}}(t) = -\dot{e}_\omega(t)(\gamma_1 c_1 + \gamma_2 c_2);\ \hat{Q}(t) = \hat{Q}(t-1) + \dot{\hat{Q}}(t). \tag{2B.20}$$

Substituting the estimated value of the resistant torque into Equation (2B.5), the torque coefficient is calculated as,

$$\hat{K}_Q = \frac{\hat{Q}}{\rho D^5 \omega|\omega|}. \tag{2B.21}$$

From Equation (2B.4), the advance ratio is derived as,

$$\hat{J}_o = \frac{\hat{K}_Q - \beta_2}{\beta_1}. \tag{2B.22}$$

Substituting $\hat{J}_o$ into Equations (2B.4) and (2B.5), the estimated propeller thrust ($\hat{T}$) is obtained.

2B.4. Virtual reality simulation

2B.4.1 Virtual reality environment

Based on mathematical models that describe the relationships between the inputs and outputs, the VR system generates a similar performance to that of the physical system and provides the user with a realistic interaction experience. In this paper, a virtual ROV model is developed based on the hydrodynamic coefficients which are identified in **Table 2B.2**. Based on the performances of the virtual model, the control system is evaluated and improved to meet the desired outcomes. A by-product is that a VR system is also a low cost operator training solution, which is based on easily

accessible and relatively affordable equipment. Due to the ability to mimic the behaviour of the actual vehicle and its environment, VR provides operators with a realistic operating environment to prepare them for actual missions.

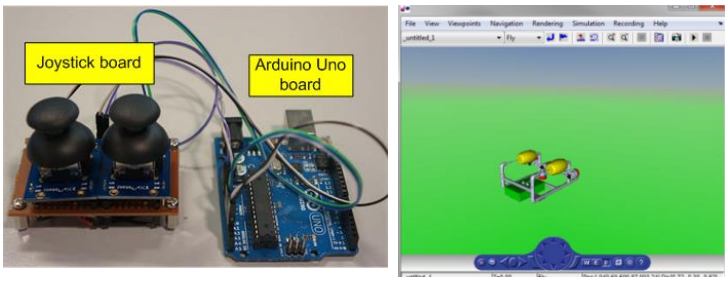

Fig. 2B.3 Control joystick and ROV model in a virtual environment

The dynamic model in Equation (2B.3) and the parameters in **Table 2B.2** are used to develop the relationships between the input thruster forces and the output ROV speeds. The mathematical model of the thruster motors given in Equation (2B.4) is applied and linked directly to the ROV dynamic model. In addition, an analogue joystick (**Fig. 2B.3**) using an Arduino controller was built and combined with the VR programme through a serial communication port.

2B.4.2 Simulation results

The driving joystick system (**Fig. 2B.3**) was 'plugged' into and combined with the simulation programme. As the pilot pulls or pushes the button, the output voltage of the joystick is interpreted as the speed command and is used as the input for closed loop controller. For simplicity, the conventional PID control law was used to generate the control signal for the system as,

$$V_a = K_p e(t) + K_i \int e(t)\,dt + K_d \frac{\mathrm{d}e(t)}{dt}, \tag{2B.23}$$

where V_a is the control signal, $e(t)$ is the error, and K_p, K_i and K_d are the proportional, integral and derivative control gains, respectively. In this simulation, the PID gains are set as: $K_p=10$, K_i =5 and $K_d=0$.

In order to test the robustness of the control system a medium range water current was included using the following random disturbance current profiles,

$$\frac{d\mathbf{v}_c}{dt} = -\mathbf{v}_c + Br_{noise}, \tag{2B.24}$$

where r_{noise} is white noise, whose mean and variance are 0 and 0.2, respectively, and B is the parameter that identifies the range of the disturbance (B=1).

In the study, an ROV operator attempts to control the ROV to follow the rectangular trajectories, which are predefined by the waypoints shown in **Fig. 2B.4**. It is seen from the simulation results that

the basic form of the desired path is achieved regardless of the effects from the external disturbance and sensor noise. The responses of the forward speed, yaw rate and depth are shown in **Fig. 2B.5**, from whose first three graphs it is seen that with the designed closed loop control system, the ROV is able to accurately follow the commands giving by the operator. The steady state errors between the reference values and the ROV responses are small (less than 5%), and there is no significant overshoot at any point due to the high damping effect of the surrounding water.

There is the difference between the actual and the estimated forces due to the errors within the dc motor mathematical model. These errors lead to an unreliability of the results obtained from the ROV mathematical model. In addition, the raw data from the sensor also contain a white noise (0 mean and 0.05 variance) to simulate the performance of the actual sensors. However, by combining these two data sources, one from the ROV model and the other from the sensor system, the covariance of errors are significantly reduced, with the effects of sensor noise mitigated so that the feedback data are smoother than the raw signal which is directly measured from the sensors (comparison of the red and the blue/dot lines in **Fig. 2B.5**). It proves that good feedback signals can be obtained by using Kalman filters, thus reducing the effect of noise and mathematical model uncertainty in order to improve the ROV performance.

From the three last graphs of **Fig. 2B.5**, it is seen that the under-actuated motions of the ROV are affected by the water current disturbances, centripetal force, Coriolis force, etc. The 2D trajectory graph shows that the water current disturbance in the sway direction distorts the path of the ROV. Because the number of actuators is less than the degrees of freedom, the ROV operator has to compensate for the path deviation by manipulating the heading angle of the ROV (yaw controller) in order to keep tracking the pre-defined waypoints.

The pitch and roll angles are caused by the coupling effect between the surge motion and centripetal force. These angles cannot be controlled by the actuators, and are automatically restored to the equilibrium position by the righting moments created by the buoyancy and gravity forces. The pitch and roll fluctuation amplitudes dictate the stability characteristic of the vehicle, thus these angles must be kept as small as possible. The response of the pitch motion (**Fig. 2B.5**) shows that this angle is proportional to the forward speed. This is due to the thruster generating the moments as the vehicle moves forward, resulting in the pitch of the vehicle. In addition, the lift forces generated on the vehicle frame due to the forward motion contributes to the pitching moment. This is partially verified when noting that the pitching moment is a function of the forward speed. At the surge speed of 0.5 m/s, the pitch and roll angles are small and the equilibrium position is easily maintained by the restoring forces. Thus, the ROV system is stable and safe within the operating range speed.

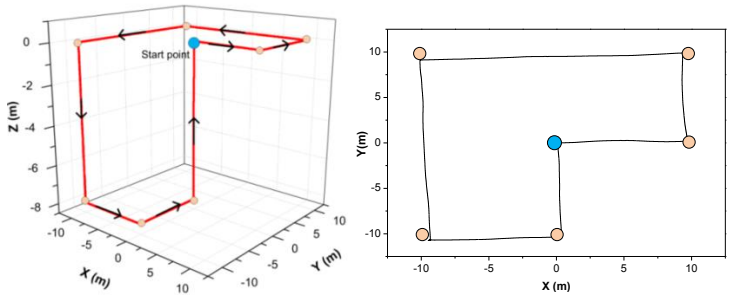

Fig. 2B.4 3D and 2D trajectory performance of the ROV control by joystick

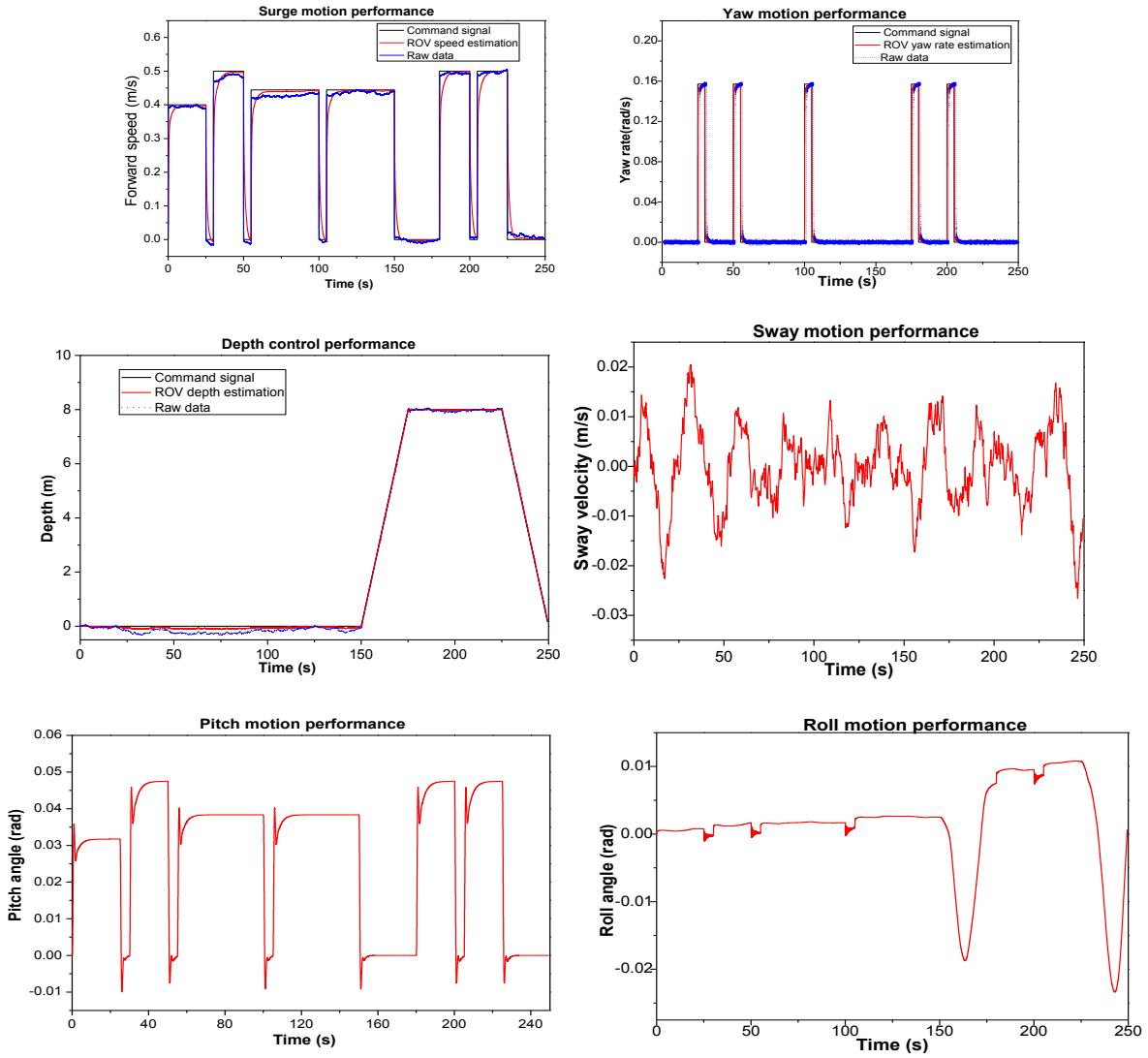

Fig. 2B.5 ROV responses

2B.5. Conclusions

This paper presented the development of the hardware and the associated control algorithm for a low cost ROV. The open source Arduino electronic controller was utilised as the main on-board control unit. By connecting with various peripheral devices such as the IMU, pressure sensor, and motor drivers,. the Arduino controller collected the relevant data from the ROV sensors and directed them to

the onshore station computer. The data is processed by the advanced Kalman filter algorithm to reduce the influence of any external disturbances and noise, and then combined with the ROV operator's commands to generate the required control signals. In addition, a Virtual Reality (VR) model of ROV was developed to display the behaviour, spatial location, and attitude of the vehicle based on the feedback data. This effectively improves the controllability of the vehicle, as the operator can directly observe the performance of the ROV through different view-points and provide the required inputs to maintain the required trajectory. The simulations conducted were also able to validate the interaction between the operator using the thumb joystick and the response of the VR model. The closed loop control system was designed for surge rate, yaw rate and depth control. It facilitates the operating process by linearizing the relationship between the joystick signal and the ROV velocity. The simulation results have shown that the closed loop system is stable in the operating scenario, even with the existence of sensor noise and external environmental disturbances.

Further work is required to verify the performance of the vehicle by conducting free running model tests to evaluate the performance of the physical system under varying operational conditions. This will enable the VR model to be compared against the physical model for validation, thus providing a versatile design tool that can assist in the training of ROV operators.

Chapter 3: Sensor Signal Processing and Advanced Control Algorithms

Based on AMC-ROV-IV presented in previous chapter, Chapter 3 investigates the signal processing and develops the advanced control algorithm to manoeuvre the ROV. The first part of this chapter presents the heading estimation algorithm namely two-layer Kalman filter to eliminate noise and disturbances from the reading of sensors including an inertial sensor and a digital compass. And the second part focuses on the development of an adaptive PID control algorithm which is able to improve the performance of the ROV.

Chapter3 - Part A: A Heading Observer for Underwater Vehicles under Roll and Pitch Oscillations and Acceleration Disturbances using Low-Cost Sensors

This subchapter has been published in International Journal of Ocean Engineering. The citation for the research article is:

Le, KD and Nguyen, HD and Ranmuthugala, D and Forrest, A, *A heading observer for ROVs under roll and pitch oscillations and acceleration disturbances using low-cost sensors*, Ocean Engineering: An International Journal of Research and Development, 110 pp. 152-162. ISSN 0029-8018 (2015)

Abstract

This paper presents the development of a heading angle observer for Underwater Remotely Operated Vehicles (ROVs) during dynamic conditions in the presence of roll/pitch oscillation and acceleration disturbances. Unlike previous algorithms, which focused on deep water working environments where the external accelerations and oscillation were rather small, this paper proposes a heading observer that deals with the effects of near surface working conditions on ROVs, such as waves or unexpected water currents. These effects cause significant roll and pitch disturbances as well as high-acceleration drift motions, which affect the measurements from the incorporated sensor system. To overcome this situation, a novel heading observer is proposed, consisting of two Kalman filter (KF) steps: one for acceleration elimination and one for roll and pitch oscillation compensation. The data from the inertial measurement unit and the magnetometer are combined to estimate and compensate for external accelerations and roll/pitch disturbances by adjusting the covariance values. Free running tests, based on a physical ROV model, were conducted under various working environments to verify the performance of the proposed observer. The comparison with previous algorithms was also made to verify the effectiveness of the proposed algorithm.

Keywords –ROV, Kalman filter, heading observer, inertial sensor, magnetometer

3A.1 Introduction

ROVs are used extensively in the exploration of ocean resources. They enable humans to investigate in deep and hostile underwater environments without physically having to enter those environments. Developing effective control for a ROV is not a straightforward task due to the highly nonlinear characteristics of the vehicle model and disturbances from the external environment, such as water currents, waves, the change of temperature or pressure that influence the performance of the vehicle. One of the important issues for ROV navigation controllers is heading control. A number of projects have looked at developing effective orientation control algorithms for ROVs (Guoqing, Li, Fengshui, Qiang, & Jing, 2009; Petrich & Stilwell, 2011). One finding is that the quality of feedback signals from the ROV sensor system plays an important role in the performance of the vehicle since the signals, affected by noises, can debase the ROV control quality and even lead to instability of the system. Thus, the need to develop improved effective orientation observers for ROVs to provide accurate and robust signals (Kinsey, Eustice, & Whitcomb, 2006).

Previously, the heading control algorithms for ROVs were constructed based on the assumption that the vehicle operated in deep water where large external acceleration and oscillation were not present. Therefore, a digital compass could provide a good heading measurement for the vehicle's control algorithms. However, such systems fall short when the vehicle operates near the free surface where the effects of waves and water currents are significant. These disturbances generate large external accelerations and oscillations, which deteriorate the data of the digital compass. Thus, there is the

need for an efficient orientation observer that filters large noise and disturbances from the sensor data. Research addressing these disturbances within the aviation industry for systems such as quadrotor and vertical takeoff and landing aircraft are relatively advanced (Martin & Salaün, 2010; Roberts & Tayebi, 2013). Others have focused on the attitude estimation for all terrain vehicles by combining Global Navigation System (GPS) and Inertial Navigation Sensor (INS) data (Hua, 2010). However, similar work dealing with issues related to marine underwater vehicles and surface vessels are limited (Vasconcelos, Cardeira, Silvestre, Oliveira, & Batista, 2011). This project focuses on developing a heading observer for ROVs experiencing large external linear and rotary accelerations, including roll/pitch oscillations.

A strap-down inertial sensor, including an accelerometer and a gyroscope, and a magnetometer are the most commonly used sensors for orientation estimation of vehicles. A single sensor is not sufficient to obtain the orientation of a moving system with respect to the inertial frame because each type of sensor has its own disadvantages. For example:

- a magnetometer returns the vector direction of the magnetic field, but s vulnerable to electro-magnetic noise from the motors and will malfunction near the Earth poles;
- a strap-down accelerometer measures not only the gravitational direction but also the acceleration of the system, generated by actuators and external sources; and
- the reading from the gyroscope, especially the low-cost sensor from micro-electromechanical (MEMS) technology, contains uncertain bias resulting in boundless orientation drift errors, as the measurement errors are accumulated when the data is integrated.

Many researchers have combined these sensors and developed orientation observers for terrain and aerial vehicles. Using a complementary filter is one of the most popular techniques for sensor combination. Due to the differences of noise frequencies from the elemental sensors, the complementary filter eliminates the noise of the sensors by using different cut-off frequencies. In addition, the algorithm allows for straightforward implementation without requiring a high computational resource. Thus, the complementary filter is suitable. for small and low-cost autonomous vehicles with limited on-board power. Several authors have proposed the nonlinear complementary filter for obtaining good attitude estimations from measurements obtained from low-cost sensors that have varying biases (Mahony, Hamel, & Pflimlin, 2008; Metni, Pflimlin, Hamel, & Souères, 2006). They applied a direct complementary filter and a passive complementary filter to design a nonlinear attitude observer based on a special orthogonal group. Their algorithm is capable of dealing with high noise levels and time varying addictive biases of the inertial sensors.

The Kalman filter has also been applied to sensor fusion. The Kalman filter can be understood as an optimal recursive least square algorithm, where it minimizes the estimated error covariance by implementing the predictor-corrector process based on various data sources. Several authors have

used the Kalman filter to estimate the roll and pitch angle of their respective aerial systems by combining the feedback from the accelerometer and gyroscope (Pe et al., 2011; Warsi et al., 2014). Their algorithms are able to mitigate the effect of external acceleration during the estimation process. For ship heading control, Fossen and Perez (2009) described the application of a Kalman filter in ship motion control systems. They proved that the Kalman filter is effective in eliminating the influence of waves from the states feedback of the ship motion, especially in low frequency motion control. For three-dimensional (3D) orientation estimation, other authors utilized the Kalman filter for attitude and heading reference system (AHRS) estimation (Jung Keun & Park, 2009; Yun & Bachmann, 2006). In their proposed observers, the predicting model used the rotational rate feedback from a gyroscope as the updating data for the rotation matrix. The readings from the accelerometer and magnetometer were then utilised for correcting errors caused by the uncertain bias of the gyroscope data.

This paper proposes an orientation observer for ROVs by estimating and eliminating the external accelerations and the roll and pitch disturbances from the measurements. By using a low-cost six-axis inertial sensor and a magnetometer, an orientation observer was developed, which consists of two Kalman filter layers. The first Kalman filter layer, which is based on the algorithm proposed by Jung Keun et al. (2012), is used to estimate the roll and pitch angles by compensating for the effects of external accelerations. The estimation of roll and pitch angles are then combined with the readings from the magnetometer for heading angle calculations. The second Kalman filter layer uses the heading angle measurement from the magnetometer to correct the error emanating from the predicting model. Differing from the conventional Kalman filter, the covariance of the magnetometer adapts with the magnitude of roll and pitch disturbance. Consequently, the erratic error inherent in magnetometer readings caused by this disturbance source is eliminated from the estimated results.

This paper describes the heading estimation problem for a three-thruster ROV and proposes a heading observer based on the Kalman filter algorithm. The sensors on the ROV are analysed through experimental work to quantify their respective advantages and disadvantages for heading estimation. The two-layer Kalman filter algorithm is validated by conducting experiments using the actual ROV under various disturbance conditions to test the systems effectiveness and robustness. Finally, a comparison of the proposed and previous algorithms is presented to identify the relative merits and future work is proposed.

3A.2 Problem description

The ROV developed at the Australian Maritime College, AMC ROV-IV shown in **Fig. 3A.1**, was used in this project. The vehicle is built on an aluminium frame incorporating two control/equipment boxes, one camera housing, and three SeaBotix BTD-150DC motor-driven thrusters (two for horizontal motion and one for vertical motion).

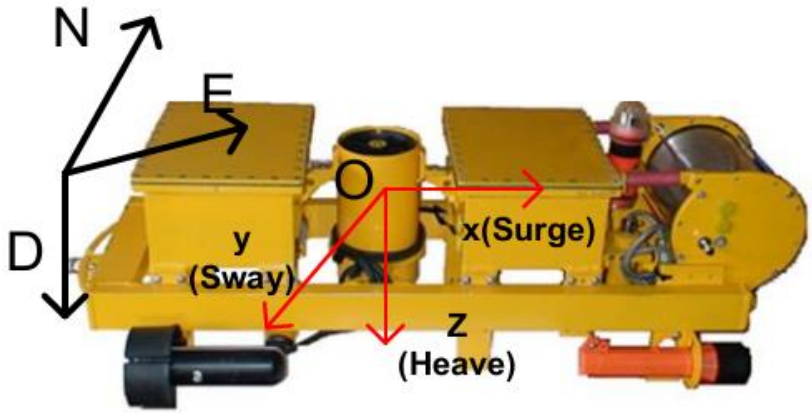

Fig. 3A.1. AMC ROV-IV, fixed frame (NED) and body frame (Oxyz)

The ROV is equipped with low-cost sensors, including an Inertial Measurement Unit (IMU) incorporating a gyroscope and accelerometers, and a 2-D magnetometer using an HMC6352 integrated circuit. The specifications of the sensors are given in **Table 3A.1**.

Table 3A.1.Sensors system of the AMC ROV-IV

Sensors	Measureable range	Resolution
Gyroscope (MPU6000 digital motion processor)	$\pm 250^{o}$/s	16 bit
Accelerometer (MPU6000 digital motion processor)	$\pm$ 2g	16 bit
Magnetometer (HMC6352 integrated circuit)	0.1 to 0.75 Gauss	12 bit

3A.2.1 Estimating the ROVs heading angle

Considering the ROV within the reference frames shown in **Fig3A.1**, the linear and angular transformation between the body and the Earth (NED) fixed coordinates systems is performed by (Thor I Fossen, 2011),

$$\dot{\boldsymbol{\eta}} = \mathbf{J}_{\Theta}(\boldsymbol{\eta})\,\mathbf{v}\,, \tag{3A.1}$$

where $\boldsymbol{\eta} = [x, y, z, \phi, \theta, \psi]^T$ is the displacement vector giving the positions in surge (x), sway (y), and heave (z) and the Euler angles roll (ϕ), pitch (θ), and yaw (ψ), $\mathbf{v} = [u, v, w, p, q, r]^T$ consists of the linear and angular velocity of the ROV in body frame, while $\mathbf{J}_{\Theta}$ is the transformation matrix defined as,

$$\mathbf{J}_{\Theta}(\boldsymbol{\eta}) = \begin{bmatrix} \mathbf{J}_1(\phi,\theta,\psi) & 0_{3\times3} \\ 0_{3\times3} & \mathbf{J}_2(\phi,\theta,\psi) \end{bmatrix}, \tag{3A.2}$$

where

$$\mathbf{J}_1(\phi,\theta,\psi) = \mathbf{R} = \begin{bmatrix} c\psi c\theta & -s\psi c\phi + c\psi s\theta s\phi & s\psi s\phi + c\psi c\phi s\theta \\ s\psi c\theta & c\psi c\phi + s\psi s\theta s\phi & -c\psi s\phi + s\theta s\psi c\phi \\ -s\theta & c\theta s\phi & c\theta c\phi \end{bmatrix} \tag{3A.3}$$

$$\mathbf{J}_2(\phi,\theta,\psi) = \begin{bmatrix} 1 & s\theta t\phi & c\phi t\theta \\ 0 & c\phi & -s\phi \\ 0 & s\phi / c\theta & c\phi / c\theta \end{bmatrix} \text{and} \tag{3A.4}$$

s = sin, c = cos, and t = tan.

The Euler angular rates are calculated by substituting equations (3A.3) and (3A.4) into (3A.1) as:

$$\begin{aligned} \dot{\phi} &= p + q\sin(\phi)\tan(\theta) + r\cos(\phi)\tan(\theta) \\ \dot{\theta} &= q\cos(\phi) - r\sin(\phi) \\ \dot{\psi} &= q\frac{\sin(\phi)}{\cos(\theta)} + r\frac{\cos(\phi)}{\cos(\theta)}, \quad \theta \neq \pm 90^{o} \end{aligned} \tag{3A.5}$$

where $[p,q,r]$ is the body-fixed angular velocity vector and measured by the gyroscope.

As the work in this paper focuses on the heading of the ROV, the first order approximation can be used to discretise equation (3A.5) as follows:

$$\psi_{t+1} = \psi_t + \Delta t\left(q_t \frac{\sin(\phi_t)}{\cos(\theta_t)} + r_t \frac{\cos(\phi_t)}{\cos(\theta_t)} \right) \tag{3A.6}$$

where Δt is the sampling time.

Equations (3A.6) clearly shows that the ROV's heading depends not only on the angular yaw velocity in Oz direction (r_t) but also on the roll and pitch angles. Therefore, the attitude of the vehicle, including the roll and pitch angle, is required in order to estimate the heading of the ROV.

The on-board gyroscope and the magnetometer can be used to measure the heading angle of the vehicle. However, the gyroscope measurement is affected by the drift because of uncertain biases, while the magnetic disturbances generated within the working environment deteriorates the quality of the magnetometer data. The oscillations in roll and pitch motions also influence the heading calculation as shown in equations (3A.6). Thus, it is required to develop a good heading observer by combining various sensors to provide an accurate estimation while mitigating the effects of the disturbances.

3A.2.2 Evaluation of sensor performances

To develop a good heading observer, a good understanding of the characteristics of the ROV sensors, including the IMU and the magnetometer is required. It is known that both these sensors have different advantages and disadvantages, which may complement each other. Thus, the next phase was to analyse the performances of these sensors based on experimental results to determine their application capability within the heading observer algorithm.

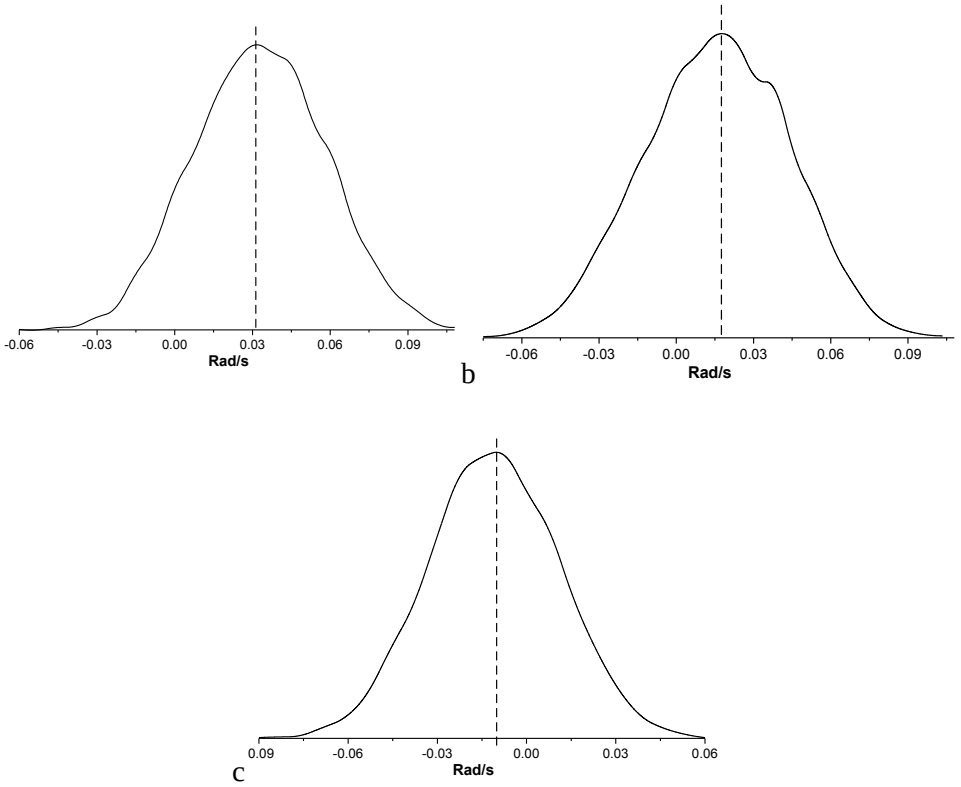

Fig. 3A.2. Noise distribution density of the 3-D gyroscope. (a) Gyroscope reading in Ox, (b) Gyroscope reading in Oy, (c) Gyroscope reading in Oz

3A.2.2.1 Gyroscope performance

Bias always exists in gyroscope measurements, especially for low-cost sensors using MEMS technology. Gyroscope biases are time-varying and influenced by a number of factors, such as ambient temperature, and therefore generate the uncertain drift when the gyroscope data is integrated with time. Thus, it was required to conducted experiments to study the characteristics and quantify the gyroscope bias. This was done by placing the ROV in a static state and recording the data from the gyroscope, with the probability density functions of the data in the three directions i.e. roll, pitch and yaw, shown in **Fig. 3A. 2**. It is seen that the distributions are bell-shaped Gaussian curves, with the mean considered as the bias of the gyroscope. The variance of the data is around 0.07 degree, which is rather small, indicating that the gyroscope can be applied to estimate the orientation of the mobile system. The integral results of the data given in **Fig. 3A. 3** show that the errors are accumulated

around 3-6 degree in 5 min. However, it is seen that the drift curves are not linear, indicating that the bias changes slowly with time. Moreover, the characteristics of the gyroscope bias can change under the variation of temperature (Jung Keun, Park, & Robinovitch, 2012). Consequently, to obtain good orientation measurements, the gyro biases have to be continuously monitored, identified, and compensated.

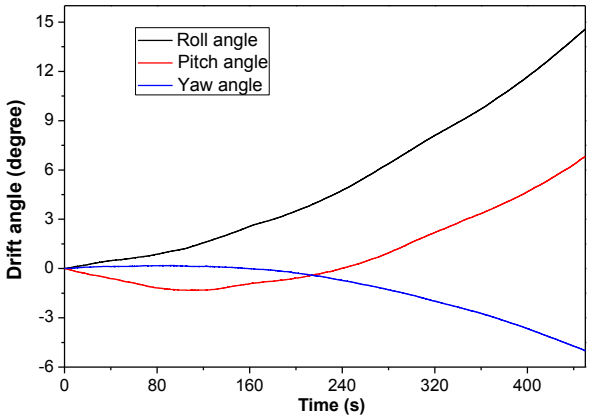

Fig. 3A.3.Drift angles obtained from the gyroscope

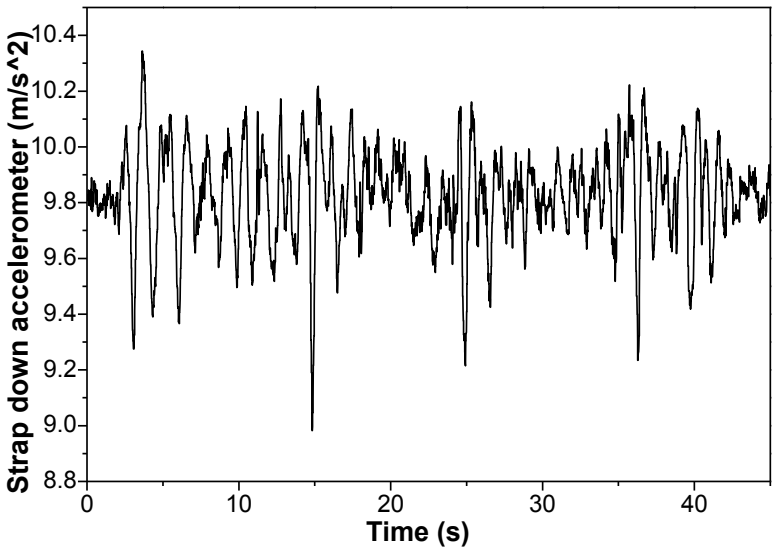

Fig. 3A.4. Acceleration disturbances

3A.2.2.2 Accelerometer and magnetometer performance

Accelerometers and magnetometers are two common sensors which are used to directly measure the orientation of moving objects. The accelerometer has the ability to provide a fixed vertical direction, which is the constant gravitational acceleration. Thus, the accelerometer is used to measure the attitude of systems, including roll and pitch angles. However, MEMS accelerometers are sensitive not only to gravity but also to the acceleration of the moving object. For this reason, the acceleration readings are affected by acceleration disturbances, generated by actuators and external effects. For

ROV systems, especially for hovering vehicles, due to the high damping forces/moments generated by interaction with the surrounding fluid, the accelerations are much smaller than the gravity constant and can be negligible. Most acceleration disturbances are generated by external sources such as water currents, vortices, and waves, and found to be significant when operation in close proximity to the free surface.

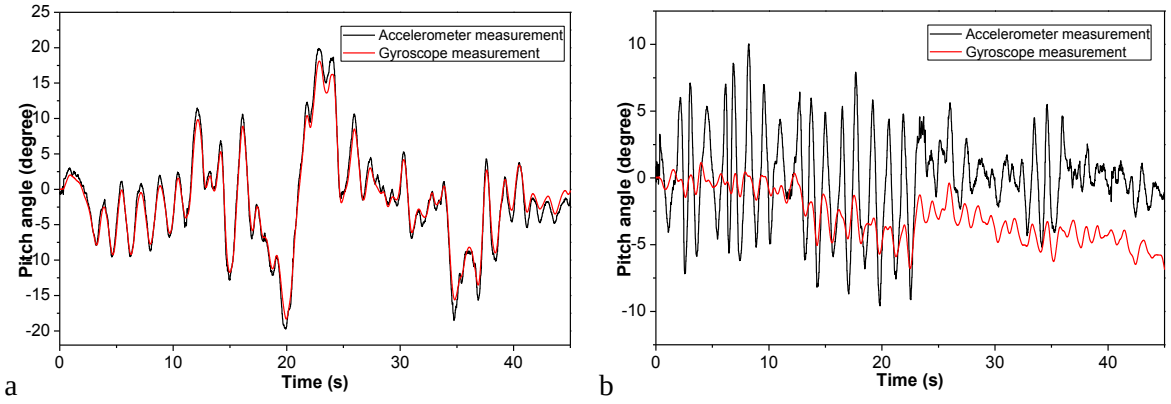

Fig. 3A.5.Pitch angle measured by gyroscope and accelerometer (a) Without disturbance (b) With disturbance

To investigate the effect of acceleration on the attitude angle estimation, experiments were conducted under two conditions, i.e. one without any acceleration disturbances and the other with the disturbances shown in **Fig. 3A.4**. Since the gyroscope is not influenced by acceleration disturbances, it can be used to verify the reading of the accelerometer in short term attitude estimation. **Fig. 3A.5**(a) shows the result of the case in which accelerations were not applied to the vehicle. It is seen that the readings from the gyroscope (red line) and accelerometer (black line) are similar, confirming that the accelerometer has the ability to provide accurate measurement for this condition. However, when random acceleration disturbances in the horizontal plane were applied to the vehicle, the data from the two sensors digress as shown in **Fig. 3A.5(b)**. The feedback from the gyroscope shows that there is little amplitude oscillation in the pitch angle, whereas the accelerometer gives significant amplitude variation. Since the gyroscope was considered unaffected by the disturbances, it is evident that the acceleration estimations are adversely affected by the external disturbances.

The magnetometer (digital compass) provides the heading measurement based on the magnetic field of the Earth. However, the sensor readings are easily affected by large disturbances which come from electronic circuits, motor coils, or even the distribution of the magnetic field. Previous research has shown that the magnetometer pitch and roll measurements are more severely affected by magnetic disturbance than yaw orientation (Young-Soo, 2010). Thus, the 2-D magnetometer, using an integrated HMC6352 circuit, is employed to measure the heading of the vehicle. In the horizontal plane, the 2-D magnetometer provides a more accurate measurement with repeatability up to 1 degree. However, when the sensor is inclined, the measurement is affected by the vertical magnetic field. The

seriousness of this effect depends not only on the roll/pitch angle, but also on the magnetic dip, which is the angle made with the horizontal by the Earth magnetic field lines. In the regions where the dip angle is large, such as near the Earth's poles, the compass measurement increases in sensitivity with the increased inclination of the vehicle.

In order to determine the accuracy of the magnetometer in heading measurements, the data from the magnetometer was compared with the vehicle's heading captured by the camera system. The experiments were conducted in the towing tank of the Australian Maritime College, where the magnetic dip is up to -71 degree, with two sets of experiments, one without any external disturbances and the other with random roll and pitch disturbances as shown in **Fig. 3A.6** applied to the ROV. The heading angle measurements obtained by the magnetometer and the actual heading angle provided by image processing for the first experiment are shown in **Fig. 3A.7(a)**. The results are very close, although the error of the gyroscope measurement increases with time due to the drift phenomenon. In the second experiment, under the influence of random roll and pitch disturbances, it is seen that the magnetometer readings are seriously affected. There are several instances that the roll and pitch angle disturbances are sufficiently large, for example from seconds 18 to 25 in **Fig. 3A.7(b)**, there is a large instantaneous errors ('jerk' phenomenon) in the data plot.

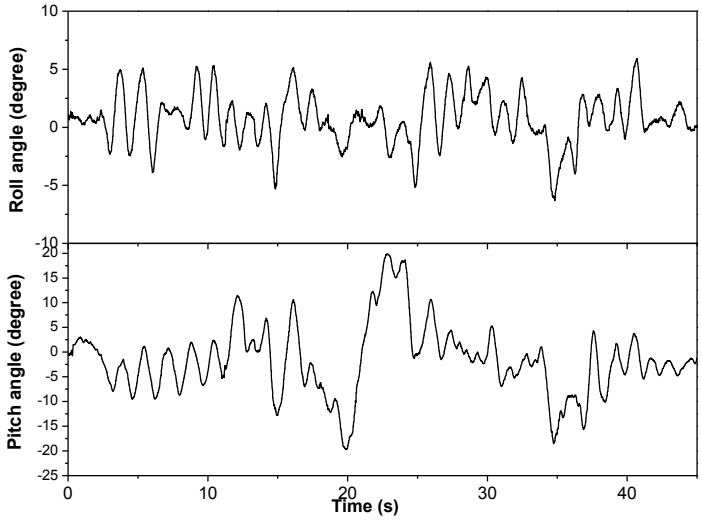

Fig3A. 6. Roll and pitch disturbances

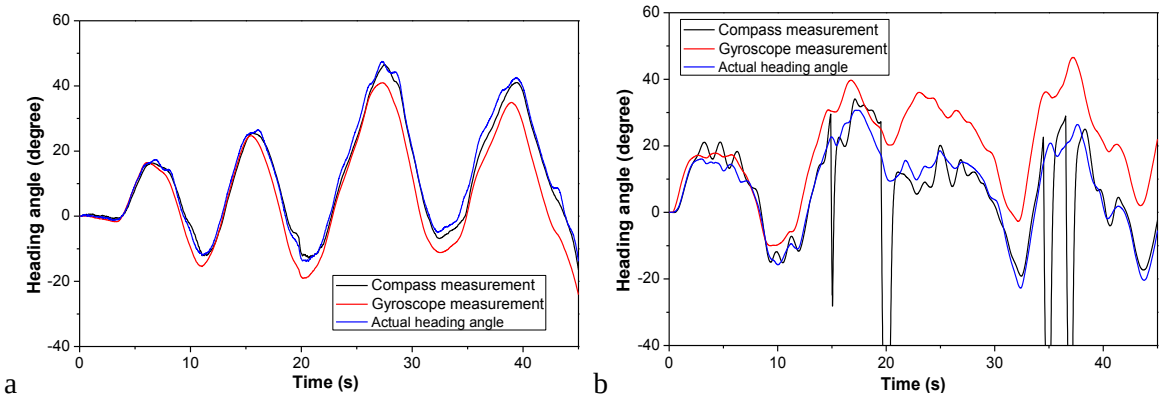

Fig. 3A. 7. Heading angle measured by compass and gyroscope (a) Without disturbance (b) With disturbance

As shown in the experimental results and the analysis above, both inertial and magnetic sensors have drawbacks which lead to inaccurate measurements. Therefore, to obtain a good heading estimation, acceleration disturbances, variant biases, and the magnetic effects have to be eliminated. The work described in this paper develops a Kalman filter-based observer, which can mitigate drawbacks of the respective sensors. The gyroscope readings are used for the prediction process input, while errors are corrected for by accelerometer and magnetometer data. In contrast to the traditional Kalman filter, the acceleration disturbances are estimated and compensated for by using the sensor readings to improve the reliability of the correction signal. In addition, the covariance value of the magnetometer is adapted to eliminate the jerk phenomenon inherent in the estimation process.

3A.3 ROV heading observer design

3A.3.1 Overview of the heading observer

As mentioned in Section 3A.2, there are three main disturbance sources which lessen the quality of heading observers: uncertain bias, external acceleration, and roll/pitch oscillations. To mitigate these effects, a novel heading observer is proposed, that consists of two extended Kalman filters. The first filter estimates the roll and pitch angles based on accelerometer and gyroscope readings, which is then passed on to the second filter. In the latter the roll/pitch results are used to calculate the heading rates and to adjust the covariance of the compass readings. Based on this data, the heading of the vehicle can be estimated. The overview of the proposed algorithm is shown in **Fig. 3A.8**.

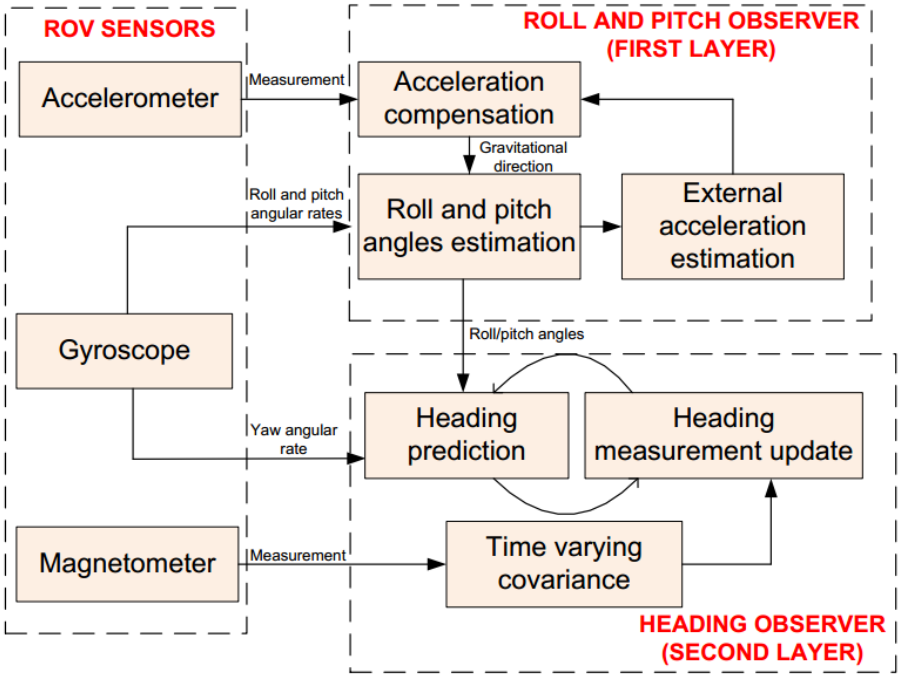

Fig. 3A.8 Overview structure of observer algorithm

The data from the gyroscope and accelerometer are used for the first filter. In a similar fashion to a traditional Kalman filter, the roll and pitch observer consists of two main processes: time update using gyroscope data and measurement update using accelerometer data. However, as shown in Section 3A.2.2, the measured update data could be inaccurate as the reading from the accelerometer includes both gravitational and vehicle accelerations. For these reasons, the disturbance acceleration compensation algorithm is added in order to reduce this effect on the observer results.

The second filter, which is also based on the Kalman filter algorithm, combines the gyroscope and the magnetometer data for heading estimation. The estimated roll and pitch results from the first filter and the yaw rate from the gyroscope are used to predict the heading of the vehicle. The error, caused by the drift phenomenon, is corrected by the magnetometer data. However, when the magnetometer data is severely affected by disturbances, the correction data from the magnetometer becomes less reliable than the prediction results. To eliminate the effects of the untrusted data, a strategy of adjusting the covariance value which reflects the reliability of the data was introduced. When a sudden change of sensor reading occurs, the covariance is increased to prevent the estimation result from the low quality data.

3A.3.2 Kalman filter for roll/pitch estimation (first layer)

To estimate the attitude of the vehicle, the reading from the gyroscope is used for the time update process, and the error caused by sensor bias is corrected for by the accelerometer data. The acceleration disturbance compensation algorithm is applied to eliminate the effect of disturbance from the sensor reading.

The measurement from the gyroscope and the accelerometer is modelled as,

$$\begin{aligned}\mathbf{y}_G &= {}^B\boldsymbol{\omega} + \mathbf{n}_G \\ \mathbf{y}_A &= {}^B\mathbf{g} + {}^B\mathbf{a} + \mathbf{n}_A\end{aligned} \tag{3A.7}$$

where ${}^B\boldsymbol{\omega}=[p \quad q \quad r]^T$ is the angular velocity in the body frame, ${}^B\mathbf{g}$ is the gravity vector with respect to the body frame, and ${}^B\mathbf{a}$, $\mathbf{n}_A$ and $\mathbf{n}_G$ are body accelerations and measurement noises of the accelerometer and gyroscope, respectively.

From the rotation matrix in equation (3A.3), it is seen that the roll and pitch angles can be calculated based on the third row of matrix $\mathbf{R}$ as follows:

Let $\mathbf{Z}=[Z_1 \quad Z_2 \quad Z_3]=[-s\theta \quad c\theta s\phi \quad c\theta c\phi]$, then,

$$\begin{aligned}&\phi = \tan^{-1}\left(\frac{Z_2}{Z_3}\right) \quad \text{and} \\ &\theta = \tan^{-1}\left(\frac{-Z_1}{Z_2/\sin(\phi)}\right).\end{aligned} \tag{3A.8}$$

The gravity vector in the body frame can be also calculated using the $\mathbf{Z}$ definition as,

$${}^B\mathbf{g} = g \times \mathbf{Z} \tag{3A.9}$$

Equations (3A.9) shows that vector $\mathbf{Z}$ is linked to both the gyroscope and accelerometer.Therefore, $\mathbf{Z}$ is used as the state vector of the Kalman filter, with the development outlined below.

Step 1: Modelling the time update process

The continuous orientation matrix update can be discretized based on a first-order approximation of a strap-down integration step as,

$$\mathbf{R}_t = \mathbf{R}_{t-1}\left(\mathbf{I} + \Delta t\tilde{\boldsymbol{\omega}}_{t-1}\right) \tag{3A.10}$$

where Δt is the sampling time;

$\tilde{\boldsymbol{\omega}}_{t-1}$ is the skew-symmetrix matrix of the vector ${}^B\boldsymbol{\omega}$, $\tilde{\boldsymbol{\omega}} = \begin{bmatrix} 0 & -r & q \\ r & 0 & p \\ -q & p & 0 \end{bmatrix}$; and

$\mathbf{R}_t$ and $\mathbf{R}_{t-1}$ are rotational matrix at t and t-1, respectively.

(Jung Keun et al., 2012)have rewritten equation (3A.10) in term of vector $\mathbf{Z}$ as,

$$\mathbf{Z}_t = \left(\mathbf{I} + \Delta t\tilde{\boldsymbol{\omega}}_{t-1}\right)^T \mathbf{Z}_{t-1} \tag{3A.11}$$

Substituting the measurement model of the gyroscope given by equation (3A.7) including noise into equation (3A.11) and expanding gives,

$$\mathbf{Z}_t = \underbrace{\left(\mathbf{I} - \Delta t \tilde{\mathbf{y}}_{G,t-1}\right)}_{\Phi_{t-1}} \mathbf{Z}_{t-1} + \underbrace{\Delta t \left(-\mathbf{Z}_{t-1}\right) \mathbf{n}_G}_{\mathbf{w}_{t-1}} . \tag{3A.12}$$

The process noise covariance of equation (3A.12) is defined by (Jung Keun et al., 2012) as,

$$\mathbf{Q}_{t-1} = E\left[\mathbf{w}_{t-1} \mathbf{w}_{t-1}^T\right] = -\Delta t^2 \tilde{\mathbf{Z}}_{t-1} \Sigma_G \tilde{\mathbf{Z}}_{t-1} \tag{3A.13}$$

where Σ_G is the covariance matrix of the gyroscope measurement noise.

Step 2: Measurement from the accelerometer

The acceleration of the ROV can be modelled as a first order low pass filter (Jung Keun et al., 2012) as,

$$\mathbf{a}_t = c_a \mathbf{a}_{t-1} + \varepsilon_t \tag{3A.14}$$

where $\mathbf{a}_t$ and $\mathbf{a}_{t-1}$ are the acceleration of the ROV in *t* and *t-1*, respectively; and

c_a is a constant which determines the cut-off frequency of the filter and ε_t is the random error of the acceleration model.

The error of the predicted acceleration is then calculated as,

$$\mathbf{a}^-_{\varepsilon,t} = \mathbf{a}^-_t - \mathbf{a}_t = c_a \mathbf{a}^+_{t-1} - \mathbf{a}_t \tag{3A.15}$$

where the minus superscript of $\mathbf{a}^-_t$ and the plus superscript $\mathbf{a}^+_{t-1}$ mean a prior acceleration estimation in *t* and a posterior acceleration estimation in *t*-1, respectively; and

$\mathbf{a}_t$ is the actual acceleration of the ROV in t.

Using the first order low pass filter given by equation (3A.14), a prior estimate can be inserted into equation (7) as follows:

$$\mathbf{y}_{A,t} - c_a \mathbf{a}^+_{t-1} = g\mathbf{Z}_t - \mathbf{a}^-_{\varepsilon,t} + \mathbf{n}_A \tag{3A.16}$$

The terms in equation (3A.16) can be simplified and rewritten as,

$$\mathbf{z}_t = \mathbf{H} \cdot \mathbf{Z}_t + \mathbf{v}_t \tag{3A.17}$$

where $\mathbf{z}_t$ is the measurement vector with acceleration compensation $\mathbf{z}_t = \mathbf{y}_{A,t} - c_a \mathbf{a}^+_{t-1}$;

$\mathbf{H}$ is the observation matrix $\mathbf{H} = g\mathbf{I}$; and

$\mathbf{v}_t$ is the measurement noise of the model $\mathbf{v}_t = -\mathbf{a}^-_{\varepsilon,t} + \mathbf{n}_A$.

The covariance of the measurement noise $\mathbf{M}_t = E\left[v_t v_t^T\right]$ can be calculated by using the formula proposed by Jung et al. (2012) as,

$$\mathbf{M}_t = E\left[v_t v_t^T\right] = \Sigma_A + \frac{1}{3} c_a^2 \left\| \mathbf{a}^+_{t-1} \right\|^2 \mathbf{I} \quad . \tag{3A.18}$$

Through equation (3A.18), it is seen that the covariance of the measurement noise is proportional to the magnitude of the ROV's accelerations. In other words, the higher the acceleration of the ROV, the less reliable will be the measurement process obtained through equation (3A.7).The first Kalman filter process for attitude estimation is summarized in **Fig. 3A. 9** and the roll and pitch angle of the ROV are obtained based on formula (3A.8). A normalization step is applied after estimation step to ensure $\|\mathbf{Z}\|=1$.

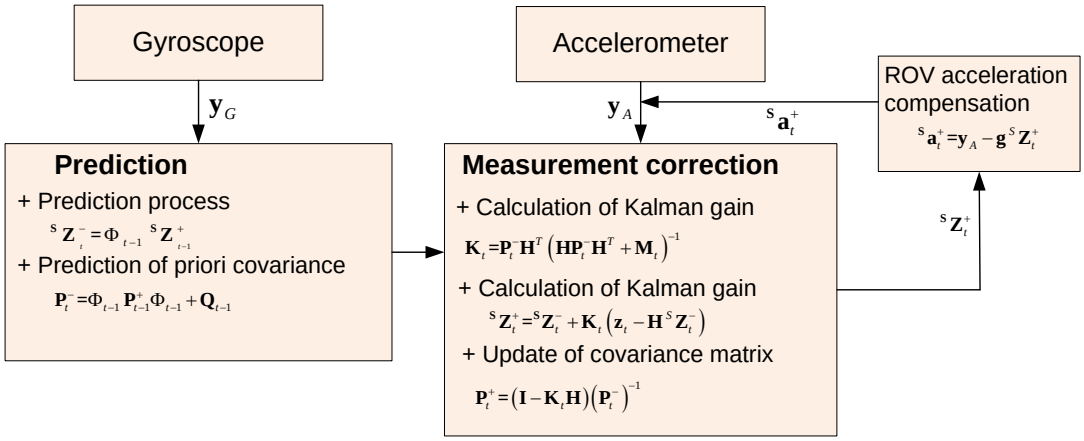

Fig. 3A.9 Attitude estimation by compensating ROV acceleration

3A.3.3 Kalman filter for heading estimation (second layer)

In this part the two sensors, i.e. the magnetometer and gyroscope, are fused using the Kalman filter to compensate for the bias of the gyroscope reading. The observation states include the heading angle and the gyro bias.

The model equation of heading angle estimation is presented as:

$$\dot{\mathbf{x}} = \mathbf{A}\mathbf{x} + \mathbf{z}_{gyro} + \mathbf{w} \tag{3A.19}$$

$$\mathbf{y} = \mathbf{C}\mathbf{x} + \mathbf{v} \tag{3A.20}$$

where

$\mathbf{x}$ is the state vector, which includes the yaw angle and the bias of the gyroscope $\mathbf{x} = [\psi \; B_{gyro}]^T$;

$\mathbf{z}_{gyro}$ contains the measurement from the gyroscope and the roll and pitch angle obtained from the first KF layer $\mathbf{z}_{gyro} = \begin{bmatrix} Z_{gyro} & 0 \end{bmatrix}^T = [q\frac{\sin(\phi)}{\cos(\theta)} + r\frac{\cos(\phi)}{\cos(\theta)} \quad 0]^T$;

$\mathbf{w}$ is the vector of the noise which is assumed to be a zero mean Gaussian white noise process with the covariance matrix $\mathbf{Q} = \begin{bmatrix} Q_{heading} & 0 \\ 0 & Q_{gyro} \end{bmatrix}$;

C is the observer matrix $\mathbf{C} = \begin{bmatrix} 1 & 0 \end{bmatrix}$;

$\mathbf{v}$ is the measurement vector of noise of the magnetometer whose covariance matrix $\mathbf{R}=R_{angle}$; and

$\mathbf{y}$ is the magnetometer data.

Thus, the derivative of the state vector is obtained as $\dot{\mathbf{x}} = [\dot{\psi} \ \dot{B}_{gyro}]^T$.

The relation between the yaw rate and the gyroscope measurement can be written as,

$$\dot{\psi} = q\frac{\sin(\phi)}{\cos(\theta)} + r\frac{\cos(\phi)}{\cos(\theta)} = q_{gyro}\frac{\sin(\phi)}{\cos(\theta)} + r_{gyro}\frac{\cos(\phi)}{\cos(\theta)} - B_{gyro}\left(\frac{\sin(\phi)}{\cos(\theta)} + \frac{\cos(\phi)}{\cos(\theta)}\right). \tag{3A.21}$$

where q_{gyro} and r_{gyro} are the pitch and yaw angular velocities obtained from the gyroscope, respectively.

Assuming that the bias of the gyroscope is slowly changing, then $\dot{B}_{gyro} \approx 0$.

From (3A.21), equation (3A.19) is derived as,

$$\begin{bmatrix} \dot{\psi} \\ \dot{B}_{gyro} \end{bmatrix} = \underbrace{\begin{bmatrix} 0 & -\left(\frac{\sin(\phi)}{\cos(\theta)} + \frac{\cos(\phi)}{\cos(\theta)}\right) \\ 0 & 0 \end{bmatrix}}_{\mathbf{A}} \cdot \begin{bmatrix} \psi \\ B_{gyro} \end{bmatrix} + \underbrace{\begin{bmatrix} q_{gyro}\frac{\sin(\phi)}{\cos(\theta)} + r_{gyro}\frac{\cos(\phi)}{\cos(\theta)} \\ 0 \end{bmatrix}}_{\mathbf{B}} + \mathbf{w} \tag{3A.22}$$

The continuous-time Kalman filter algorithm can be described by the following steps (Young-Soo, 2010).

Step 1: Define the initial vector and the error covariance matrix

Covariance matrix of error $\mathbf{P}(0) = E\left[\left(x(0) - \hat{x}(0)\right)\left(x(0) - \hat{x}(0)\right)^T\right]$

Initial state vector $\hat{\mathbf{x}}(0) = [\hat{\theta}(0) \ \hat{B}_{gyro}(0)]^T$

Step 2: Update the error covariance matrix update

$$\dot{\mathbf{P}}(t) = \mathbf{A}\cdot\mathbf{P}(t-1) + \mathbf{P}(t-1)\cdot\mathbf{A}^T + \mathbf{Q} - \mathbf{P}(t-1)\cdot\mathbf{C}^T\cdot\mathbf{R}^{-1}\cdot\mathbf{C}\cdot\mathbf{P}(t-1) \tag{3A.23}$$

$$\mathbf{P}(t) = \mathbf{P}(t-1) + \dot{\mathbf{P}}(t)\,dt \tag{3A.24}$$

Step 3: Calculate the Kalman gain

The Kalman gain is calculated as,

$$\mathbf{K}(t) = \mathbf{P}(t) \cdot \mathbf{C}^T \cdot \mathbf{R}^{-1} \tag{3A.25}$$

with $\mathbf{K}(t) = \begin{bmatrix} K_1(t) & K_2(t) \end{bmatrix}^T$.

Step 4: Estimate the vector of states

The new state vector is updated through the following formula,

$$\dot{\hat{\mathbf{x}}}(t) = \mathbf{A} \cdot \hat{\mathbf{x}}(t-1) + \mathbf{z}_{gyro}(t) + \mathbf{K}(t)\left[\mathbf{y}(t) - \mathbf{C} \cdot \hat{\mathbf{x}}(t-1)\right] \tag{3A.26}$$

$$\hat{\mathbf{x}}(t) = \hat{\mathbf{x}}(t-1) + \dot{\hat{\mathbf{x}}}(t)\,dt \tag{3A.27}$$

Step 5: Update the covariance of the measurement process R_{angle}

The covariance of the magnetometer is updated based on threshold-based switching strategy. The readings of the magnetometer are compared with the magnetic vector, which is known. The norm of the difference between these data is used as the switching condition for the covariance as follows:

$$R_{angle} = \begin{cases} \sigma_M^2 & \text{if } \left\| |\theta| + |\phi| \right\| \le |\varepsilon_M| \\ \infty & \text{otherwise} \end{cases} \tag{3A.28}$$

where ϕ and θ are the amplitude of roll and pitch oscillations respectively; and ε_M is the threshold of the switching scheme.

3A.4 Experimental results and discussion

3A.4.1 Experiment scenarios

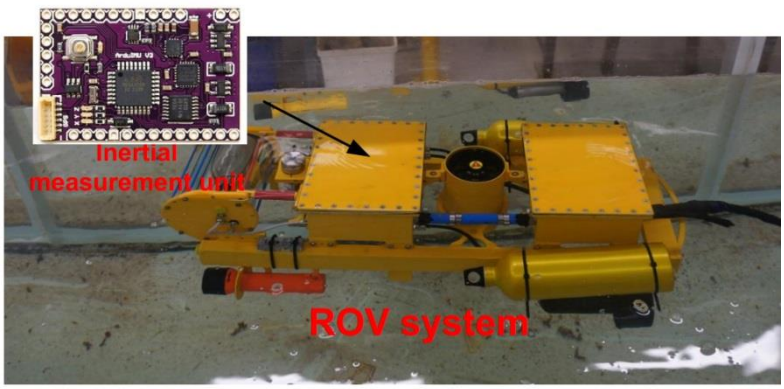

Fig. 3A.10 Experimental validation using AMC ROV-IV in AMC's Towing Tank

To verify the proposed algorithm, experiments were conducted using the AMC ROV-IV in the towing tank of the Australian Maritime College (**Fig. 3A.10**). Based on the feedback from the low-cost sensors, (see **Table 3A.1**), the heading observer algorithm was developed within a real-time environment at a 100Hz sampling rate. To check the accuracy of the heading estimation, the image processing technique was applied and synchronized with the running time of the ROV program. A camera was installed above the vehicle to capture the ROV's heading posture based on an image processing algorithm.

The operations of the ROV are governed by an Arduino Mega 2560 microcontroller board, connected to the peripheral sensors such as the inertial measurement unit (IMU), the digital magnetometer, and the pressure sensor. They all provide the states of the vehicle, including the acceleration, rotational rates, depth, and direction. All information from the sensors is gathered by an ATmega2560 microcontroller and forwarded to the control station via a RS-485 serial communication at a baud rate of 115200bps. Then, the main control algorithm, which is developed in the station computer, receives and processes the raw data.

Table 3A.2 Characteristics of operating conditions

Disturbance / Specification	Zero disturbance	Medium disturbance	Large disturbance
External acceleration	N/A	0.2-0.8m/s^2	1-2 m/s^2
Roll and pitch oscillation	N/A	5-10 degree	10-15 degree

During the experiments three different operating conditions, i.e. zero, medium, and large disturbances, are applied in turn to verify the effectiveness of the observer. The disturbances consist of horizontal external acceleration and roll/pitch oscillations roughly estimated by image processing to be in line with the specifications given in **Table 3A.2**. To establish the advantages of the proposed algorithm, the results by using a traditional Kalman filter (where the covariance is invariant) are compared against those of the proposed observers. The parameters of both algorithms as selected are shown in **Table 3A.3**. The effects of the magnetometer threshold on the estimation results were also studied by, in turn, applying difference threshold values to the proposed algorithms. The results of these cases are discussed in Section 3A.4.2.

Table 3A.3 Parameters of the observer algorithm

	Process name	Traditional Kalman filter(KF) observer	Proposed observer
First KF layer (Roll/pitch estimation)	Gyroscope measurement (Σ_G)	N/A	$\Sigma_G = \begin{bmatrix} 0.1 & 0 & 0 \\ 0 & 0.1 & 0 \\ 0 & 0 & 0.1 \end{bmatrix}$
	Acceleration measurement (Σ_A)	N/A	$\Sigma_A = \begin{bmatrix} 0.2 & 0 & 0 \\ 0 & 0.2 & 0 \\ 0 & 0 & 0.2 \end{bmatrix}$
	Coefficient of low pass filter (c_a)	N/A	0.1
Second KF layer (Heading estimation)	Process noise covariance	$\mathbf{Q} = \begin{bmatrix} \frac{0.02*180}{\pi} & 0 \\ 0 & \frac{0.04*180}{\pi} \end{bmatrix}$	$\mathbf{Q} = \begin{bmatrix} \frac{0.02*180}{\pi} & 0 \\ 0 & \frac{0.04*180}{\pi} \end{bmatrix}$
	Measurement noise covariance	R_{angle} R=0.2	$R_{angle} = \begin{cases} 0.2 & \text{if } \left\| \lvert\theta\rvert + \lvert\phi\rvert \right\| \le \varepsilon_M \\ \infty & \text{otherwise} \end{cases}$

3A.4.2 Comparison and discussion

In the first experiment, the focus was on the effectiveness of roll and pitch compensation for the yaw rate calculation. The compensator results, including roll and pitch angles, were combined with the yaw rate from the gyroscope to calculate the heading rate using equation (3A.6). The heading of the vehicle, which is an integral of equation (3A.6), is then compared to the true heading captured by the camera system, and the non-compensating measurement to clarify the effectiveness of the compensator.

The data due to zero and large disturbances are then processed by the first layer filter giving the results as shown in **Fig. 3A.11(a)**. In the zero-disturbance case, it is seen that there is almost no difference between the original measurement and the filter results as the roll and pitch angles are very small. The effects of the roll/pitch compensator are clearly shown in **Fig. 3A.11(b)** as the large disturbance motion is applied to the vehicle, where the drift of the compensated results, represented by the red line, is reduced in comparison to the original measurement.

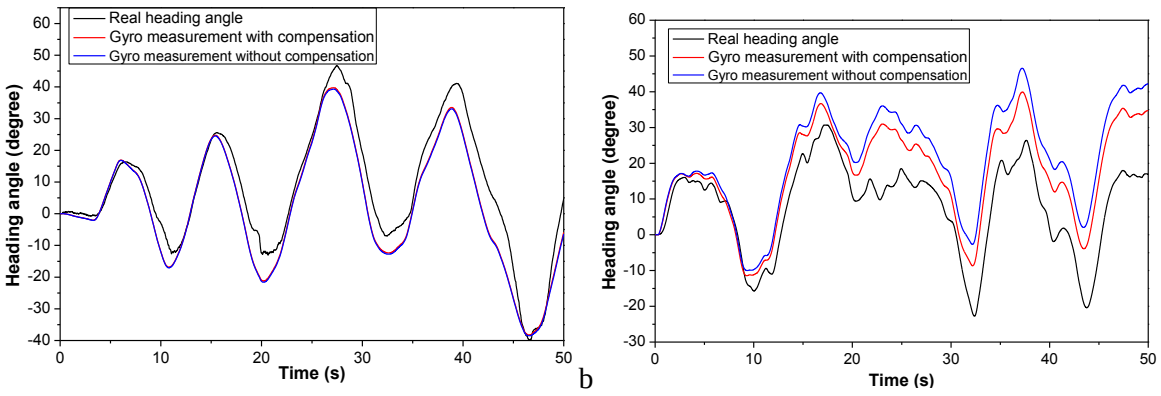

Fig. 3A.11 Heading angle determined by the gyroscope (a) Without disturbance. (b) With large disturbance

For each of the above operating conditions, the heading of the ROV estimated using a traditional KF and the proposed observer are shown in **Fig. 3A.12**. In this test, the threshold for the magnitude of the magnetometer was set at 15.

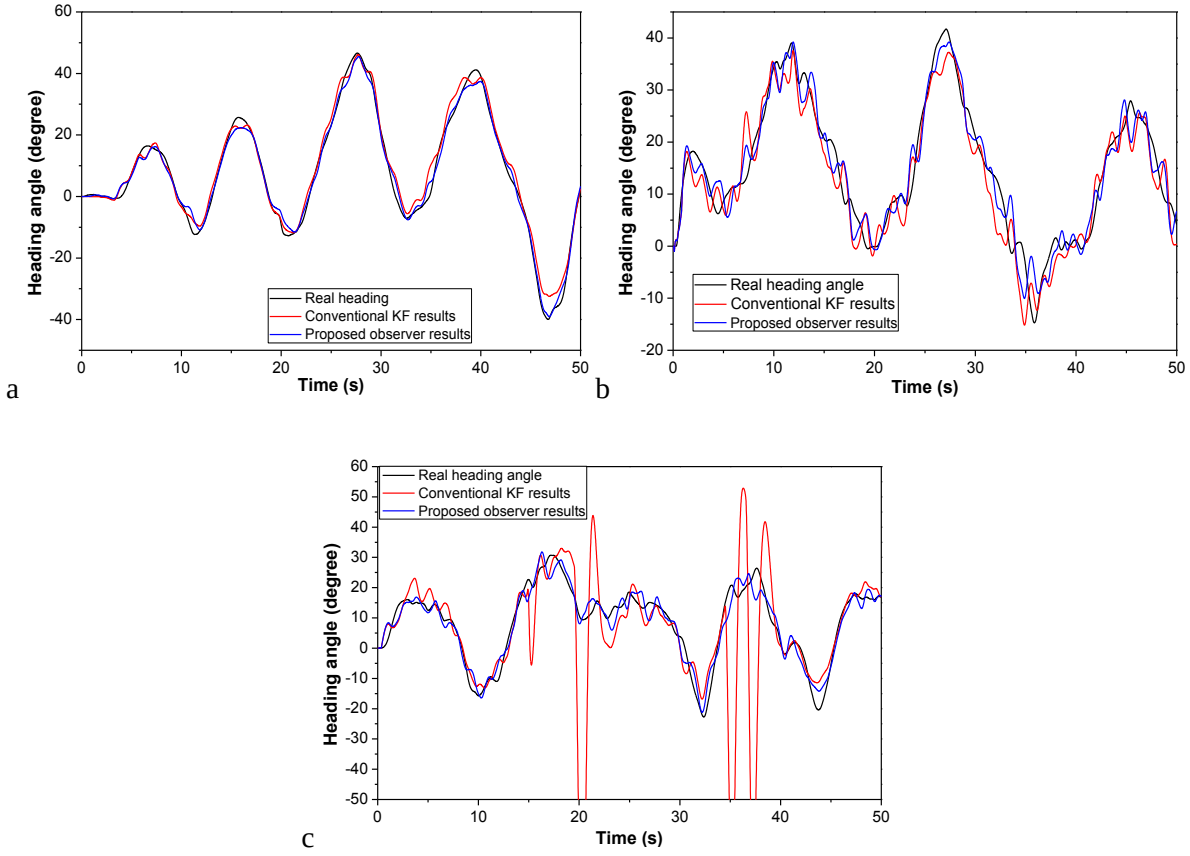

Fig. 3A.12 Heading observer results. (a) Zero-disturbance case (b) Medium disturbance case (c) Large disturbance case

It is seen that in the zero disturbance case (**Fig. 3A. 12**(**a**)), the performance between the conventional KF and the proposed observer is almost the same as there are no external accelerations and roll/pitch

oscillations requiring compensation. The difference between these algorithms is clearer in the case where the external disturbances are present. For the medium disturbances case (**Fig. 3A. 12(b)**), the results provided by both algorithms have minor oscillations around the actual heading captured by the camera, which is due to the magnetic noise. Although the covariance of the magnetometer measurement is varied to prevent the result from the sudden jerks, the amplitude of the noise does not further exceed the sensor threshold. For this reason, the proposed algorithm cannot completely eliminate the small amplitude disturbance from the estimation results. Nevertheless, the root mean square errors of the compared algorithms, shown in **Table 3A.4**, show that the proposed algorithm provides better results than the conventional algorithms.

Table 3A.4 Root mean square error of vehicle heading for different operating conditions

Disturbance / Algorithm	Zero disturbance	Medium disturbance	Large disturbance
Convention KF observer	2.86 degree	4.24 degree	21.45 degree
Proposed observer based on two-layer KF	1.95 degree	3.42 degrees	3.27 degree

However, in the large disturbance case (**Fig. 3A.12(c)**), the advantages of the proposed observer are clearly seen. It is seen that the sudden changes of the estimation results, caused by the large roll and pitch disturbances, are eliminated as the covariance of the magnetometer is set to infinity. Thus, the proposed observer achieves relatively smooth heading estimation results.

From the estimated bias results shown in **Fig. 3A.13**, it is seen that the bias varies by a wide range from -12 to 12 degree, which is much higher than those from the static-state experiment in Section 3A.2.2.1. This proves that the bias of the low-cost gyro sensor is highly unpredictable, as it depends not only on the ambient temperature but also on the characteristics of the ROV motions. **Fig. 3A.13** also describes the comparison between the KF and the proposed observer results, with the difference between these results clearly seen in the large-disturbance case. With the conventional KF observer the bias estimation is inaccurate and provides unreliable information for the gyroscope, as the correction data from the magnetometer contains the large amplitude disturbance. This phenomenon is much improved with the proposed algorithm.

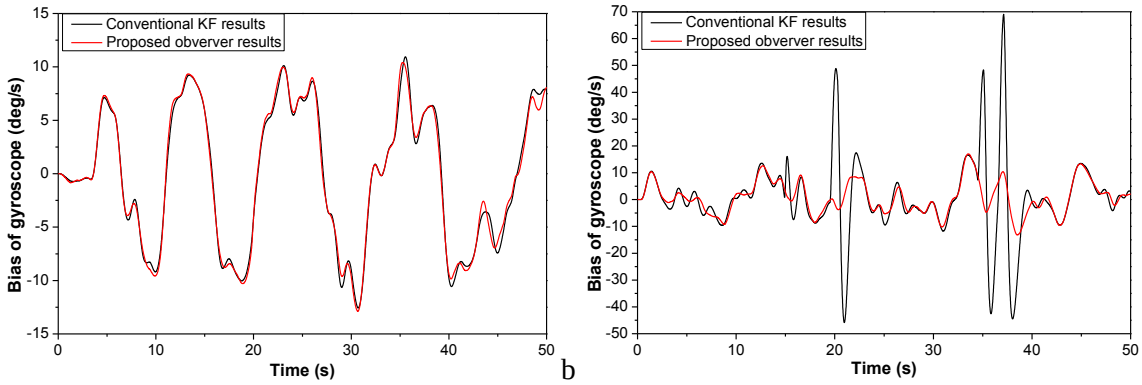

b

Fig. 3A.13 Bias estimation of conventional KF and proposed algorithm (a) Zero disturbance case (b) Large disturbance case

In order to verify the effectiveness of the two-layer KF in drift compensation, the longer test was conducted in medium disturbance case. **Fig. 3A. 14(a)** shows the actual heading of the ROV obtained by the external camera and the heading estimated by two-layer KF and the gyroscope measurement. The drift phenomenon of the gyroscope is clearly observed in **Fig. 3A.14(b)** as the heading error from the gyro measurement, represented by the red line, gradually increases from 0 to around 10 degree after 200 seconds. While the average error of the two-layer KF results is constant with time, the error oscillates around 0 with the amplitude $\pm$ 4.5 degree. This indicates that the two-layer KF observer can effectively compensate the drift of the gyroscope measurement.

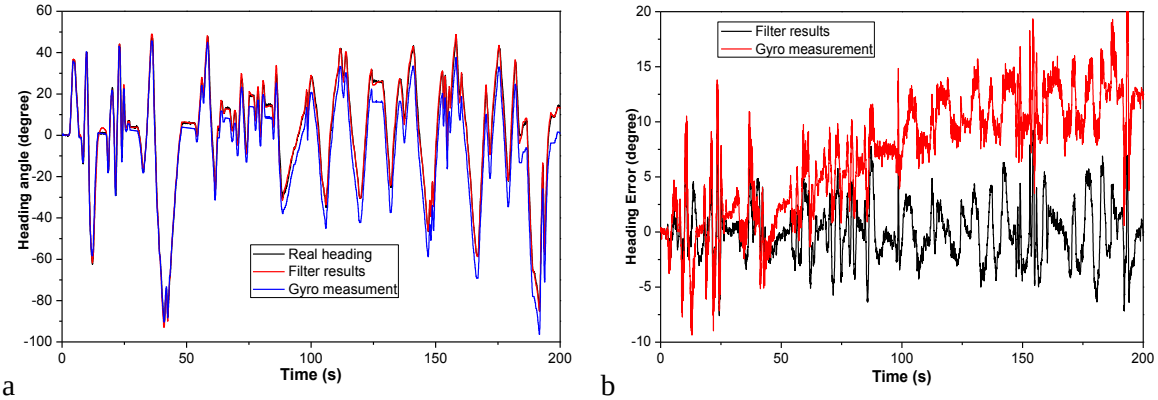

a b

Fig. 3A.14 Heading observer results in 200sec. (a) Filter results and gyroscope measurement (b) Heading error

It is known that the threshold for the magnetometer covariance selection plays an important role in the quality of the estimation results. Low threshold settings mean that the compass measurement is less sensitive to the roll/pitch oscillations. In other words, a small oscillation is enough to block the contribution of the magnetometer to the estimation process. However, it does not indicate that when a small threshold value is set a better estimation result is obtained. The reason is that the drift of the

gyroscope cannot be compensated for when the correction source is not available due to the infinitive covariance value.

Table 3A.5 Root mean square error of vehicle heading from different threshold values

Threshold value	Root mean square error
ε_M =30	5.07 degrees
ε_M =20	4.25 degrees
ε_M =15	3.27 degrees
ε_M =5	4.83 degrees

Fig. 3A.15 and **Table 3A.5** show the performance of the proposed observer using different threshold values. It is seen that the error decreases as the threshold is adjusted down from 30 to 15, but starts to increase as the parameter is decreased further. The proper threshold should balance the contribution of the gyroscope and magnetometer with the estimation results. The threshold value depends, not only the inclination of the magnetic field, but also the quality of the gyroscope, especially the bias characteristic. In this working condition, the experimental results show that the value of 15 is the most appropriate threshold for the heading observer. However, this value has to be re-determined when deploying the ROV in different areas as the magnetic inclinations can change.

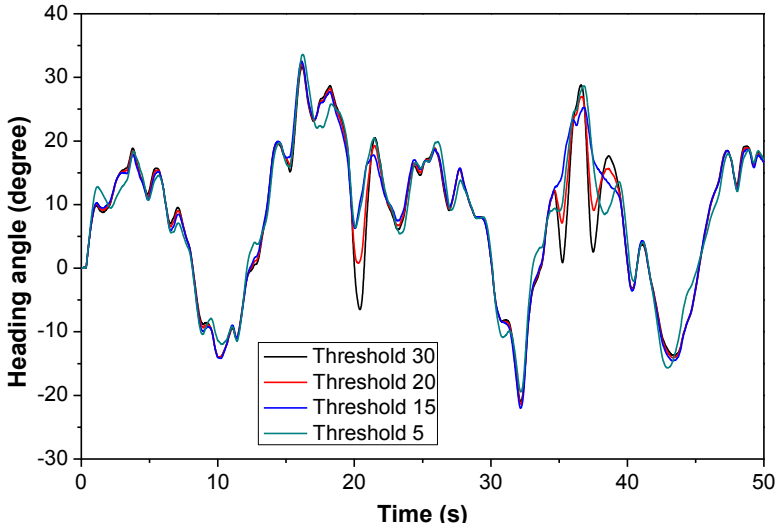

Fig. 3A.15 Heading estimation results using different threshold values

3A.5 Conclusions

This paper presented the development of a heading observer for ROVs based on a low-cost sensor system, including an inertial measurement unit and magnetometer. The proposed observer, which consists of a two-layer Kalman filter, is aimed at eliminating the effect of roll/pitch oscillations and acceleration disturbances, which are widely present when operating in proximity to the free surface. The first layer was applied to accurately estimate the roll and pitch angles by combining the data from the gyroscope and accelerometer. The results were then used to calculate the heading rate and the covariance value of the magnetometer in the second layer. By applying the variant covariance scheme, the 'jerk' phenomenon of the digital compass reading, caused by the roll/pitch oscillations, is eliminated. The effectiveness of the proposed observer was verified by conducting experiments using a test ROV, with the results of the observer compared against the true headings captured by an external camera. The comparisons show that the estimation results are much better than those of using the traditional Kalman filter as the error of the heading estimation was reduced by applying the two-layer KF algorithm, especially with the presence of roll and pitch disturbances. Thus, the proposed algorithm is a suitable solution to estimate the heading for low-cost sensor-based ROVs. By providing high quality feedback data, the proposed observer improves the performance of the ROV heading controller.

Further work is required to determine the value of the magnetometer threshold. Currently, this value is determined by a trial and error process, which is time consuming. Thus, a self-adaptive threshold is currently being developed to quickly deploy the algorithm in various working conditions.

Chapter 3-Part B: A Self-tuning Nonlinear PID Controller for a Three-Thruster Remotely Operated Underwater Vehicle

This subchapter has been published in the Proceedings of the Second Vietnam Conference on Control and Automation

Le, KD and Nguyen, HD and Ranmuthugala, SD, *A Self-tuning Nonlinear PID Controller for a Three-Thruster Remotely Operated Underwater Vehicle*, Proceedings of the Second Vietnam Conference on Control and Automation, 22 - 23 November 2013, Da Nang, Vietnam, pp. 1-8. (2013)

Chapter 4: ROV Haptic Joystick and Artificial Potential Field (APF) for Obstacle Detection

Chapter 4 presents the development of a haptic joystick and a novel Artificial Potential Field (APF) technique for a haptic controller of an underwater Remotely Operated Vehicle (ROV) to assist the pilot to avoid obstacles. In the first part, a lab-developed haptic joystick was fabricated and tested in the simulation of control the surge motion of the AMC-ROV-IV where the drag force from fluid was fed back to ROV pilots over haptic force. In the next part, the APF algorithm was designed to replicate potential risks presented by underwater obstacles in the vicinity of the ROV, enabling the haptic drive system to alert ROV pilots to potential dangers due to surrounding obstacles and prompt pilots through the haptic joystick described in part A to avoid the dangers and safely navigate the vehicle.

Chapter4 - Part A: Haptic Driving System for Surge Motion Control of Remotely Operated Underwater Vehicles

This subchapter has been published in International Conference on Modelling, Identification and Control. The citation of the research paper is:

Le, KD and Nguyen, HD and Ranmuthugala, D and Forrest, AL, *Haptic driving system for surge motion control of underwater remotely operated vehicles*, The 6th International conference on modelling, identification and control, 3-5 December, Melbourne, Australia, pp. 31. (2014)

Chapter 4 - Part B: Artificial Potential Field for ROV Haptic Control in Dynamic Environment

This subchapter has been submitted for publication in the Journal of Systems and Control Engineering and at the time of writing is accepted and waiting for being published. The citation of the research article is:

Le, KD and Nguyen, HD and Ranmuthugala, D and Forrest, AL, Artificial Potential Field for ROV haptic control in dynamic environment, Proceedings of the Institution of Mechanical Engineers, Part I: Journal of Systems and Control Engineering [Accepted 2016]

Abstract

This paper presents the development of a novel Artificial Potential Field (APF) technique for a haptic controller of an underwater Remotely Operated Vehicle (ROV) to assist the pilot to avoid obstacles. The APF technique is used to replicate potential risks presented by underwater obstacles in the vicinity of the ROV. Based on the APF technique, a risk avoidance vector is calculated and transmitted to a haptic joystick to generate the tactile feedback, which enables the ROV pilot to be alerted to potential dangers due to surrounding obstacles and prompt the pilot through the joystick to avoid the dangers and safely navigation the vehicle. The novel APF technique can deal with both stationary and moving obstacles as it is combined with an obstacle motion detection algorithm based on Fuzzy C-Means (FCM) and Kalman Filter (KF) algorithms. These algorithms are applied to process raw data from the scanning sensor to identify the relative positions and velocities between the ROV and the obstacles, which are employed within the APF calculations. To validate the proposed technique, the haptic joystick and the novel APF formula were applied to control a simulated ROV within a virtual reality (VR) environment.

Keywords: Artificial Potential Field, Remotely Operated Vehicles, dynamic obstacle, virtual reality.

4B.1 Introduction

Contrary to submarine control strategies, ROV pilots remain remote to the vehicle and control it using tele-operation technology. Pilots indirectly perceive operating environments based on the feedback from sensors such as depth, velocity, and inertial sensors located on ROVs and visuals feedback via on-board cameras. However, due to the lack of 3-D information and limitations with quality and field vision of the cameras, ROV pilots are not always able to observe and identify external hazards purely on visual feedback, especially when ROVs operate in environments littered with obstacles, which can result in collisions. Lam (2009) states it is difficult to ensure the safety of ROVs using tele-operation control systems by purely relying on visual feedback. A potential solution is to add one or more feedback senses to assist pilots to safely manoeuvre the ROV through the surrounding hazards.

One option with regard to tele-operation control is to include a tactile user interface that would enhance operator awareness of the working environment and improve performance, especially in collision avoidance (Lam, 2009).The virtues of a tactile user interface are that it allows pilots to feel as if they are directly interacting with the working environment. This technique is commonly known as haptic control and it has been widely applied in tele-operation control systems for mobile robots and robotic manipulators. Rösch et al. (2002) proposed a haptic interface for mobile robot controllers,

which consisted of a force feedback joystick and ultrasonic sensors to create a force feedback loop.[2] As the robot moves closer to an obstacle, the joystick actuators generate a force inversely proportional to the distance to the obstacle in order to warn the operator of the proximity and prevent collision. Along the same lines Ryu et al. (2010) fabricated a 6-DOF haptic master joystick for tele-operation of a mobile manipulator robot. Others have developed haptic collision avoidance systems for aerial vehicles (Brandt & Colton, 2010; Lam, 2009; Lee, Sukhatme, Kim, & Park, 2005). For underwater vehicles, Zhenying (2012) proposed the use of haptic feedback to control a biomimetic fish robot. The work combined kinematic modelling and Computational Fluid Dynamics (CFD) analysis to provide force feedback for the users enabling them to 'feel' the forces acting on the robot body as well as the field distribution maps such as velocity and pressure.

Haptic technology can be applied to ROV driving systems to improve the performance of ROV pilots. In addition to seeing the obstacles via on-board cameras, the haptic driving system will provide ROV pilots with the ability to 'feel' the obstacles based on its proximity and potential danger, enabling them to take the necessary action to prevent collision. However, most of the previous research in haptic control systems assumed that the environment around the vehicle remained unchanged with fixed location obstacles (Jensen, Tolbert, Wagner, Switzer, & Finn, 2011; Lee et al., 2005). In the study of Lee et. al. (2005), the application of haptic tele-operation technique in controlling a mobile robot was focused on. The feedback forces included the environment force and the collision-preventing force which are merely calculated from the distance information between the robot and the obstacles and the possible-turning angles enabling the robot to change direction without colliding to obstacle. Only static obstacles, such as straight rectangular wall, cylindrical wall and curved wall, were considered in their experiments. Jensen et. al. (2011) proposed to apply the haptic feedback control strategy to the automotive steering system to improve the safety of drivers. The study has been verified using a driving simulation software and shown the optimistic results that the haptic steering feedback improved driver performance by reducing 62% of obstacle hit rate. However, the testing scenarios are rather simple, only consisting of nine sets of three black cones used as fixed obstacles, compared to the complexity of actual traffic conditions which involve various dynamic obstacles, i.e. other automobiles and pedestrians, hence casting doubt on the efficacy of the proposed haptic steering system.

In the underwater environment, the actual operating environments of ROVs are much more complex than those of terrain vehicles because they are littered with many uncertain factors, such as static and moving (or dynamic) obstacles. The motion of dynamic obstacles is hard to determine; and for this reason it causes a substantial threat to ROV safety. In the work presented in this paper, the ROV haptic driving system is improved to deal with dynamic working environments, including both static and moving obstacles. A scanning sensor is used to detect obstacles around the ROV by making a 2D full-circle scan. Based on the raw data, an advanced algorithm, consisting of Fuzzy C-Means (FCM)

and Kalman Filter (KF) algorithms, is used to determine relative positions and velocities between the obstacles and the ROV. Based on this information, an Artificial Potential Field (APF) is utilised to model the risks presented by the obstacles to generate a risk avoidance vector, which is then used to generate the torque reference signals for the haptic controller. The control signals drive the actuators incorporated within the joystick providing the ROV with force feedback based on the obstacle information.

To verify the proposed technique, the haptic joystick and the novel Artificial Potential Field (APF) algorithm were utilised within a virtual reality (VR) environments to control a simulated ROV. The simulation results indicate that the combined FCM and KF algorithms provide good estimations of obstacle states, with the tactile feedback accurately describes the risks arising from those obstacles.

4B.2 Overview of ROV Haptic Driving system

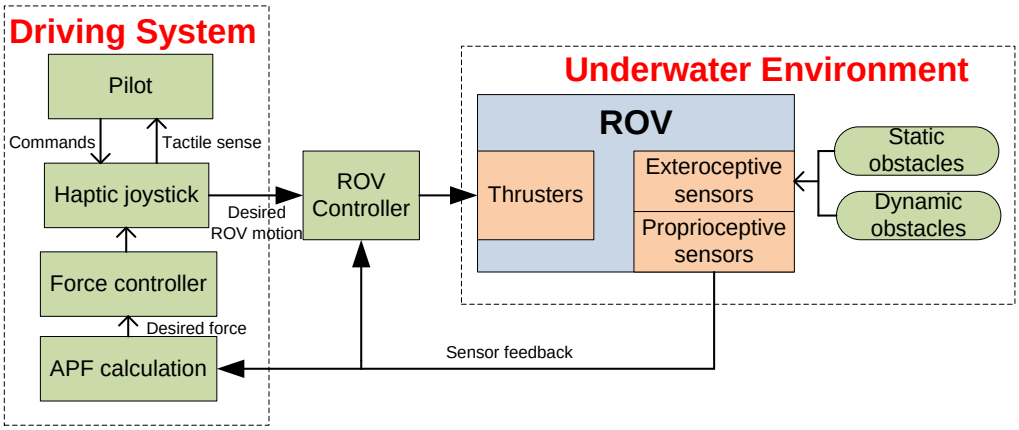

Fig. 4B.1. Overview of ROV haptic driving system

An overview of the ROV haptic driving system is presented in **Fig. 4B.1**, which consists of two main parts: the ROV which provides tactile feedback to the haptic joystick handler and the haptic driving system which converts commands from the pilot to the ROV controller. The former function is widely performed in conventional ROV driving systems; thus the focus of the research is on the application of the latter function in collision avoidance tasks.

The states of the ROV, (i.e. position, heading, and velocity), and information on the surrounding obstacles are obtained by proprioceptive and exteroceptive sensors, which include the inertial and scanning sensors and the ROV positioning system. A combined FCM and KF algorithm processes the raw data from the sensors to determine the relative positions and velocities between ROV and the obstacles. The results are then forwarded to APF algorithm to calculate the final risk avoidance vectors, which are used as reference signals for the force controller incorporated within the haptic joystick system.

4B.3 Artificial Potential Field (APF) within a Dynamic Environment

4B.3.1 APF calculation

The application of APF proposed by Khatib (1985) is defined as the field which is generated by obstacles and navigation targets. This technique was first applied to local path planning in autonomous ground vehicles applications. The basic principle of APF is that obstacles generate repulsive force while targets create attraction force to vehicles. This would results in the vehicles naturally approaching targets while avoiding obstacles, a strategy that has successfully been applied to controlling aerial vehicles, satellite trajectory, and tele-operation systems(Cetin, Zagli, & Yilmaz, 2013; Koren & Borenstein, 1991; Nair, Behera, Kumar, & Jamshidi, 2014; Saravanakumar & Asokan, 2013).

In the APF algorithm developed by Khatib (1985), the intensity of the field depends on the relative positions between the robot and the obstacles. Thus, it will generate a repulsive force even when the relative velocities are zero, thus overestimating the threat and increasing the workload of the operators. To address this issue, research included the velocities and the deceleration limits into the potential field formula (Ge & Cui, 2002; Poty, Melchior, & Oustaloup, 2004). However, very little has been done in considering the APF algorithm within dynamic environments. At the same relative distance, a moving obstacle that is approaching the ROV presents a greater chance of collision than a static obstacle. For instance, **Fig. 4B.2** shows the scenarios of a ROV and an obstacle, moving at the velocity v_{veh} and v_{Obs} respectively, where the collision hazard increases as the velocity vectors converge.

This project enhances the Lam's Parametric Risk Field (PRF) formula by involving the velocities of the obstacles into this formula to ascertain the hazard presented by moving obstacles (Lam, 2009). The intensity of the artificial field depends not only on the relative distances but also on the relative velocities between the ROV and the obstacles. The ROV in this work is assumed to operate within a 2D XY plane, as shown in **Fig. 4B.2**, enabling the collision avoidance task to focus on a horizontal plane.

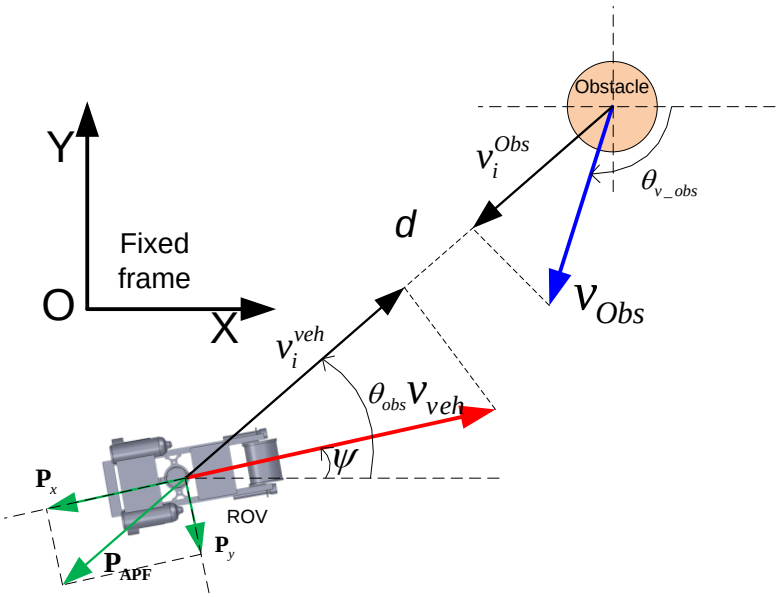

Fig. 4B.2 APF vector caused by dynamic obstacle within a fixed (XY) frame

The ROV positioning system, incorporating an acoustic sensor and a Doppler Velocity Log (DVL), is utilised to measure the absolute position and velocity of the ROV in the fixed (XY) frame, while a scanning sensor determines the relative positions between the ROV and the surrounding obstacles. The combined FCM-KF algorithm processes the data from these sensors to estimate the relative velocities. Finally, the APF algorithm uses the estimated relative positions and velocities to compute the risk avoidance vector, which represents the direction and level of the surrounding hazards. The calculation process is presented in **Fig. 4B.3**.

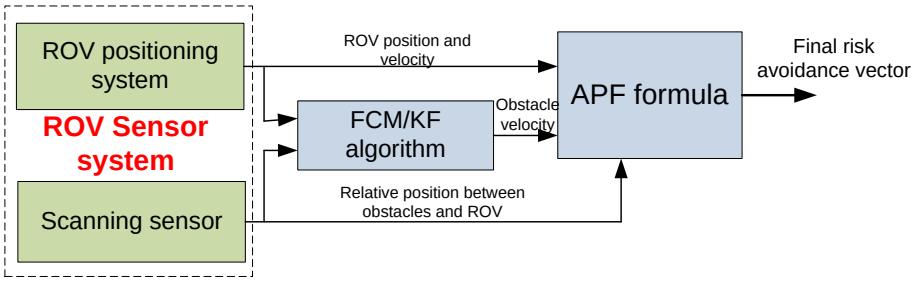

Fig. 4B.3 APF calculation algorithm

The amplitude of the vector $\mathbf{P}_{\mathbf{APF}}\left(d_i, v_i\right)$, ranging from 0 to 1, of the risk avoidance vector due to an obstacle is be calculated as (Lam, 2009),

$$\left|\mathbf{P}_{\mathbf{APF}}\left(d_i, v_i\right)\right| = \begin{cases} 1 & \text{when} \quad d_{res}\left(d_i, v_i\right) \le 0 \ or \ \dfrac{1+v_i}{d_{res}\left(d_i, v_i\right)} \ge \dfrac{1}{G} \\ 0 & \text{when} \quad \dfrac{1+v_i}{d_{res}\left(d_i, v_i\right)} \le 0 \\ G\left(\dfrac{1+v_i}{d_{res}\left(d_i, v_i\right)}\right) & \text{otherwise} \end{cases} \tag{4B.1}$$

where d_i is the relative distance between vehicle and obstacle, v_i is the relative velocity between them, d_{res} is the reserve avoidance distance, and G is a positive gain used to scale the function and adjust the field sensitivity.

From the formula (4B.1), it is seen that the amplitude of $\mathbf{P}_{\mathbf{APF}}\left(d_i, v_i\right)$ reaches the maximum value if the reserve avoidance distance is negative ($d_{res}\left(d_i, v_i\right) \le 0$) or the ROV is approaching the obstacle and potentially collides to it ($\dfrac{1+v_i}{d_{res}\left(d_i, v_i\right)} \ge \dfrac{1}{G}$).

Higher the gain G, larger the haptic force generated when the ROV approaches obstacles. The effect of G on the APF intensity is seen in **Fig. 4B.4**, where the danger area at G = 5 is much larger than that at G = 3. In other words, at the same relative velocity and position, the haptic force is proportional to the value of G. However, the high value of G is not always suitable to haptic controllers as it increases the repulsive force and hence the workload of the pilots, especially in cases where the pilots manoeuvre the ROV in close proximity to obstacles for inspection tasks.

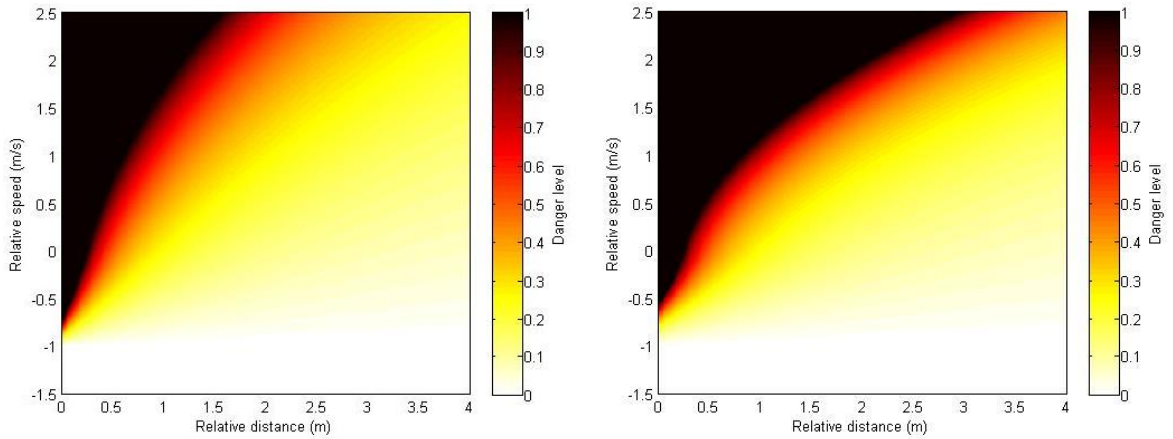

a. $a_{\max} = 1.5 m/s^2$, $G = 3$ b. $a_{\max} = 1.5 m/s^2$, $G = 5$

Fig. 4B.4. The AMP intensity for different gains Gat a maximum acceleration $a_{\max}$ of 1.5 m/s^2

The reserve avoidance distance is now computed as,

$$d_{res}\left(d,v_i\right)=\begin{cases} d+d_{stop}\left(v_i\right) & v_i\le 0 \\ d-d_{stop}\left(v_i\right) & v_i>0 \end{cases} \tag{4B.2}$$

where d_{stop} is the minimum required braking distance. The value of d_{stop} depends on both the relative velocity and the maximum acceleration $a_{\max}$ of the vehicle and is given by,

$$d_{stop}\left(v_i\right)=\frac{\left|v_i\right|^2}{2a_{\max}} \tag{4B.3}$$

The relative velocity between the vehicle and obstacle is obtained by (see **Fig. 4B.2**),

$$v_i=v_{veh}\cos\left(\theta_{obs}-\psi\right)-v_{Obs}\cos\left(\theta_{obs}-\theta_{v\_obs}\right) \tag{4B.4}$$

where v_{veh} and v_{Obs} are the velocity of the ROV and obstacle respectively, θ and θ_{v_obs} are the motion direction of the ROV and obstacle respectively, and θ_{obs} is the angle from the X axis to the straight line between the ROV and the obstacle.

The risk avoidance vector $\mathbf{P_{APF}}\left(d,v_i\right)$ is divided into two parts, i.e. $\mathbf{P_u}$ and $\mathbf{P_r}$, that are used to calculate the reference signals for the haptic torque controller in surge and yaw motion as,

$$\begin{aligned} \left|\mathbf{P}_u\right| &= \left|\mathbf{P}_{APF}\right|\cdot\cos\left(\theta_{obs}-\psi\right) \\ \left|\mathbf{P}_r\right| &= \left|\mathbf{P}_{APF}\right|\cdot\sin\left(\theta_{obs}-\psi\right) \end{aligned}. \tag{4B.5}$$

If multiple obstacles are present in the detected range of the sensors, the ‘max-min’ strategy is used to obtain the final risk avoidance vector. The principle of this strategy is that the final risk avoidance vector would be the vector caused by the riskiest obstacle. Lam (2009) showed that the max-min strategy is the best way to deal with multi-obstacles as it prevents the haptic driving system from over or underestimating risk sources.

4B.3.2 Obstacle velocity estimation

The velocities of the ROV and obstacle are required in order to calculate the final risk avoidance vector based on the APF formula given in (4B.1). Although the ROV velocity is obtained by the on board DVL system, there is no sensor that directly measures the velocity of the obstacle. Hence, an estimation algorithm, combining the FCM and KF algorithm, is required to acquire the latter.

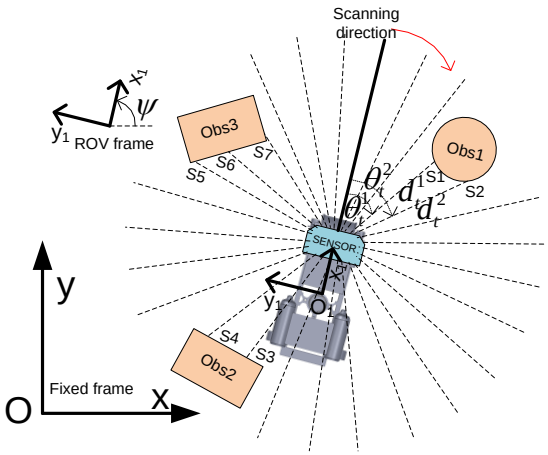

Fig. 4B.5 2D scanning sensor to detect obstacles

A 2D underwater range finder sensor using the time of flight principle provides a high resolution full circle scan in the XY plane to measure the relative distance between the ROV and obstacles (see **Fig. 4B.5**). The specifications of the sensor employed on the ROV control system are given in **Table 4B.1**.

Table 4B.1. Specifications of 2-D scanning sensor

Scan range	From 0.1m to 3.5m
Resolution	0.02deg.
Accuracy	1mm
Updating rate	10Hz

Fig. 4B.6 presents the linkage within the coupled FCM and KF algorithm. First, the FCM algorithm determines the positions of individual obstacles based on the data feedback from the scanning sensor. The results are then combined with the obstacle motion models by applying the KF algorithm to estimate the velocities of each obstacle.

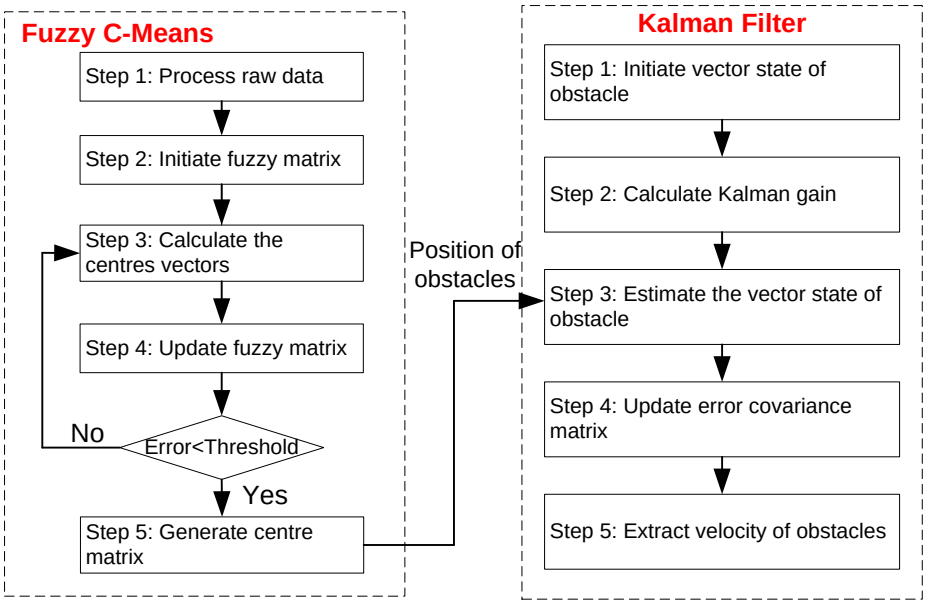

Fig. 4B.6 Coupled FCM-KF based estimation algorithm

- *Identifying obstacle position using Fuzzy C-Means algorithm*

The raw data from the scanning sensor are processed by FCM algorithm to determine the centres of the surrounding obstacles. Defining the obstacle position matrix as,

$$\mathbf{Obs}_t = \begin{bmatrix} O_{tx}^1 & O_{ty}^1 \\ O_{tx}^2 & O_{ty}^2 \\ \vdots & \vdots \\ O_{tx}^c & O_{ty}^c \end{bmatrix} \tag{4B.6}$$

where c is the number of detected obstacles at t; and $\begin{bmatrix} O_{tx}^i & O_{ty}^i \end{bmatrix}$ is the position of the i^{th} obstacle in the fixed (XY) frame at time t. The data from scanning sensor can be expressed as,

$$\mathbf{Sn}_t = \begin{bmatrix} \theta_t^1 & d_t^1 \\ \theta_t^2 & d_t^2 \\ \vdots & \vdots \\ \theta_t^N & d_t^N \end{bmatrix} \tag{4B.7}$$

where $\begin{bmatrix} \theta_t^i & d_t^i \end{bmatrix}$ is the polar coordinate of the i^{th} reading in the vehicle (x_1y_1) frame (see **Fig. 4B.5**) at time t; and N is the number of scanning rays reflected from obstacles.

Not all emitted beams from the scanning sensor are reflected by obstacles. Only the beams returned by obstacles are included in matrix $\mathbf{Sn}_t$. Thus N varies depending on the given situations. For example, if N is zero, there are no obstacles present in the scanning range of the sensor.

Once the matrix $\mathbf{Sn}_t$ is established, the following steps are carried out to determine the positions of the obstacles.

<u>Step 1</u>: Convert sensor data $\mathbf{Sn}_t$ from the vehicle (x_1y_1) frame to the fixed (XY) frame

Assume a point A having coordinates in the vehicle (x_1y_1) frame is A*(x,y)*. The general formula to convert A*(x,y)*to the fixed (XY) frame Oxy is then(Siegwart, Nourbakhsh, & Scaramuzza, 2011),

$$\begin{bmatrix} X_{fix} \\ Y_{fix} \end{bmatrix} = \begin{bmatrix} \cos\psi & -\sin\psi \\ \sin\psi & \cos\psi \end{bmatrix} \begin{bmatrix} x \\ y \end{bmatrix} + \begin{bmatrix} P_x \\ P_y \end{bmatrix} \tag{4B.8}$$

where $\begin{bmatrix} x & y \end{bmatrix}^T$ is the coordinates of A within the vehicle (x_1y_1) frame, $\begin{bmatrix} X_{fix} & Y_{fix} \end{bmatrix}^T$ is the coordinate of A within fixed (XY) frame, $\begin{bmatrix} P_x & P_y \end{bmatrix}^T$ is the vehicle position within the fixed frame, and ψ is the heading of the vehicle.

Using equation (4B.8), the matrix $\mathbf{Sn}_t$ containing the sensor data in the vehicle frame is converted to the fixed frame as,

$$\mathbf{Abs\_Sn}_t = \begin{bmatrix} A\_Obs_t^1 \\ A\_Obs_t^2 \\ \vdots \\ A\_Obs_t^N \end{bmatrix}$$

$$= \begin{bmatrix} d_t^1 \cdot \cos\theta_t^1 \cdot \cos\psi + d_t^1 \cdot \sin\theta_t^1 \cdot \sin\psi + P_x & -d_t^1 \cdot \cos\theta_t^1 \cdot \sin\psi + d_t^1 \cdot \sin\theta_t^1 \cdot \cos\psi + P_y \\ d_t^2 \cdot \cos\theta_t^2 \cdot \cos\psi + d_t^2 \cdot \sin\theta_t^2 \cdot \sin\psi + P_x & -d_t^2 \cdot \cos\theta_t^2 \cdot \sin\psi + d_t^2 \cdot \sin\theta_t^2 \cdot \cos\psi + P_y \\ \vdots & \vdots \\ d_t^N \cdot \cos\theta_t^N \cdot \cos\psi + d_t^N \cdot \sin\theta_t^N \cdot \sin\psi + P_x & -d_t^N \cdot \cos\theta_t^N \cdot \sin\psi + d_t^N \cdot \sin\theta_t^N \cdot \cos\psi + P_y \end{bmatrix} \tag{4B.9}$$

$$= \begin{bmatrix} d_t^1 \cos\left(\theta_t^1 - \psi\right) + P_x & d_t^1 \sin\left(\theta_t^1 - \psi\right) + P_y \\ d_t^2 \cos\left(\theta_t^2 - \psi\right) + P_x & d_t^2 \sin\left(\theta_t^2 - \psi\right) + P_y \\ \vdots & \vdots \\ d_t^N \cos\left(\theta_t^N - \psi\right) + P_x & d_t^N \sin\left(\theta_t^N - \psi\right) + P_y \end{bmatrix}$$

where $A\_Obs_t^i \in R^{2x1}$ is the scanned coordinate of the i^{th} obstacle transformed into the fixed frame at time t. The matrix $\mathbf{Abs\_Sn}_t$ is then used as the input to the FCM algorithm to determine the absolute obstacle coordinate.

<u>Step 2:</u> Initiate a random fuzzy matrix

The fuzzy matrix **U** at time t is defined as,

$$\mathbf{U}_t = \begin{bmatrix} \mu_{11} & \mu_{12} & \cdots & \mu_{1N} \\ \mu_{21} & \mu_{22} & \cdots & \mu_{2N} \\ \vdots & \vdots & \ddots & \vdots \\ \mu_{c1} & \mu_{c2} & \cdots & \mu_{cN} \end{bmatrix} \tag{4B.10}$$

where c and N are the number of obstacles and the number of scanning sensor data respectively at each time interval . Initially, the member of the **U** matrix can be randomly generated based on a Gaussian distribution. However, the following constraints must be met,

$$\begin{cases} \mu_{ik} \in [0,1] \text{ with} 1 \le i \le c, 1 \le k \le N \\ \sum_{i=1}^{c} \mu_{ik} = 1, \forall k \in \{1, 2, ..., N\} \\ 0 < \sum_{k=1}^{N} \mu_{ik} < N, \forall i \in \{1, 2, ..., c\} \end{cases} \tag{4B.11}$$

<u>Step 3</u>: Calculate the centre matrix

The coordinates of the obstacles, including the centres of the scanning data cluster, are presented in matrix V_t,

$$\mathbf{V}_t = \begin{bmatrix} v_t^1 \\ v_t^2 \\ \vdots \\ v_t^c \end{bmatrix} \tag{4B.12}$$

where v_t^i is the coordinates of the i^{th} obstacle in the fixed frame and calculated as,

$$v_t^i = \frac{\sum_{k=1}^{N} (\mu_{ik})^m A\_Obs_t^k}{\sum_{k=1}^{N} (\mu_{ik})^m}, 1 \le i \le c \tag{4B.13}$$

where m is the power factor satisfying $m \in (1, \infty)$.

<u>Step 4:</u> Update fuzzy matrix

The elements of the fuzzy matrix **U** are updated based on the distance between the input data and the centres of the clusters obtained in Step 3 as,

$$\mu_{ik} = \frac{1}{\sum_{j=1}^{c}\left(\frac{D\left(A\_Obs_t^k, v_t^i\right)}{D\left(A\_Obs_t^k, v_t^j\right)}\right)^{\frac{2}{m-1}}}, 1 \le i \le c \text{ and } 1 \le k \le N \tag{4B.14}$$

where $D\left(A\_Obs_t^k, v_t^i\right)$ is the distance between the k^{th} scanning data and the i^{th} obstacle centre. The distance D is calculated by,

$$D\left(A\_Obs_t^k, v_t^i\right) = \sqrt{\left(A\_Obs_t^k - v_t^i\right)^T \left(A\_Obs_t^k - v_t^i\right)} \tag{4B.15}$$

<u>Step 5</u>: Calculate the iteration error and generate centre matrix

The iteration error is defined as the norm of the difference between the fuzzy matrix **U** at times t+1 and t, and obtained by,

$$\varepsilon = \left\| \mathbf{U}_{t+1} - \mathbf{U}_t \right\| \tag{4B.16}$$

If the iteration error is smaller than the pre-defined stopping threshold the iteration loop is halted and the current centre matrix $\mathbf{V}_t$ is transmitted to the KF algorithm to estimate the obstacle velocity. If not, step 3 is repeated until convergence.

- *Estimation of obstacle velocity through the Kalman Filter algorithm*

The Kalman filter employs the results from the FCM algorithm to estimate the velocities of the obstacles. The motion model of an obstacle can be described as (Nguyen Trong & Kyoung Kwan, 2012),

$$\begin{cases} P(t+1) = P(t) + T_s \cdot V(t) + \dfrac{T_s^2}{2} \cdot A(t) \\ V(t+1) = V(t) + T_s \cdot A(t) \\ A(t+1) = A(t) + w(t) \end{cases} \tag{4B.17}$$

where $P(t+1) = \left[P_x(t+1) \quad P_y(t+1) \right]^T$ is the position of the obstacle;

$V(t+1) = \left[V_x(t+1) \quad V_y(t+1) \right]^T$ is the velocity of the obstacle;

$A(t+1) = \left[A_x(t+1) \quad A_y(t+1) \right]^T$ is the acceleration of the obstacle;

T_s is the sampling time; and *w(t)* is the Gaussian distribution noise.

The state of the vehicle, including its position, velocity, and speed, is defined as $\mathbf{X}(t)=\left[P^T(t) \quad V^T(t) \quad A^T(t)\right]$. Using (4B.17), the obstacle velocity at time t+1 is predicted as,

$$\mathbf{X}^{-}(t+1)=\mathbf{A}\cdot\mathbf{X}(t)+\mathbf{B}\cdot\mathbf{W}(t) \tag{4B.18}$$

where the minus superscript means the predict variable and $\mathbf{W}(t)$ is the noise vector.

The matrices **A** and **B** in (18) are determined from (4B.17) as,

$$\mathbf{A}=\begin{bmatrix} 1 & 0 & T_s & 0 & T_s^2/2 & 0 \\ 0 & 1 & 0 & T_s & 0 & T_s^2/2 \\ 0 & 0 & 1 & 0 & T_s & 0 \\ 0 & 0 & 0 & 1 & 0 & T_s \\ 0 & 0 & 0 & 0 & 1 & 0 \\ 0 & 0 & 0 & 0 & 0 & 1 \end{bmatrix} \text{ and } \mathbf{B}=\begin{bmatrix} 0 & 0 \\ 0 & 0 \\ 0 & 0 \\ 0 & 0 \\ 1 & 0 \\ 0 & 1 \end{bmatrix}$$

The observation model is presented as,

$$\mathbf{Z}(t)=\mathbf{H}\cdot\mathbf{X}(t)+\mathbf{V}(t) \tag{4B.19}$$

where $\mathbf{Z}(t)$ is the positions of the obstacles obtained through the FCM algorithm, $\mathbf{V}(t)$ is the measurement noise, and $\mathbf{H}$ is observation matrix given as,

$$\mathbf{H}=\begin{bmatrix} 1 & 0 & 0 & 0 & 0 & 0 \\ 0 & 1 & 0 & 0 & 0 & 0 \end{bmatrix}.$$

The velocity of an obstacle is then estimated through the following steps.

<u>Step 1</u>: Define the initiate vector and matrix

Covariance matrix of error $\mathbf{P}(0)=E\left[\left(\mathbf{X}(0)-\hat{\mathbf{X}}(0)\right)\left(\mathbf{X}(0)-\hat{\mathbf{X}}(0)\right)^T\right]$

Initial state vector $\mathbf{X}(0)=\left[P^T(0) \quad V^T(0) \quad A^T(0)\right]$

<u>Step 2</u>: Calculate the Kalman gain

The Kalman gain is calculated as,

$$\mathbf{K}(t)=\mathbf{P}^{-}(t)\cdot\mathbf{H}(t)^T\left(\mathbf{H}(t)\cdot\mathbf{P}^{-}(t)\cdot\mathbf{H}(t)^T+\mathbf{R}(t)\right)^{-1} \tag{4B.20}$$

where $\mathbf{K}(t)$ is a 6x2 Kalman gain matrix.

<u>Step 3</u>: Estimate the state vector

The new state vector is updated through the following formula,

$$\hat{\mathbf{X}}(t) = \hat{\mathbf{X}}^{-}(t) + \mathbf{K}(t)\left[\mathbf{Z}(t) - \mathbf{H}\cdot\hat{\mathbf{X}}^{-}(t)\right]$$
$$\mathbf{P}(t) = \left(\mathbf{I} - \mathbf{K}(t)\cdot\mathbf{H}(t)\right)\cdot\mathbf{P}^{-}(t) \quad (4B.21)$$

<u>Step 4:</u> Update the error covariance matrix

$$\mathbf{P}^{-}(t+1) = \mathbf{A}\cdot\mathbf{P}(t)\cdot\mathbf{A}^{T} + \mathbf{Q} \quad (4B.22)$$

The obstacle velocity $V(t)$ in vector state is then used to calculate the value of APF.

4B.4 Virtual Reality (VR) simulation of a ROV haptic driving system

4B.4.1 Numerical-based ROV and VR environment

Before applying the proposed haptic control strategy to an actual ROV, it was first tested within a VR simulation by coupling a physical haptic joystick controller to the simulation of the ROV and its associated control systems. The overview of the control structure of the simulation programme is similar to that described in **Fig. 4B.1**, with the exception that the physical vehicle is replaced by a numerical representation of the ROV, consisting of the relevant kinematics and kinetics models. The 2D scanning sensor is also simulated based on the specifications given in **Table 4B.1**. The ROV kinetics model presents the relationship between the forces from the thrusters and the velocity of the vehicle, which is given by the following equation (Fossen, 2011),

$$\mathbf{M}\dot{\mathbf{v}} + \mathbf{C}(\mathbf{v})\mathbf{v} + \mathbf{D}(\mathbf{v})\mathbf{v} + \mathbf{G}(\eta) = \mathbf{T} \quad (4B.23)$$

where $\mathbf{M}$ is the system inertia matrix (including the added mass), $\mathbf{C}(\mathbf{v})$ is the Coriolis centripetal matrix (including added mass), $\mathbf{D}(\mathbf{v})$ is the damping matrix, $\mathbf{G}(\eta)$ is the gravitational and buoyancy forces and moments vector, and $\mathbf{T}$ is the input thrust vector of ROV.

The position and pose of the ROV within the fixed frame are calculated based on the ROV kinematics using,

$$\dot{\boldsymbol{\eta}} = \mathbf{J}_{\Theta}(\boldsymbol{\eta})\mathbf{v} \quad (4B.24)$$

where $\boldsymbol{\eta} = [x, y, z, \phi, \theta, \psi]^{T}$ and $\mathbf{v} = [u, v, w, p, q, r]^{T}$ are the position (x, y, z), Euler angles (ϕ, θ, ψ), and velocity $[u, v, w, p, q, r]$ vectors respectively, while J_{Θ} is the transformation matrix. Details of the matrices in equations (4B.23) and (4B.24) were presented previously by the authors in(K. Le, H. Nguyen, & S. Ranmuthugala, 2013; Le, Hung Duc, Ranthumugala, & Forrest, 2014).

The ROV kinetics and kinematics are linked with the animation model to provide real time visual feedback of the vehicle in relation to the surrounding environment. The ROV model and its operating environments were designed using Virtual Reality Modelling Language (VRML) and exported into

the simulation programmes(K. Le et al., 2013). **Fig. 4B.7** presents the external and camera views of the VR operating environment.

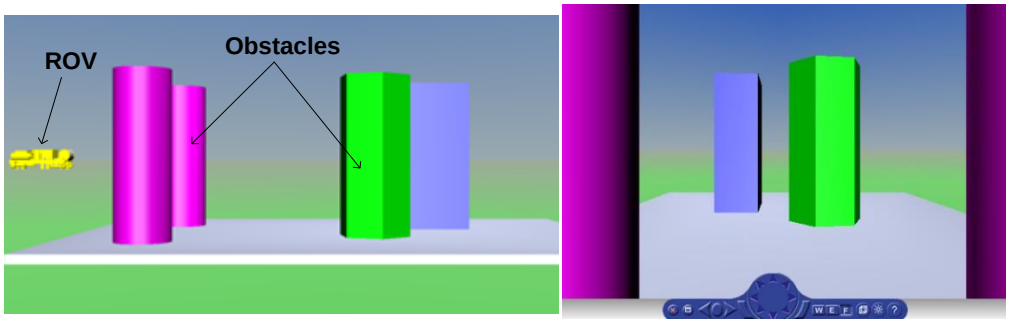

Fig. 4B.7 External view and ROV camera view in VRML

4B.4.2 ROV haptic driving system

The haptic joystick consists of two joystick levers used to control the surge and yaw motions of the ROV (see **Fig. 4B.8**), consisting of two main functions: controlling the ROV following pilot commands and providing information of obstacles surrounding the ROV over the haptic feedback force to pilots. The former functions conveys the pilots commands, including surge speed and yaw rates, to the control unit by generating the reference signals that are proportional to the displacement of the joystick levers. The motion control algorithm were designed to compare these reference signals to the actual surge speed and yaw rate of the ROV, obtained by a DVL and a gyroscope, to calculate the proper control signals for the thrusters, thus driving the ROV to follow the surge and yaw commands of pilots. Regarding the latter function , the haptic forces are generated by DC motors connected to the joystick via a shaft coupling. The states of the DC motors, including the shaft rotational speeds and electrical currents, are utilised to estimate the generated torque, which is then fed back to the torque controller. The torque controller generates the control signals to the DC motor drive based on the errors between the estimated torques and the reference signals resulted from the APF algorithm. The output torques generated from the joystick enable pilots to feel the haptic forces representing the external hazards. The design and fabrication of the controller and the haptic driving system are described in detail by the authors in(Le et al., 2014).

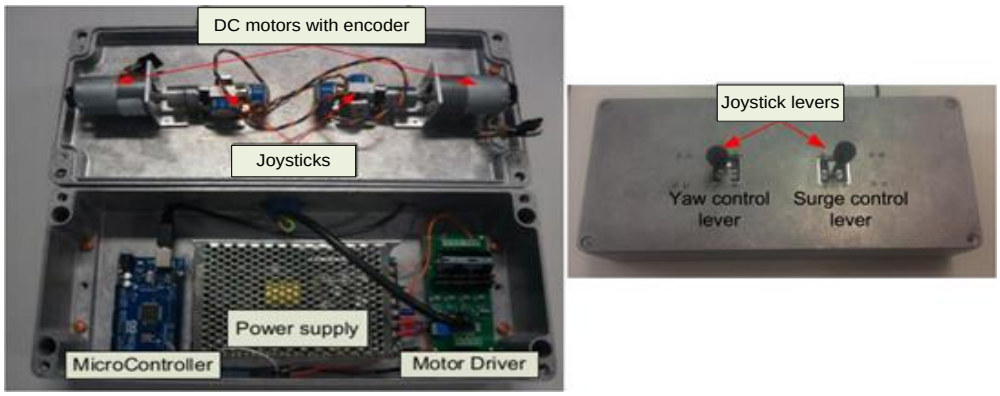

Fig. 4B.8 Layout of the haptic driving system within the joystick controller

4B.5 Simulation Results

Two simulation programs were designed to test the obstacle detection performance of the coupled FCM-KF algorithm and the haptic control performance within a real-time simulation environment. The former verifies the accuracy of the coupled FCM-KF by processing the simulated data from a laser-based scanning sensor. White noise was added to the sensor reading to improve the reality of the simulation. Next, the APF algorithm was applied to the ROV haptic drive system to control the vehicle in complex environment consisting of both stationary and dynamic obstacles. The aim of the latter simulation is to check whether the final risk avoidance vector, calculated from APF algorithm, could reflect the threat presented by obstacles to ROV pilots.

4B.5.1 Simulation 1: obstacle detection

In this simulation, the obstacle detection performance of the coupled FCM-KF algorithm was evaluated. The testing environment included two static (Obs1 and Obs2) and one moving (Obs3) obstacles as shown in **Fig. 4B.9**, with the relevant locations and dimensions given in **Table 4B.2**. The ROV equipped with the scanning sensor was located at the origin of the fixed frame and remained stationary. The three obstacles are always maintained within the range of the scanning sensor, which is 3.5m, ensuring that the obstacle measuring data from the scanning sensor are continuously acquired.

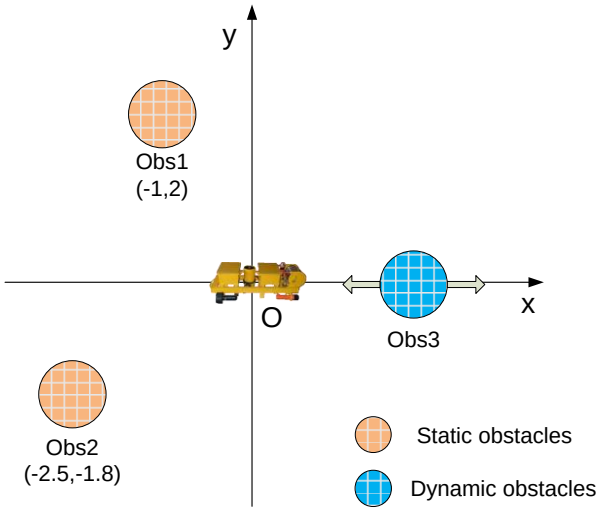

Fig. 4B.9 Testing environment for Simulation 1

Table 4B.2 Obstacle information for Simulation 1

Obstacle name	State	Position/Motion	Dimension
Obs1	Static	x = -1, y = 2	R = 0.3 m
Obs2	Static	x = -2.5, y = -1.8	R = 0.3 m

Obs3	Dynamic	Moving from [0.5, 0] to [3.5, 0] $x = 1.5\sin(0.5t) + 2;$ $y = 0;$	R = 0.4 m

The parameters of coupled FCM-KF algorithm used in the simulation are given in **Table 4B.3**. Two iteration termination conditions for the FCM algorithm, namely the iteration error and the maximum iteration, are set to guarantee the timing constraint of the real-time programme. The FCM algorithm stops and transmits the results to the KF algorithm as soon as one of these conditions are met.

Table 4B.3 Parameters of the coupled FCM-KF algorithm for Simulation 1

Sampling time	0.03s
FCM	Iteration error: 0.0001
	Maximum iteration: 50
KF	Process noise covariance: Q=50*eye(5)
	Measurement noise covariance: R=2*eye(2)

The positions of the obstacles identified by the FCM algorithm are shown in **Fig. 4B.10**. The position errors of the Obs1 and Obs2 are around ± 0.005m and ± 0.01m/s respectively. The difference is due to the number of the scanning ray reflected from each of these obstacles. Although Obs1 and Obs2 are of the same dimensions, Obs2 is located further away from the ROV than Obs1. As a result of this variation, the number of scanning rays returned from Obs1 and Obs2 are 700 and 450 respectively, with the higher data input from Obs1 ensuring greater accuracy from the FCM algorithm and thus a smaller error. This effect is clearly seen with the moving obstacle, Obs3. **Fig. 4B.10c** shows that Obs3 periodically moves along the X axis between (0.5, 0) and (3.5, 0) at an angular frequency of $\omega = 0.5\,\text{rad/s}$. The estimation of the position error of Obs3is shown in **Fig. 4B.11**, which also varies at the same frequency, with the error increasing as Obs3 moves further away from the ROV. This demonstrates that the obstacle detection accuracy does not remain constant, but varies with the dimensions and locations of the individual obstacles, with smaller and more distant obstacles being harder to accurately identify and locate.

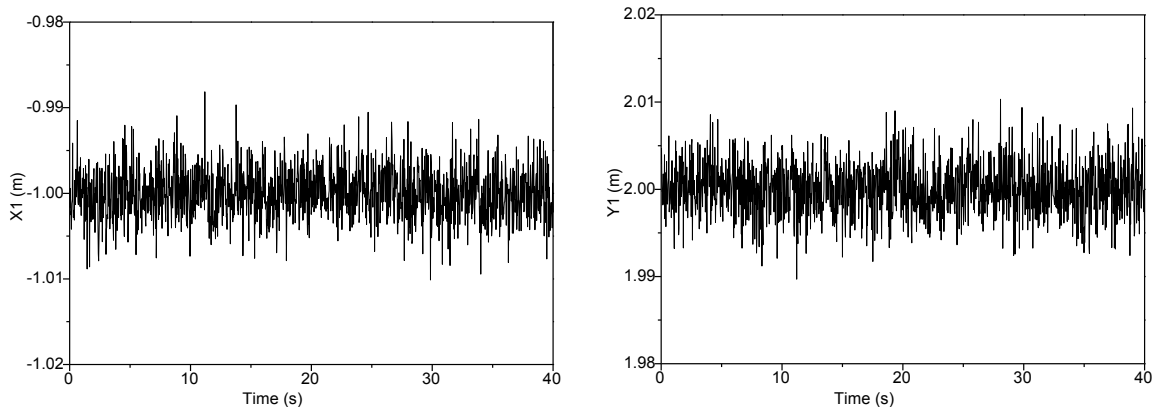

a. Estimated position of Obs1

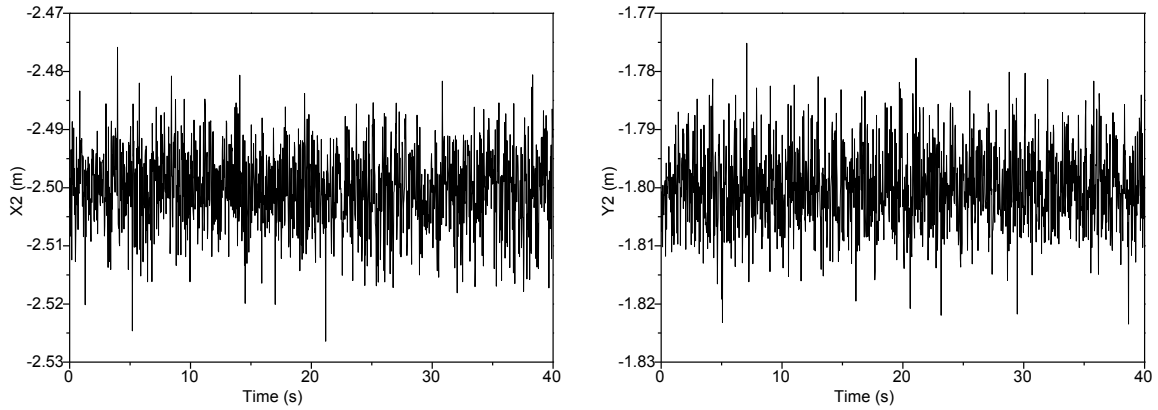

b. Estimated position of Obs2

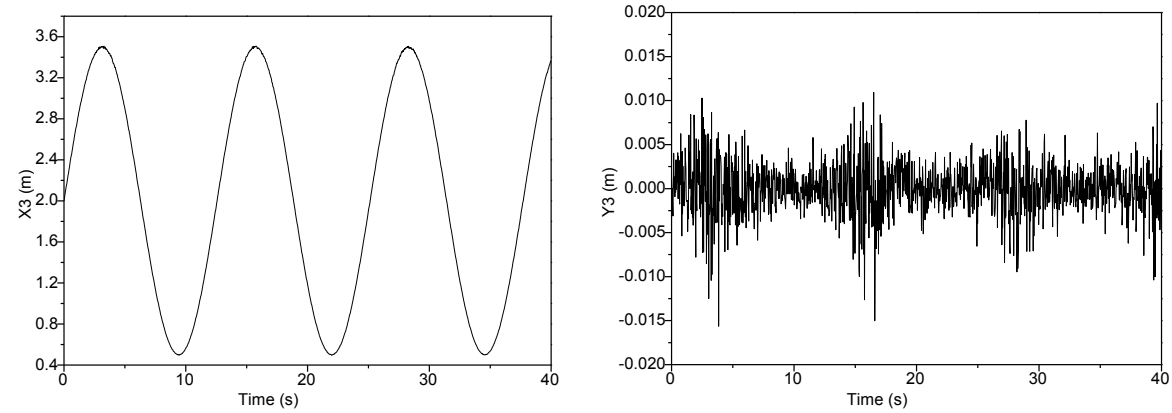

c. Estimated position of Obs3

Fig. 4B.10 Obstacle positions estimated by the FCM algorithm

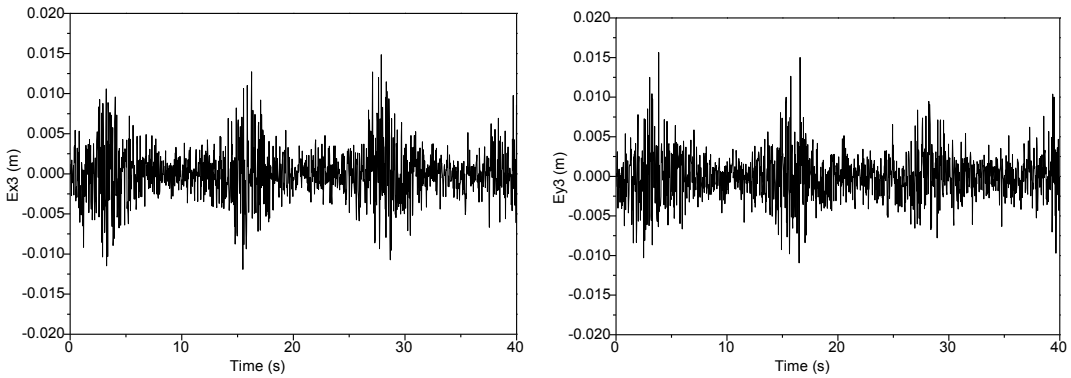

Fig. 4B.11 Position errors, Ex3 and Ey3, of the dynamic obstacle, Obs3

The KF algorithm employs the position estimated results from the FCM algorithm to determine the velocities of the obstacles. **Fig. 4B.12** shows that the velocity estimated errors of Obs1 and Obs2 are ± 0.002m/s and ± 0.004m/s respectively. The difference is due to the accuracy of the input data which is the obstacle positions identified by the preceding FCM algorithm. The velocity estimated error of Obs3 varies from ± 0.01 to ± 0.04m/s, which is larger than those of the static obstacles due to the effect of the inaccuracy of the obstacle motion model given in (4B.17) on the KF estimation process. Nevertheless, the errors are relatively small, thus the results of the coupled FCM-KF algorithm can be utilised to calculate the risk avoidance vector by applying the APF formula in (4B.1).

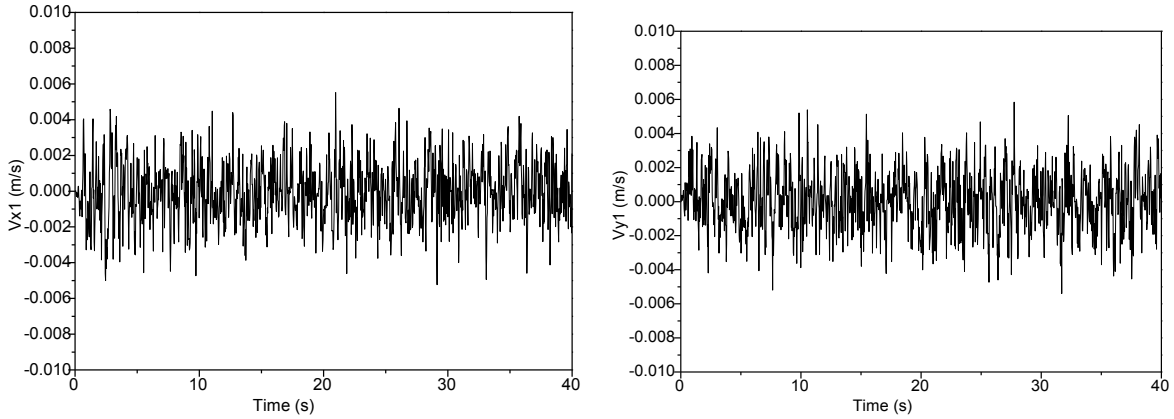

a. Estimated velocity of Obs1

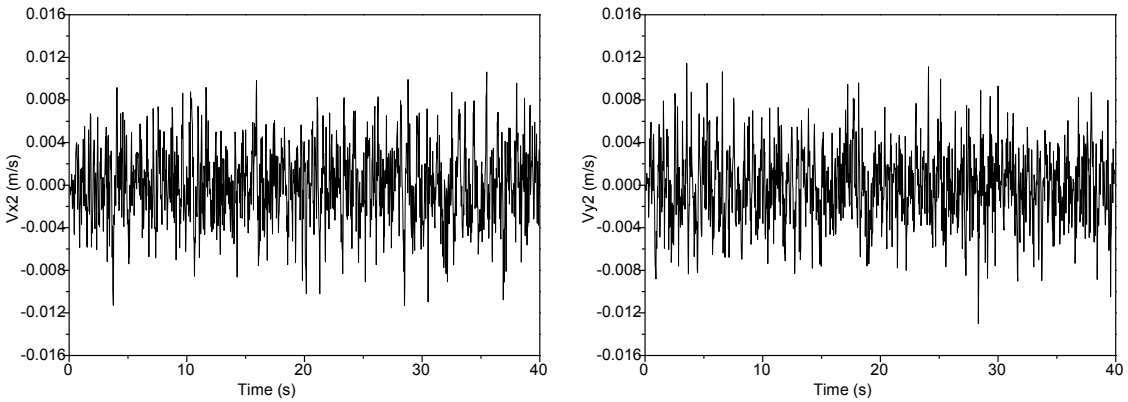

b. Estimated velocity of Obs2

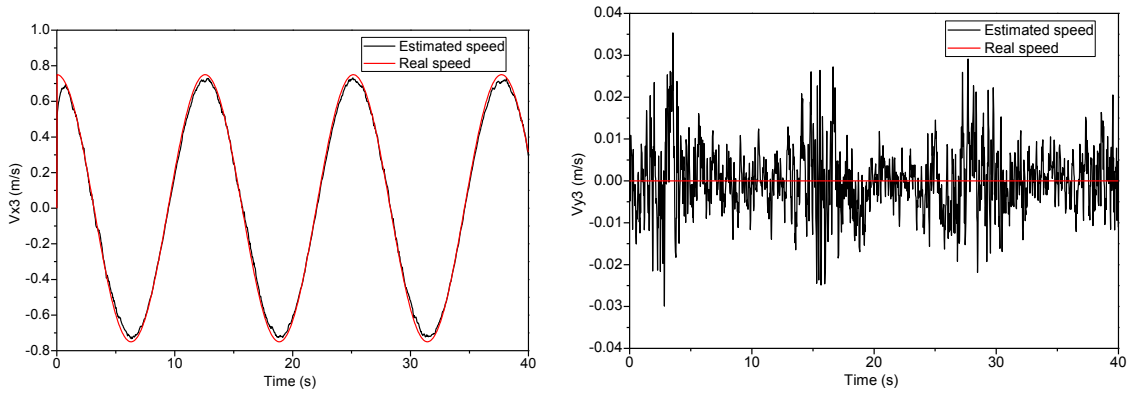

c. Estimated velocity of Obs3

Fig. 4B.12 Obstacle velocities estimated by the KF algorithm

Fig. 4B.13a presents the danger levels on the ROV due to the individual obstacles obtained using the amplitude of the risk avoidance vectors. The static obstacles Obs1 and Obs2 present constant danger levels, while the dynamic obstacle Obs3 due to its sinusoidal motion presents a periodically varying danger level as shown in **Fig. 4B.13b**. The maximum APF danger level is 0.56 when $v_i = 0.17m/s$ and $d_i = 0.53m$, while the minimum of 0.03 corresponds to $v_i = -0.71m/s$ and $d_i = 2.32m$. The obstacles in close proximity to the ROV with positive relative velocities will impose a greater hazards to the vehicle and will thus be reflected with a higher danger level.

The max-min strategy combines the danger levels from all obstacles to determine the final risk avoidance vector, with its amplitude shown in **Fig. 4B.13c**. From 0 to 4.6 seconds the final risk avoidance vector is reflective of Obs1, as it is the dominant hazard. However as Obs3 approaches the ROV with a positive relative velocity, its risk vector amplitude rapidly increases surpasses that of Obs1 and thus is reflected in the final avoidance vector.

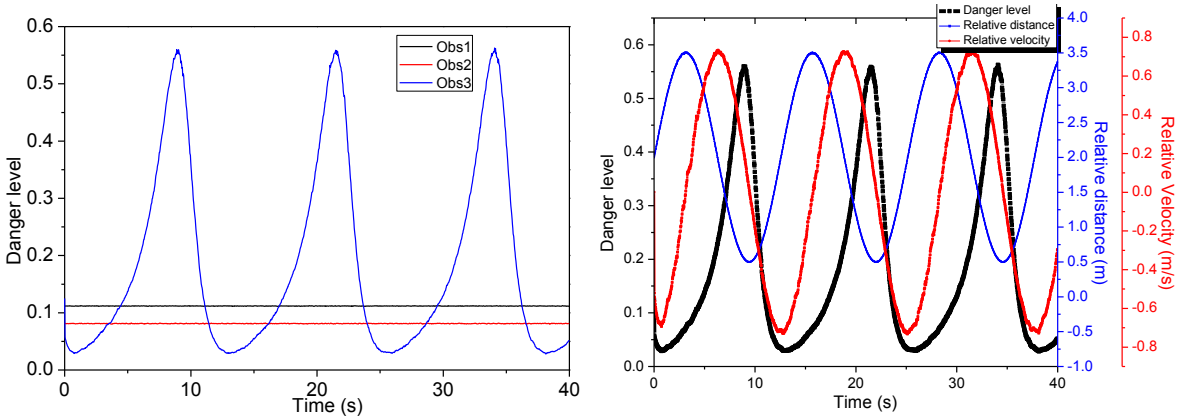

a. Danger level of each obstacle

b. Danger level of Obs3

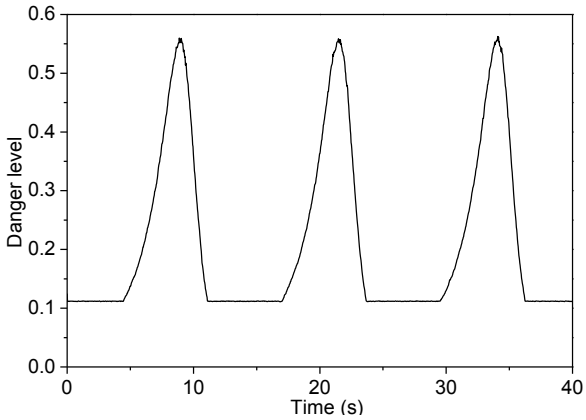

c. Final danger level

Fig. 4B.13. Danger level represented by the APF in Simulation 1

Fig. 4B.14 presents the risk avoidance vector components $\mathbf{P_u}$ and $\mathbf{P_r}$ calculated from equation (4B.5). From 4.6 to 11 seconds the value of $\mathbf{P_r}$ is zero as Obs3, which presents the highest hazard at during this period, moves only along the X axis, which coincides with the ROV's heading. It means that there is only the repulsive force, generated by the surge control lever. The negative value of $\mathbf{P_u}$ during this period represents the haptic force that tends to push the ROV back to prevent collision with Obs3. As Obs3 moves away from the ROV between 11 to 16 seconds, Obs1 now becomes the dominant hazard to the ROV (**Fig. 4B.13a**), thus representing the final risk avoidance vector, which due to its position will influence both $\mathbf{P_u}$ and $\mathbf{P_r}$. **Fig. 4B.14** shows that the values of $\mathbf{P_r}$ is now non-zero, which will results in a haptic force that acts on the yaw control lever to prompt the pilot to turns the ROV in an clockwise direction to avoid Obs1. In addition, the positive value of $\mathbf{P_u}$ will prompt the pilot to move forward to reduce the collision potential with Obs1 (see **Fig. 4B.9**).

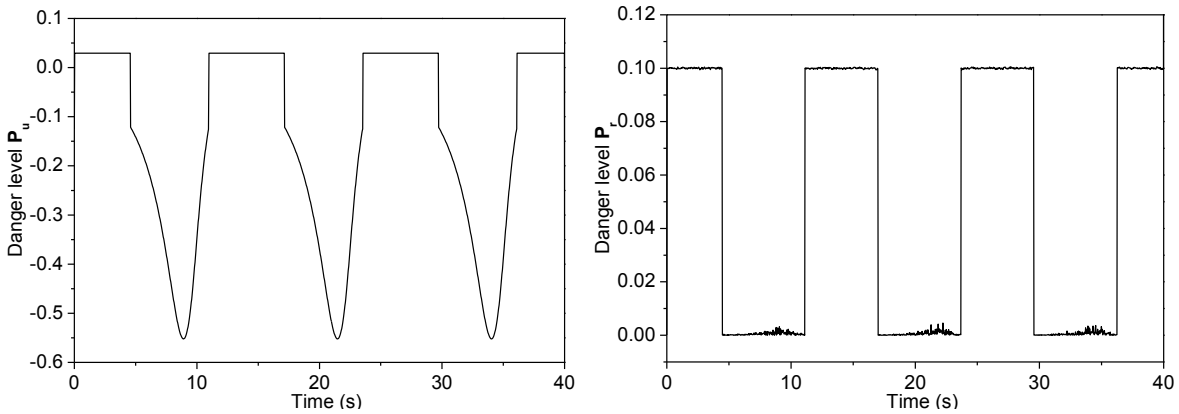

Fig. 4B.14. Danger level represented by the APF in surge and yaw direction of Simulation 1

4B.5.2 Simulation 2: ROV to follow a pre-defined path

In this simulation, the ROV pilot is tasked to use the haptic joystick and the visual feedback to manoeuvre the simulated ROV to follow a pre-defined path comprising of stipulated waypoints. **Fig. 4B.15** depicts the tracking path and the waypoint coordinates, with the ROV starting at the origin of

the fixed frame and sequentially approaching Waypoint 1 and Waypoint 2 before finally reaching the destination. A number of static and moving obstacles are also present within the operating environment, with their relevant information given in **Table 4B.4**.

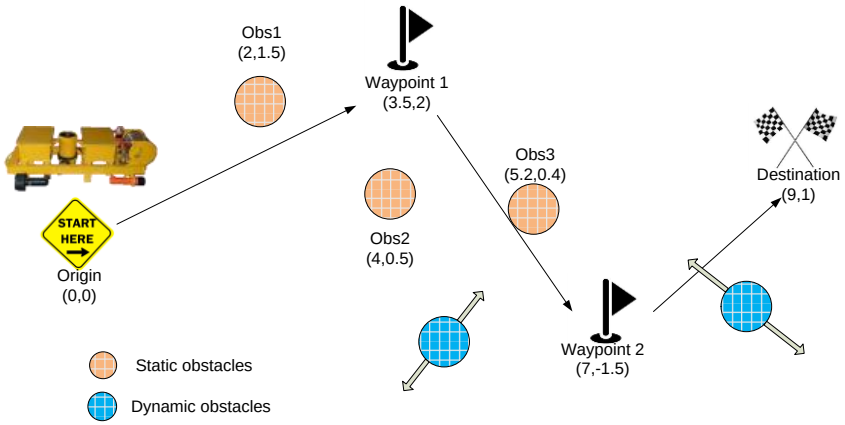

Fig. 4B.15 Working environment for Simulation 2

Table 4B.4 Obstacle information for simulation 2

Obstacle name	**Status**	**Position/Motion**	**Dimension**
Obs1	Static	x = 2, y = 1.5	R = 0.3 m
Obs2	Static	x = 4, y = 0.5	R = 0.3 m
Obs3	Static	x = 5.2, y = 0.4	R = 0.3 m
Obs4	Dynamic	Moving from [5, -1] to [7, 1.5] $x = \sin(0.5 \cdot t) + 6,\ y = 1.25\sin(0.5 \cdot t) + 0.5$	R = 0.3 m
Obs5	Dynamic	Moving from [8, -1] to [7, 1] $x = -0.5\sin(0.6 \cdot t) + 7.5,\ y = \sin(0.6 \cdot t)$	R = 0.3 m

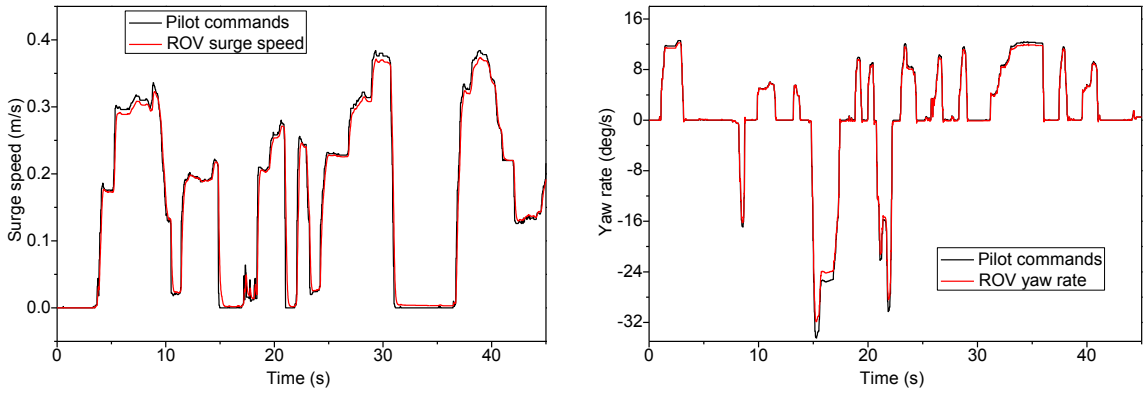

a. Surge motion response b. Yaw motion response

Fig. 4B.16. ROV response to pilot's joystick commands

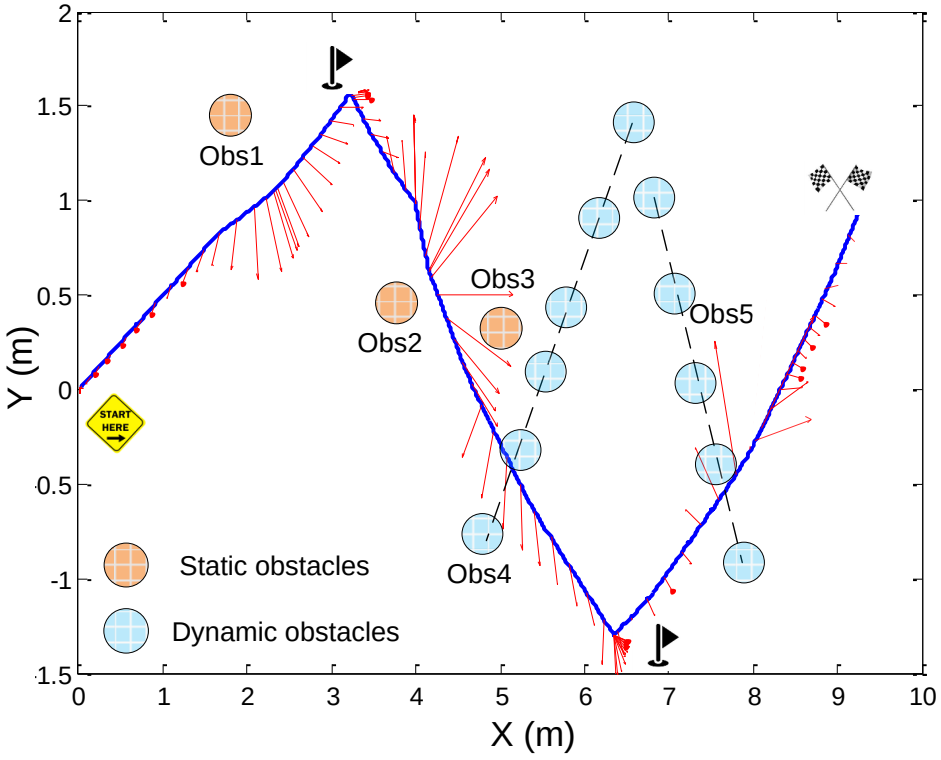

Fig. 4B.17. Trajectory of the simulated ROV and the associated risk avoidance vectors (in red)

Fig. 4B.16 presents the ROV responses in surge and yaw under the commands of the pilot. The errors between the actual ROV responses and the reference signals are relatively small being 0.05m/s and 2deg/s for surge and yaw motions respectively. This implies that the ROV controller is capable of driving the vehicle to follow the pilot's commands.

The actual ROV path starting from the fixed frame origin, reaching the two waypoints, and terminating at the destination without colliding with any of the obstacles is shown in **Fig. 4B.17**. The risk avoidance vectors are also plotted as red arrows at the appropriate locations along the ROV path.

The directions of the vectors always point away from the hazards, with its amplitude proportional to the danger level presented by the obstacles.

The danger levels caused by the obstacles within the environment are presented in **Fig. 4B.18a**, where the maximum value is reached twice during the mission, with the first occurring between 23 and 27 seconds while the second occurs between 37 and 42 seconds. The former occurs as the ROV passes through the gap between Obs2 and Obs3. Since the ROV moves closer to Obs2 than Obs3, the risk avoidance vector of Obs2 (with its danger level amplitude represented by the red line in **Fig. 4B.18b**) becomes the final risk avoidance vector. This, when passing Obs2 and Obs3, the direction of the final avoidance vector pushes the ROV away from Obs2. As the ROV moves away from Obs2, the avoidance vector presented by this obstacle weakens that it is surpassed by the threat level caused by Obs3 in the 26th second (as seen from **Fig. 4B.18b**, that the blue line cuts and overtakes the red line in this moment). Because Obs3 presents the highest potential threat to the ROV from 26 to 31 seconds, it dominates the final risk avoidance vector, thus the final vector changes direction, pushing the ROV towards the left side of the fixed-frame coordinate. In the second case, the hazard is due to the dynamic obstacle Obs5, whose danger level amplitude is presented by the purple line in **Fig. 4B.18b**. The sudden increase of the danger level of Obs5 from 0.1 to 1 around the 38 second mark indicates that Obs5 is approaching the ROV rapidly increasing the threat level.

Although the moving obstacle Obs4 crosses the ROV's path as shown in **Fig. 4B.17**, its danger level (green line) plotted in **Fig. 4B.18b** shows that it dominates the final risk avoidance vector for only a short period of time, i.e. from 33 to 38 seconds, while its danger level is relatively low at around 0.2. This is due to the relatively large distance between the ROV and Obs4 and as the latter moving away from the ROV.

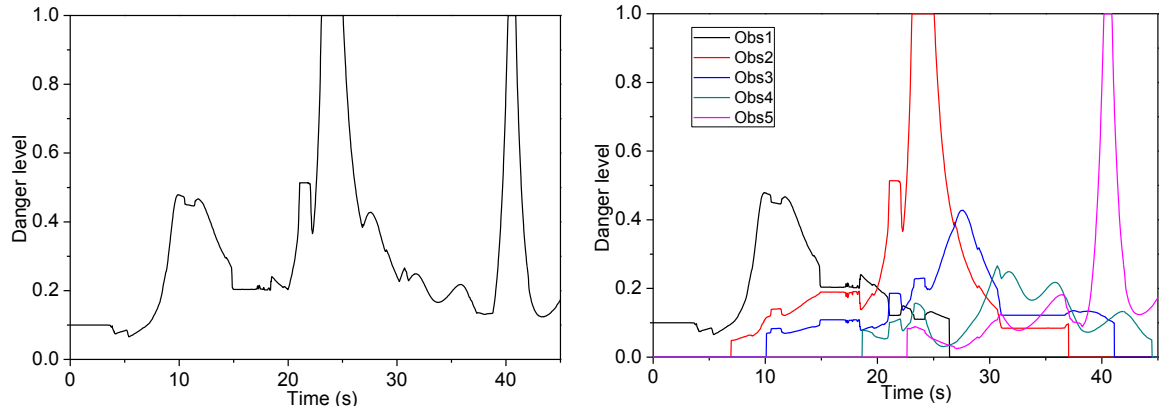

a. Final danger level b. Danger level of each obstacle

Fig. 4B. 18. Danger level represented by the APF in Simulation 2

The final risk avoidance vector is divided into the two elements $\mathbf{P_u}$ and $\mathbf{P_r}$ as shown in **Fig. 4B.19**. These elements are then converted into the respective reference signals for the haptic force controllers

by multiplying them by the haptic feedback gains. **Fig. 4B.20** presents the haptic torque created by the actuators within the joystick. It is seen that the error between the reference signals and joystick response is relatively small at around 0.02 Nm. This indicates that the haptic controller has the ability to replicate the potential hazard presented by obstacles via the haptic torques acting back on the joysticks.

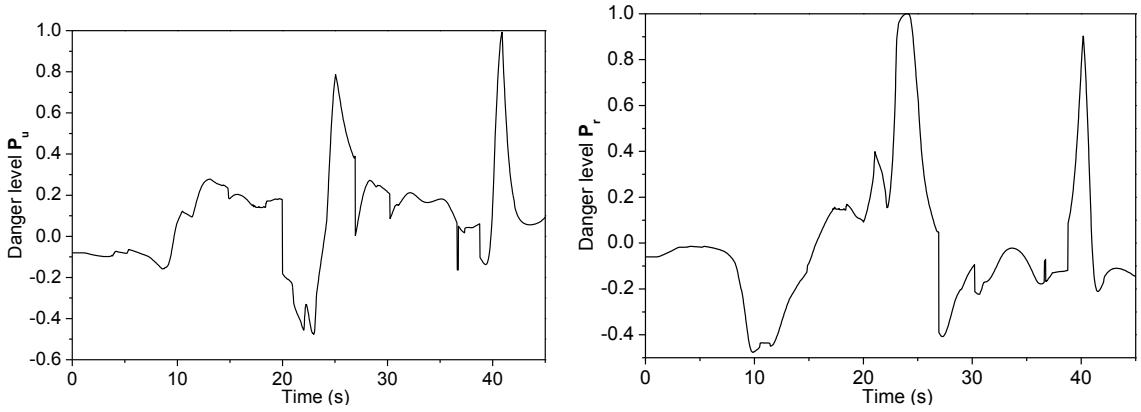

Fig. 4B.19. Danger level described by APF in surge and yaw motion of Simulation 2

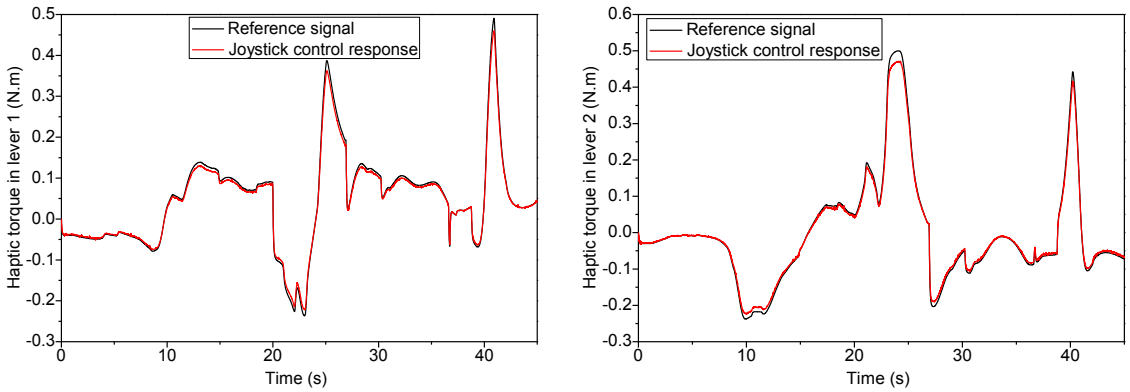

Fig. 4B.20. Haptic joystick responses

4B.6 Conclusion

This paper has shown how the novel APF technique is applied to a ROV haptic driving system to assist the pilot in collision avoidance during missions in operating environments consisting of stationary and moving obstacles. By including a coupled FCM-KF algorithm, the proposed APF has the ability to model the potential risk presented by both types of obstacles. The effectiveness of the proposed technique was verified by conducting simulations of the ROV within a virtual reality environment, with the simulated vehicle controlled by a haptic joystick. The simulation results indicated that the coupled FCM-KF algorithm is sufficiently effective and robust to be applied to real-time control. Although the performance of the coupled FCM-KF algorithm depends on the size and distance of obstacles to the ROV, the accuracy of the algorithm is acceptable as the estimated errors are small. The final risk avoidance vector calculated from the APF algorithm provides ROV pilots

with an indication of the danger level of obstacles in the vicinity of the ROV and prompts through the joystick the direction to avoid collision. Consequently, the haptic driving system can improve the safety of the ROV manoeuvring in cluttered environments.

Future work is planned to test the system on a free running physical ROV in an actual operational environments to fully evaluate the effectiveness of the ROV haptic driving system.

Chapter 5: Robust Model Reference Adaptive Control for Remotely Operated Vehicles Haptic Drive System

Chapter 5 presents the development of a novel robust adaptive control algorithm for a haptic controller of an ROV to deal with uncertainty, the nonlinear characteristic of the haptic drive system and the time delay caused by data transmission. The proposed algorithm was applied to a 3-DOF Falcon haptic joystick to control the AMC-ROV-V described in Chapter 2-part B to validate the effectiveness.

This chapter has been submitted for publication in the Journal of IEEE Transactions on Haptics and at the time of writing is under review. The citation of the research article is:

Le, KD and Nguyen, HD and Ranmuthugala, D and Forrest, AL, Robust Model Reference Adaptive Control for Remotely Operated Vehicles Haptic Drive System, IEEE Transactions on Haptics [Under review 2016]

Abstract

This paper presents the development of a robust adaptive control algorithm for a haptic controller of an underwater Remotely Operated Vehicle (ROV) to deal with disturbances, the nonlinear characteristic of the system and the time delay caused by data transmission. These factors are found to cause adverse effects on the performance of the haptic control in terms of the transparency and the stability of tele-operation control systems, resulting in the inaccuracy of ROV manipulation, which in extreme cases can lead to obstacle collision and mission failure. To address these issues, the novel control algorithm is proposed, consisting of a robust control technique, named Quantitative Feedback Theory (QFT), and a Model Reference Adaptive Control (MRAC) algorithm, and applied to control the actuators incorporated within a haptic joystick. The comparison of the Robust Model Reference Adaptive Control (RMRAC) technique and other algorithms was carried out on both the simulated and physical ROV models to verify the effectiveness and merits. The results indicated that RMRAC not only maintained the stability of the ROV drive system but also improved the performance by reducing the overshoot and settling time of the force responses, and thus ameliorating the haptic feedback quality.

Keywords: ROV haptic control, robust control, QFT, MRAC.

5.1 Introduction

Due to the lack of 3-D information and limitations with quality and the field vision of the cameras, ROV pilots are not always able to observe and identify external hazards purely on visual feedback, especially when the ROVs are operating in environments littered with obstacles, resulting in collisions. A potential solution is to add one or more feedback sensors to assist pilots to safely manoeuvre the ROV through the surrounding hazards. One option with regard to tele-operation control is a technique called haptic control, which includes a tactile user interface that can enhance the operator's awareness of the working environment and improve the performance. The virtues of a tactile user interface are that it allows pilots to feel as if they are directly interacting with the working environment. The haptic technology was first applied to tele-operation control systems for robotic manipulators for various purposes, such as surgeon training, endoscopic operation and construction, and has recently begun to be employed in controlling mobile systems, such as terrain robots, aerial and underwater vehicles (Brandt & Colton, 2010; Lam, 2009; Rösch, Schilling, & Roth, 2002; Ryu, Song, Cho, Kang, & Kim, 2010; Sangyoon, Sukhatme, Jounghyun, & Chan-Mo, 2002).

The transparency and the stability characteristics are two main criteria to quantify the quality of the haptic controller. Vlachos and Papadopoulos defined the transparent characteristic as a haptic users' feeling of the absence of haptic device parasitic forces, such as inertia, gravity, and friction, during control operations (Vlachos & Papadopoulos, 2006). In other words, the greater the transparency of the haptic system, the more realistic the feeling that the haptic users will experience. Meanwhile,

stability is a prime concern in haptic control systems because an unstable system not only causes misleading feedback information but also increases the workload for pilots (Lam, 2009), leading to inaccurate driving decisions that culminate in mission failure or even complete damage of the system in the worst cases. Due to these critical effects, previous research has been devoted to improving the transparency and maintaining the stability of the haptic system, which can be categorised into two main approaches: hardware optimisation and advanced control application.

In the former approach, the authors (Hayward, Choksi, Lanvin, & Ramstein, 1994; Kurtz & Hayward, 1992; Vlachos & Papadopoulos, 2006) optimised the mechanical parameters of multi-DOF haptic mechanisms by focusing on endpoint side fidelity to mitigate the effects of parasitic forces. Meli et al. used a strategy called sensory subtraction to eliminate the effects of non-kinaesthetic feedback and to improve the transparency in the bimanual haptic interaction (Meli, Pacchierotti, & Prattichizzo, 2014). The application of their technique in controlling a 7-DOF haptic mechanism showed remarkable results for the completion time, and the force exerted bythe haptic users was relatively small, regardless of the communication delay. Jian Li et al. improved the tele-operation performance using haptic devices with complementary degrees of freedom (DOF). Their experimental results from using two 1-DOF and 2-DOF master haptic devices to control a 3-DOF slave robot provided more stable and more accurate tracking performance than a non-split haptic system in which the slave robot was controlled by a 3-DOF joystick (Jian, Tavakoli, & Qi, 2014c). Baser et al. implemented both active and passive actuators on a 1-DOF haptic device to improve the stable impedance and transparency characteristics (Baser, Gurocak, & Konukseven, 2013).

In the latter approach, haptic control algorithms, which are based on the permanent haptic hardware, were more focused. Abdossalami et al. implemented Lyapunov analysis to develop an adaptive nonlinear controller that overcame the uncertain dynamics of the haptic devices. The controller successfully maintained the stability in both impedance-based and admittance-based haptic control experiments (Abdossalami & Sirouspour, 2009). To ensure the stability of haptic systems under the effects of time delay, Natori et al. treated the time-varying delay as external disturbances which are estimated and compensated by a communication disturbance observer. The remarkable virtue of this technique is the ability to compensate the time-varying delay without the need for time-delay models (Natori, Tsuji, Ohnishi, Hace, & Jezernik, 2010). Other methodologies, such as penalty-based and Llewellyn's criterion, were also proposed to stabilise and improve the performance of haptic control systems (Jian, Tavakoli, & Qi, 2014a, 2014b; Li, Zhang, Ye, & Zhang, 2015). Nevertheless, most of the previous haptic research has focused on investigating the application of the haptic devices on a robotic manipulator or a virtual mass-spring-damper system, while very little has been done in analysing and designing a stable and responsive haptic controller for ROV drive systems, which are usually affected by a large scale of disturbances and highly nonlinear characteristics.

In this paper, a Robust Model Reference Adaptive Control (RMRAC) technique for a ROV haptic drive system is developed. The stability of the control system was achieved by the Quantitative Feedback Theory (QFT) synthesis methodology (Horowitz, 1993), whose principle is to determine the robust controller over a specified region of a control plant, in this case the ROV haptic drive system, in the frequency domain (Hwang & Yang, 2002). Due to the high adaptation rate, the Model Reference Adaptive Control (MRAC) algorithm (Sastry & Isidori, 1989; Tao, 2003) was combined with the QFT controller to improve the transparency of the haptic control system. The errors between the reference model and the actual states were employed to tune the parameters of the adaptive controller using a back propagation algorithm. The parasite forces affecting the haptic control quality, such as inertia of the joystick and Coulomb friction, were found to be compensated as these errors converge to zero, hence improving the transparency of the haptic feedback quality.

To verify the effectiveness of RMRAC, the technique was applied to the haptic control system including an observation class ROV and a 3-DOF haptic joystick. Both simulation and experimental results showed that the RMRAC technique provided adequate force tracking performance, good sensor noise rejection and robustness against the varying time delay.

5.2 ROV haptic drive system

The principle of a ROV haptic drive system is shown in **Fig. 5.1**, consisting of two main functions: controlling the ROV following pilot commands and providing information on the external environment such as drag, inertial force and distance to obstacles over the haptic feedback force to pilots. By grasping the joystick lever, pilots have the feeling as if they are directly interacting with ROVs within the working environment by sensing the resistance from the fluid caused by the damping force, added mass and the potential threat from obstacles represented by the virtual force. In other words, the haptic controller 'turns' the joystick into a virtual ROV, which possesses similar kinetic characteristics to the actual vehicle.

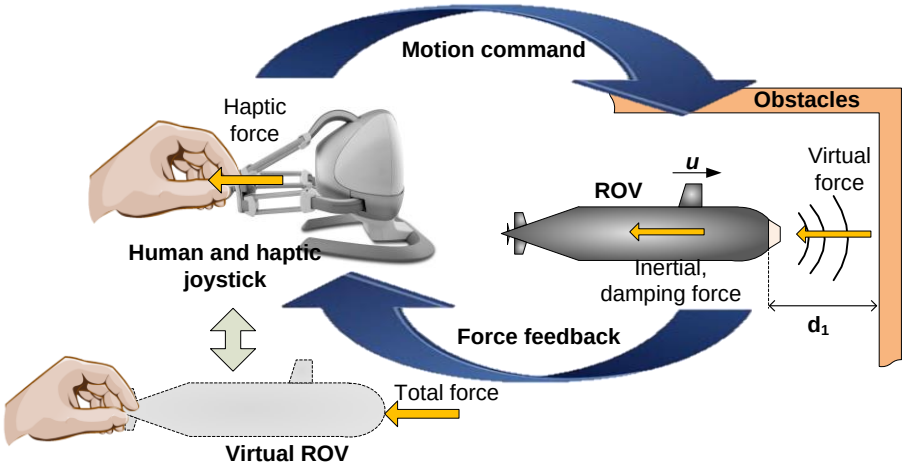

Fig. 5.1. ROV haptic drive system strategy

This research focuses on the haptic drive system in surge motion. First, the kinetics of the ROV and the haptic joystick are investigated to obtain insight into the effects of the relevant forces. The kinetic model of the ROV in surge motion is written as (Le, Nguyen, & Ranmuthugala, 2014)

$$m\dot{u}_r + cu_r|u_r| + d_{dis} = T \tag{5.1}$$

where u_r is the relative speed of the ROV in water, T is the thrust force of the horizontal thrusters, m is total mass including ROV and added mass in the surge direction, c is the hydrodynamic quadratic damping coefficients, and d_{dis} is the restoring force and external disturbances.

The virtual force presented by obstacles is given as (Farkhatdinov & Ryu, 2010)

$$f_{vir} = \begin{cases} k(d_o - d) & \text{with } d \le d_o \\ 0 & \text{with } d > d_o \end{cases} \tag{5.2}$$

where f_{vir}, k, d are the virtual force, virtual stiffness and distance from the vehicle to obstacles measured by the sonar sensor, respectively, and d_o is the boundary of the virtual force field where the force begins to impose on the ROV.

The total haptic feedback force transmitted from the ROV to the control station is calculated as

$$F_{haptic} = k_h\left(f_{vir} + m\dot{u}_r + cu_r|u_r|\right) \tag{5.3}$$

where k_h is the haptic feedback gain.

The kinetic equation of the haptic joystick can be expressed as follows (Polushin & Hasan, 2014)

$$M\ddot{x}_h + B\dot{x}_h + G(\dot{x}_h, x_h) = F_h - F_{motor} \tag{5.4}$$

where F_h and F_{motor} are the force given by the ROV pilots and the force of the actuators incorporated within the haptic joystick; M, B and G are the inertia, damping matrix and uncertain force of the dynamic model; and $\ddot{x}_h$, $\dot{x}_h$ and x_h are acceleration, velocity and position of the joystick lever controlled by the human hand.

The counterforce given by the haptic joystick to the ROV pilots is derived from equation (5.4) as

$$M\ddot{x}_h + B\dot{x}_h + G(\dot{x}_h, x_h) + F_{motor} = F_h \tag{5.5}$$

The goal of the haptic controller is to generate suitable control signals to the actuators to transmit the haptic feedback force, F_{haptic}, calculated in equation (5.3), to the sensation of the ROV pilots, leading to $F_h = F_{haptic}$. Combining equation (5.3) and (5.5), the dynamic equation of the ROV haptic drive system is then derived as

$$M\ddot{x}_h + B\dot{x}_h + G\left(\dot{x}_h, x_h\right) - k_h\left(f_{vir} + m\dot{u}_r + cu_r\left|u_r\right|\right) = F_{motor} \tag{5.6}$$

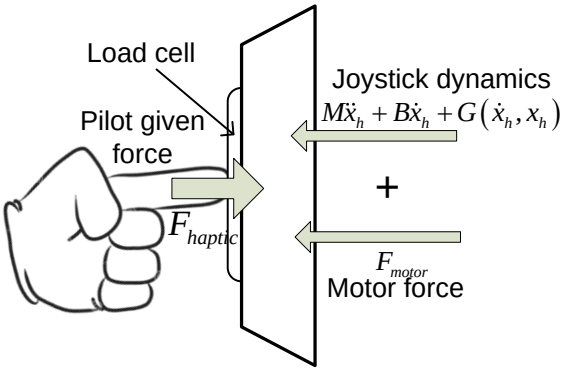

Fig. 5.2. Force analysis of pilot-joystick interaction

The force analysis of the pilot–joystick interaction is summarised in **Fig. 5.**2. To ensure the quality of the haptic performance, the haptic controllers are required to control the actuators to generate the proper force F_{motor} that makes the pilot–joystick interaction force measured by the load cell converge to the haptic feedback force given by (5.3). Intuitively, the haptic controller transmutes the joystick dynamics given in (5.4) into the ROV kinetics given in (5.1) to provide realistic tactile feedback to the pilots: the more similar those models are, the greater the transparency of the haptic system will be. Designing an effective haptic controller is not a straightforward task due to the high nonlinearity of the systems, and the parasite forces presented by inertia and Coulomb friction of the joystick lever, especially the time delay of the data transmission process, which affects the performance and the stability of the control system. To ensure the transparency and stability of the ROV haptic drive system, the paper develops a novel control algorithm named robust model reference adaptive control (RMRAC) which consists of two parts: a QFT controller and an adaptive controller based on a back propagation algorithm. The former controller has the ability to stabilise the system by dealing with uncertain parameters and varying time delay, while the latter is capable of self-adjusting the control parameters to reduce the error between the actual system and the ROV kinetic models, which is used as the reference model, thus increasing the transparency of the ROV drive haptic system.

The control block diagram of the ROV haptic drive system is presented in **Fig. 5.3**, consisting of two main closed-loop controls: a motion controller and a force controller equivalent to the two main functions of the haptic drive system. The former controller controls the motion of the ROV to follow commands given by pilots which is widely performed in conventional ROV drive systems; thus the focus of the research is on the application of the RMRAC technique on the latter controller.

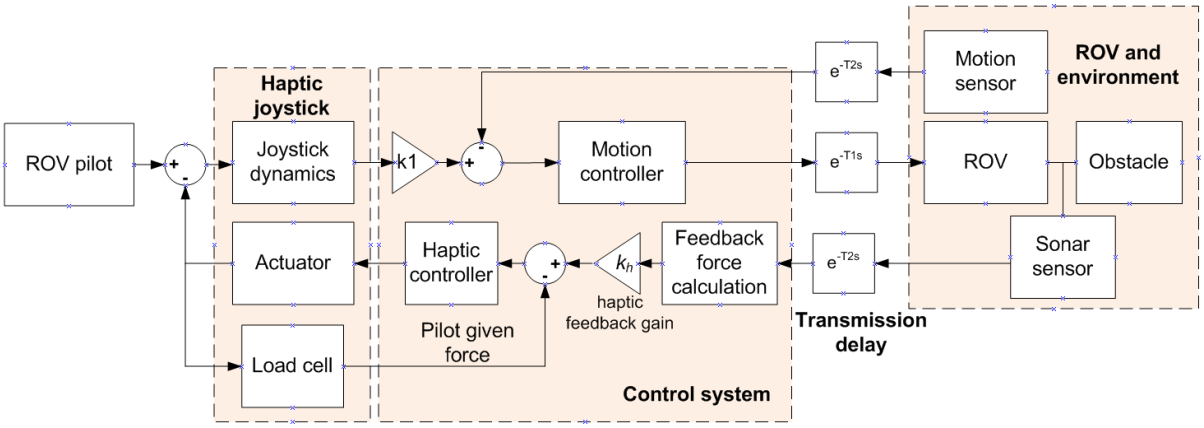

Fig. 5.3. Block diagram of ROV haptic drive system

5.3 RMRAC controller design

5.3.1 Overview of the control structure

As the work focuses on the haptic controller, the full control diagram of the haptic drive system in **Fig. 5.3** can be simplified to a single closed-loop control structure, as shown in **Fig. 5.4**, where the joystick, the ROV system and the motion controller are lumped together to form a new control plant whose input and output signals are the total force imposed on the joystick, including the force of the ROV pilots and the haptic actuators, and the haptic feedback force calculated by formula (5.3), respectively. The haptic controller generates appropriate control signals to the joystick actuators to balance the force given by the ROV pilots and the haptic feedback force, creating a tactile sensation for the pilots.

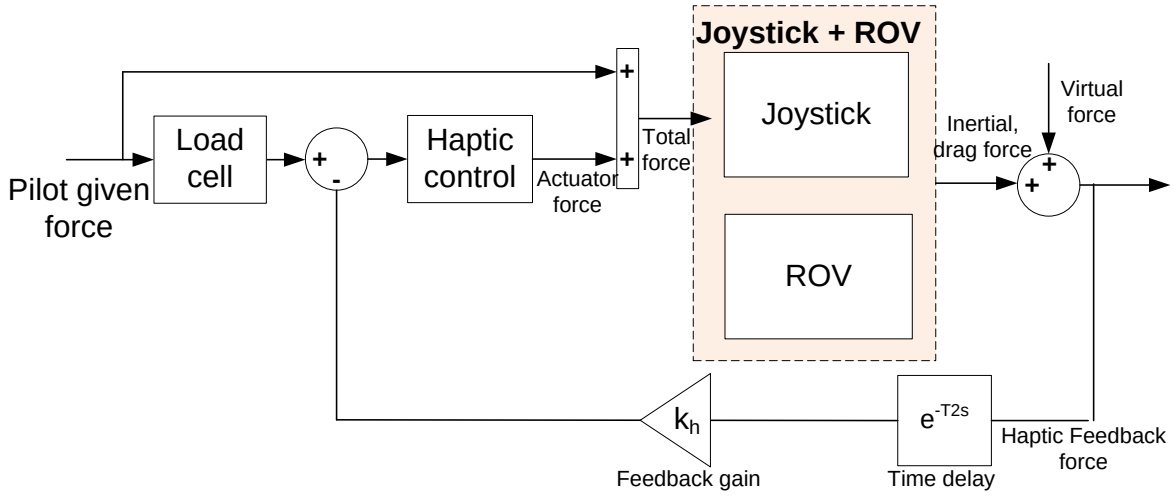

Fig. 5.4. Simplification of ROV haptic drive system diagram

The control plant shown in **Fig. 5.4** is highly nonlinear and contains various uncertain parameters such as time-varying delay (T_2), external disturbances and noise of the sensor data. Additionally, the pilot force and virtual force presenting hazards from obstacles can be considered as the input and

output disturbances that adversely affect the stability of the closed-loop control system. To ensure the stability and the transparency requirement, a RMRAC algorithm, including QFT and a neuralnetwork based MRAC controller, is designed and used as the main algorithm for the haptic controller due to the merits of the elemental algorithms: the QFT controller has the ability to control systems with large uncertainties and input/output disturbances, and requires neither an accurate mathematical model nor a transfer function of the control plant (Horowitz, 1993); and the MRAC algorithm adjusts the control signals to minimise the error between the ROV reference model and the control plant (see **Fig. 5.5**), increasing the reality of the haptic feedback.

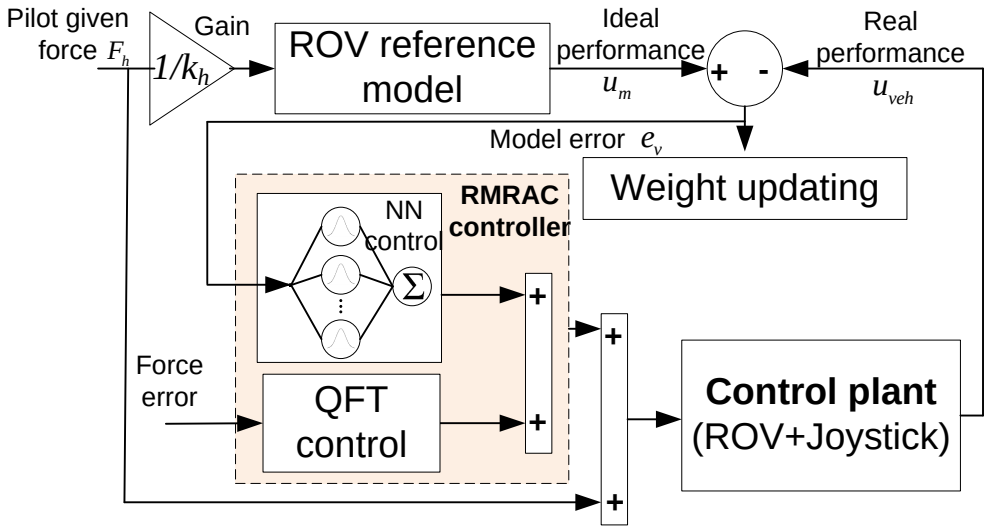

Fig. 5.5. RMRAC algorithm structure

5.3.2 QFT control design

The QFT synthesis strategy is to design the transfer function of the controller G and the pre-filter F which stabilises the closed-loop control system, shown in **Fig. 5.6**, with the presence of the uncertain parameters in the control plant P, the input and output disturbances.

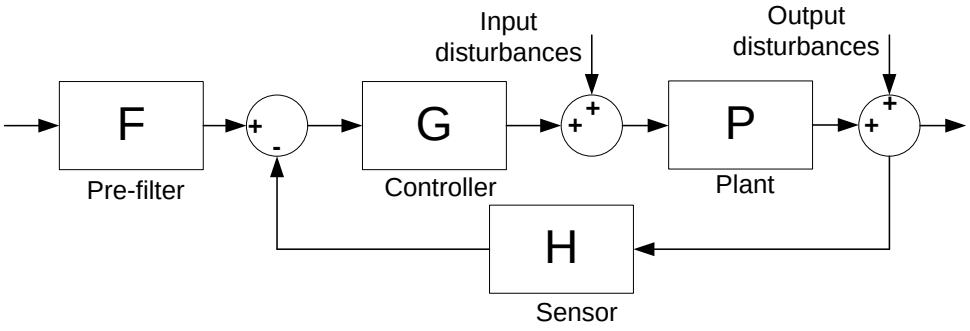

Fig. 5.6. Typical single-loop feedback system

5.3.2.1 Identification of family transfer function of the control plant

The first step of the QFT controller design process is to derive a family transfer function of the control plant which represents the uncertainties of the system. The control plant is presented in **Fig. 5.7**, consisting of the main components: 3-DOF Falcon haptic joystick, the AMC-ROV-V (the specifications are given in **Table 5.1**) and time delay due to data transmission.

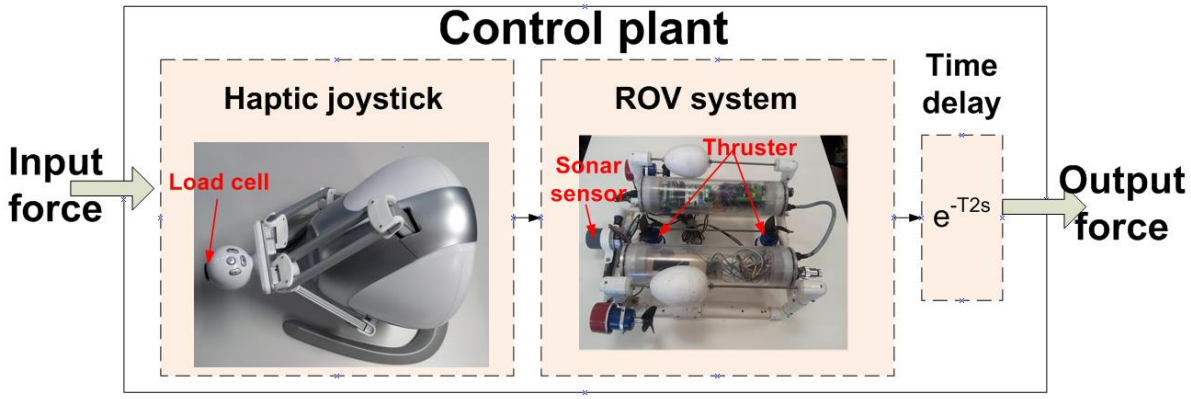

Fig. 5.7. Control plant and the components

Table 5.1: Specifications of the haptic hardware

Maximum haptic force	5N
Load cell range	0-50N
ROV maximum speed	0.5m/s
Sonar sensor range	0.5-5m
Sonar sensor resolution	0.02m

To examine the effect of time delay on the stability of the control system, the time delay was separately identified. The ROV communicates with the control station over the umbilical cable by using RS-485 protocol at a baud rate of 115200 bps. The time delay of the communication process was estimated by a loopback strategy: the periodic signal was sent from the control station to the ROV control system, where the on-board micro-controller received the signal then sent it back to the control station. The difference of phase between the transmitted and received signal was used to determine the time delay caused by data transmission. The estimation result shown in **Fig. 5.8** indicated that the time delay varied randomly, ranging from 0 to 0.01s.

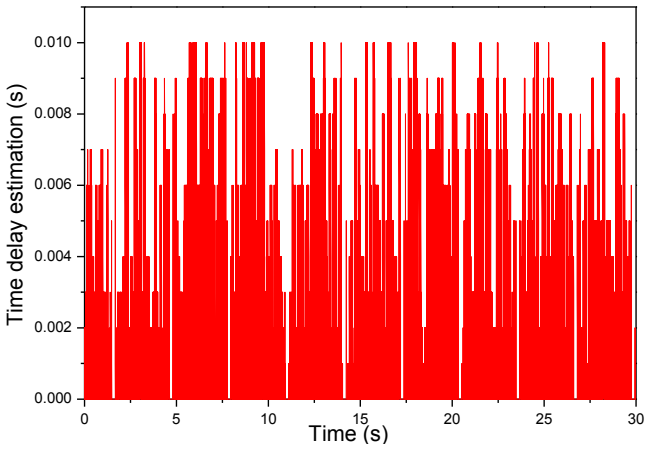

Fig. 5.8. Time delay estimation result

As the mathematical model of the AMC-ROV-V was fully determined in previous research (Le et al., 2014), the numerical-based ROV was utilised to simplify the identification process. The Falcon haptic joystick controlled the simulated ROV to surge back and forth, while the input force given by the ROV pilots were measured by the load cell, and the output force, including the inertia and drag force, were also collected, presented in **Fig. 5.9**, to identify the family transfer function of the control plant.

Once the data were collected, the main transfer function of the plant was derived employing the system identification toolbox of MATLAB, presented as

$$G_{plant}(s) = \frac{6.97s + 0.82}{s^3 + 1.63s^2 + 1.12s + 0.49} \tag{5.7}$$

with 82.32% data fitness.

The validation of the identification results is then illustrated in **Fig. 5.9b**, where it is seen that the output of the actual system and the model (5.9), drawn in turn by black and red lines, are relatively well fitted.

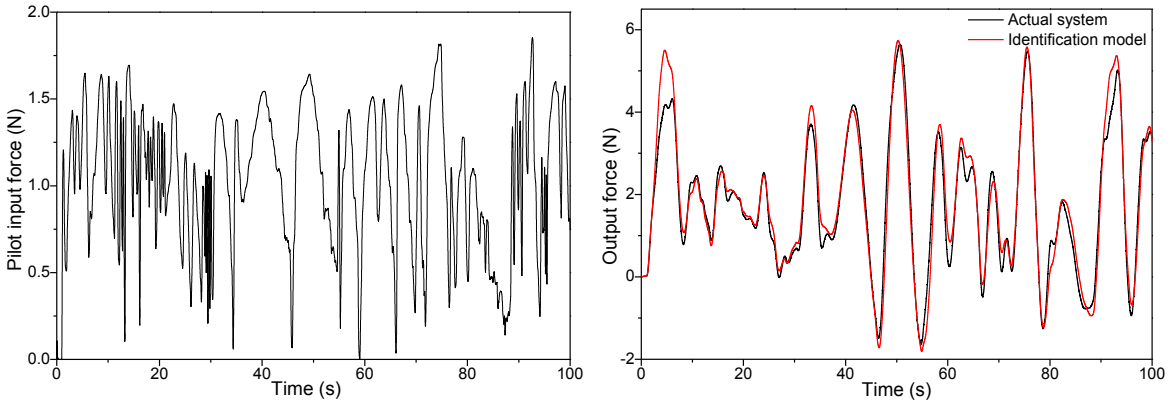

a. Pilot input force b. Output force

Fig. 5.9. Input, output signals and identification results

From the estimation results of time delay and the transfer function, the uncertain control plant can be described by the third-order family transfer function written as follows

$$P(s) = \frac{as+b}{s^3+cs^2+ds+e}e^{-Ts} \tag{5.8}$$

where $a \in [6.7, 7.1]; b \in [0.6,1]; c \in [1.4,1.8]; d \in [0.9,1.4]; e \in [0.3,.7] \text{and} T \in [0, 0.01]$ are the uncertain parameters of the control plant.

5.3.2.2 QFT control synthesis

Once the control plant P is established, the following steps are carried out to determine the robust controller G and the pre-filter F.

Step 1: Define the specification of the closed-loop control system

The QFT controller is designed to make the closed-loop control system achieve the stability and good performance that are described by the following criteria:

- **Stability specifications:** According to the Nyquist stability criterion, the closed-loop control system is only stable as long as its Nichols plot does not cross the critical points (180^o, 0 dB) in the Nichols chart (see **Fig. 5.10**) (Horowitz, 1993). To ensure this criterion, the gain margin M=1.4 equivalent to 3 dB represented by the red curve in **Fig. 5.10** is set to create a boundary around the critical point; and the following condition has to be satisfied to prevent the Nichols plot of the closed-loop system from intersecting the boundary:

$$\left|\frac{L(j\omega)}{1+L(j\omega)}\right| \le M = 1.4 \text{ with } \omega \ge 0 \tag{5.9}$$

where L is the open-loop transfer function $L(s) = P(s)G(s)$.

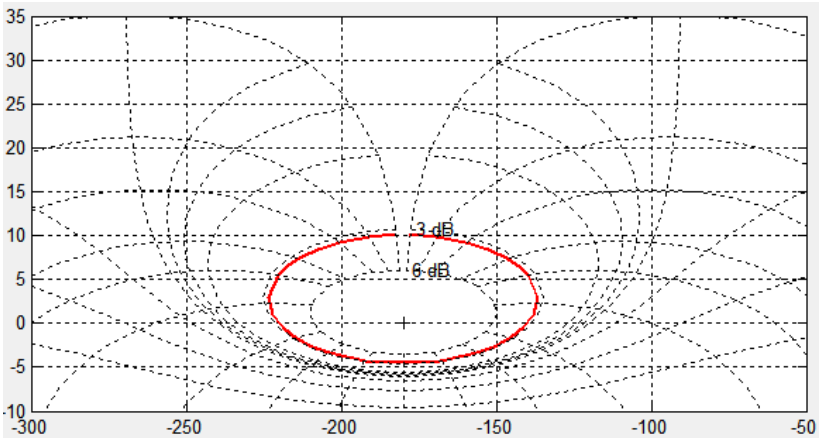

Fig. 5.10. Stability condition performed in Nichols chart

- **Reference tracking:** the performance of the control system is usually quantified based on the settling time and the percentage of overshoot for the unit step response; hence, the following criteria are selected for the closed-loop control system.
  - Settling time less than 1.5 s; and
  - Maximum percentage of overshoot smaller than 10%.

From the criteria, the upper and lower boundaries, presented in transform function form T_u and T_l are designed so that the step response of closed-loop transfer function $T(s)=\dfrac{F(s)P(s)G(s)}{1+P(s)G(s)}$ is always located within the boundaries, satisfying the condition $\left|T_l(j\omega)\right| \le \left|T(j\omega)\right| \le \left|T_u(j\omega)\right|$ for every value of ω in the interest frequencies.

Using a process of trial and error, the upper and lower boundaries are designed as

$$T_u(s)=\frac{8s+10}{s^2+6.4s+10} \tag{10}$$

$$T_l(s)=\frac{25}{s^2+14.08s+25}$$

whose step responses are shown in **Fig. 5.11**.

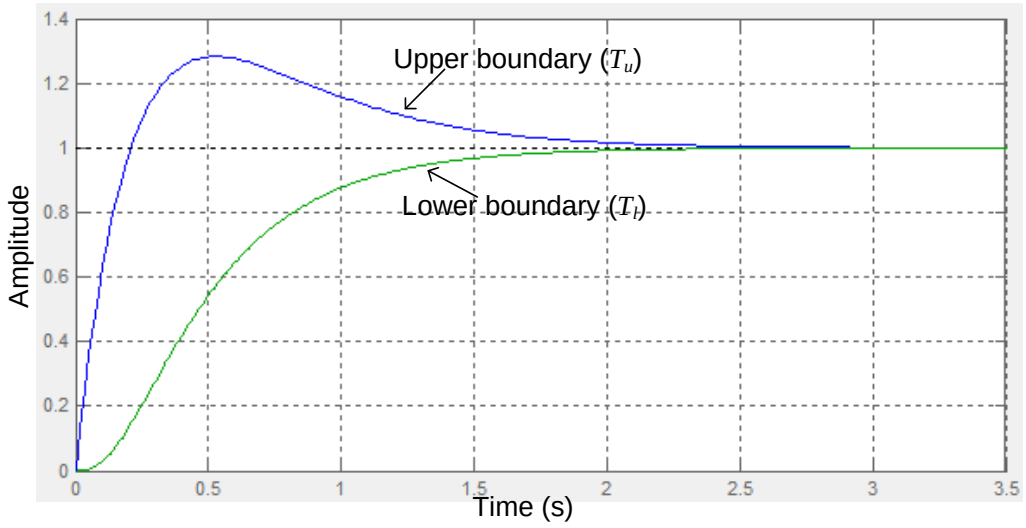

Fig. 5.11. Step response of the upper and lower boundary transfer functions

- **External disturbance rejection:** it is seen in **Fig. 5.4** that the input and output signals of the control plant are affected by the pilot-given force and the virtual force from obstacles. These forces are uncertain and independent from the characteristics of the control plant; thus, from the perspective of the control theory, they can be considered as external disturbances which cause a potential threat to the stability of the closed-loop system. To address these issues, the following conditions should be set

for the QFT controller design procedure to mitigate the effect of the external disturbance on the system (Borghesani, Chait, & Yaniv, 2003):

$\left|\frac{F(j\omega)}{1+PG(j\omega)}\right| \leq 1.2$ for rejection of disturbance at the plant output; and

$\left|\frac{FP(j\omega)}{1+PG(j\omega)}\right| \leq 0.2$ for rejection of plant input disturbances.

Step 2: Robust control design

The control constraints established in Step 1 are employed to synthesise the robust control at the critical frequency set $\omega = \{0.01, 0.1, 0.5, 1, 2, 5, 10, 20\}$ rad/s which is also the range of frequency of the haptic feedback signal. The transfer function of the QFT controller has to fulfil the worst case of all bounds by making the corresponding value of the loop gain on or above the boundary of each critical frequency (Horowitz, 1993).

Using the QFT control toolbox and trial and error strategy, the transfer function of the robust controller G is derived as

$$G(s) = \frac{112.6s^2 + 957s + 1126}{s^2 + 350s} \tag{5.11}$$

whose Nichols plot presented in **Fig. 5.12** does not cross the critical point, satisfying the stability criterion given in condition (5.9).

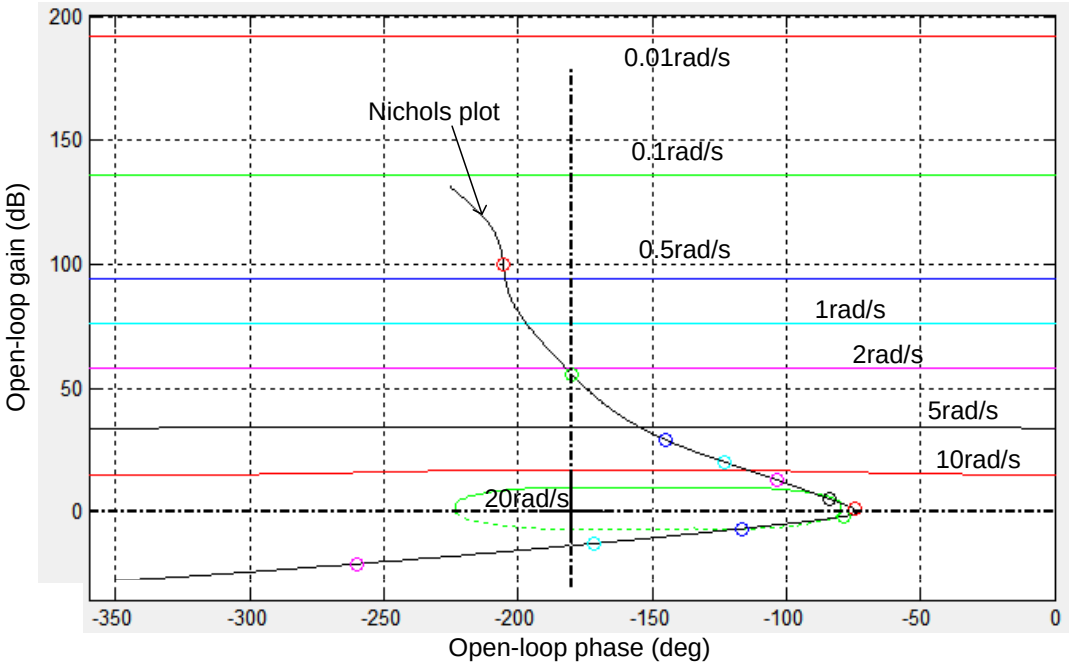

Fig. 5.12. Nichols charts of the control design results

Step 3: Pre-filter design

The pre-filter is designed to ensure that the closed-loop response of the control plant (5.8) lies within the upper and lower reference tracking boundaries defined in (10). Using the QFT control toolbox, the transfer function of the pre-filter F is derived as

$$F(s) = \frac{s^2 + 97.8s + 16.6}{s^2 + 7.6s + 14.4} \tag{5.12}$$

Figs. 5.13 and **14** show the results of the QFT controller design process. The frequency-domain plot, known as a Bode plot, and the step response plot in **Fig. 5.13** indicate that the controller G and the pre-filter F effectively guaranteed the stability and the reference tracking criterion. Additionally, the Bode magnitude plots in **Fig. 5.14,** denoting the effects of the input and output disturbance, were located below the zero threshold within the critical frequency range, i.e. the designed QFT controller attenuated the effect of external disturbances on the closed-loop control system.

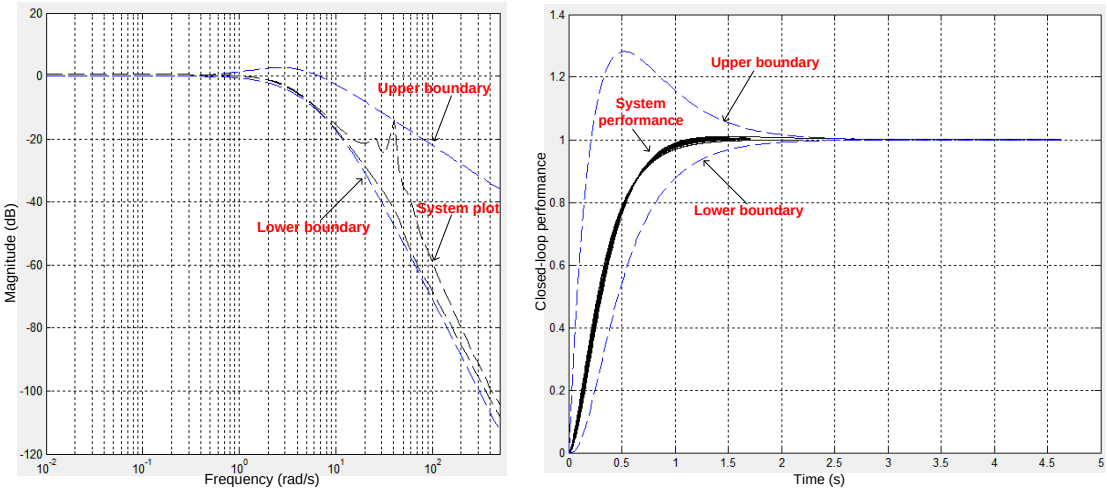

a. Bode diagram b. Step response

Fig. 5.13. Tracking performance with pre-filter

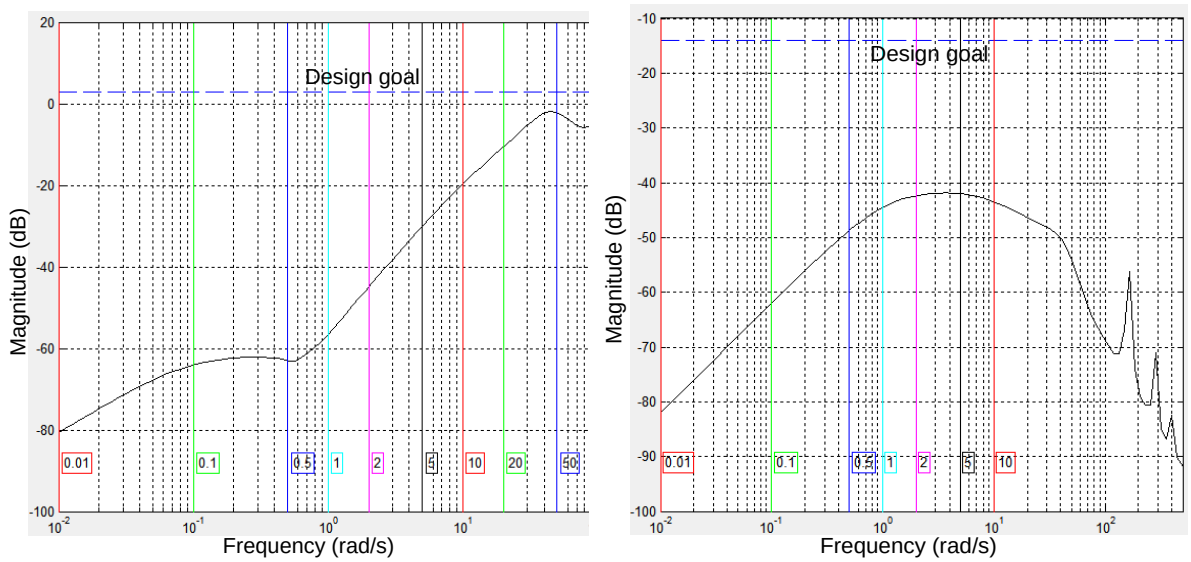

a. Output disturbance rejection b. Input disturbance rejection

Fig. 5.14. External disturbance rejection performance

5.3.3 MRAC controller design

The MRAC controller improves the transparency of the haptic control system by minimising the error between the ROV reference model and the control plant, thus mitigating the parasite force presented by the dynamics of the joystick, such as inertia, Coulomb friction, etc. The mathematical model of the reference model is selected as:

$$m\dot{u}_m + cu_m|u_m| + f_{vir} = F_h / k_h \tag{5.13}$$

where u_m is the surge speed of the ROV reference model where the input signal is the force given by ROV pilots F_h. The MRAC controller enables pilots to feel the forces being imposed on the ROV as if they are directly interacting with the vehicle as the error representing the difference between the actual system and the virtual model given in equation (5.13) converges to zero.

Due to the high adaptation rate, the neural network structure is used as the core of the MRAC controller and the control parameters are adjusted based on the back propagation algorithm. The structure of the neural network-based MRAC controller is presented in **Fig. 5.15**, consisting of hidden (n nodes) and output (1 node) layers. The following steps are carried out to calculate the control signals and update the control parameters.

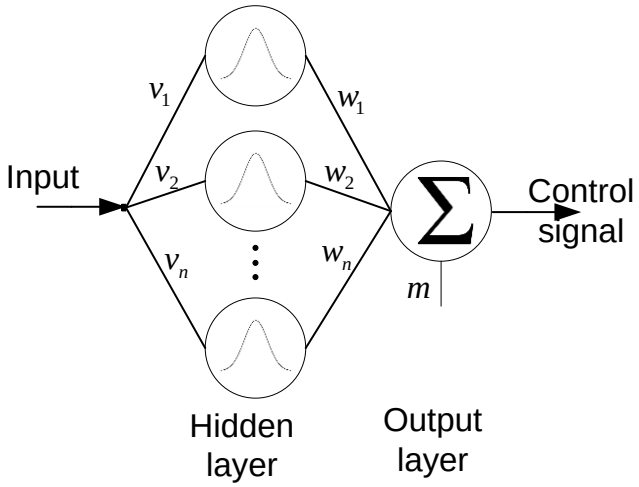

Fig. 5.15. Neural network-based MRAC control structure

Step 1: Initiate the random weights and biases of the neural networks system in the hidden layer (v_i and n_i) and output layer (w_i and m)

Step 2: Calculate the output control signal

The error between the actual system and the ROV reference model is defined as

$$e_v = u_m - u_{veh} \tag{5.14}$$

where u_m and u_{veh} are the surge speed of the ROV reference model and real system, respectively.

The output of the i^{th} node in the hidden layer is calculated as

$$z_i = f\left(net_i\right) = f\left(e_v v_i + n_i\right) \tag{5.15}$$

where *f(x)* is the activation function selected as

$$f\left(x\right) = \frac{2}{1+e^{-2x}} - 1 \tag{5.16}$$

The output values of the hidden layer are used to calculate the output signal in the output layer as follows:

$$out = \sum_{i=1}^{n} z_i w_i + m \tag{5.17}$$

Step 3: Update the weights and biases values

The weights and the biases of the neural network nodes are updated to minimise the following cost function:

$$E = \frac{1}{2} e_v^{\,2} \tag{5.18}$$

Applying the back propagation algorithms, the weights and bias in the output layer at time *t+1* are self-adjusted as

$$\begin{aligned} w_i(t+1) &= w_i(t) - \eta \frac{\partial E}{\partial w_i} \\ m(t+1) &= m(t) - \eta \frac{\partial E}{\partial m} \end{aligned} \tag{5.19}$$

where η is the learning rate (LR).

The updating parts in (5.19) are expanded using the chain rule as follows:

$$\begin{aligned} \frac{\partial E}{\partial w_i} &= \frac{\partial E}{\partial out}\frac{\partial out}{\partial w_i} = -\frac{u_{veh}}{\partial out}(z_i) \approx -\frac{u_{veh}(t) - u_{veh}(t-1)}{out(t) - out(t-1)}(z_i) \\ \frac{\partial E}{\partial m} &= \frac{\partial E}{\partial out}\frac{\partial out}{\partial m} \approx -\frac{u_{veh}(t) - u_{veh}(t-1)}{out(t) - out(t-1)} \end{aligned} \tag{5.20}$$

Substituting (5.20) into (5.19), the updating formulae of the weights and biases in the output layer are presented as

$$\begin{aligned} w_i(t+1) &= w_i(t) + \eta \frac{u_{veh}(t) - u_{veh}(t-1)}{out(t) - out(t-1)} z_i(t) \\ m(t+1) &= m(t) + \eta \frac{u_{veh}(t) - u_{veh}(t-1)}{out(t) - out(t-1)} \end{aligned} \tag{5.21}$$

Similarly, the weights and the biases in the hidden layer are calculated as

$$\begin{aligned} v_i(t+1) &= v_i(t) - \eta \frac{\partial E}{\partial v_i} \\ n_i(t+1) &= n_i(t) - \eta \frac{\partial E}{\partial n_i} \end{aligned} \tag{5.22}$$

with

$$\begin{aligned} \frac{\partial E}{\partial v_i} &= \frac{\partial E}{\partial out}\frac{\partial out}{\partial z_i}\frac{\partial z_i}{\partial v_i} \approx -\frac{u_{veh}(t) - u_{veh}(t-1)}{out(t) - out(t-1)}(w_i) g(.) \\ \frac{\partial E}{\partial n_i} &= \frac{\partial E}{\partial out}\frac{\partial out}{\partial z_i}\frac{\partial z_i}{\partial n_i} \approx -\frac{u_{veh}(t) - u_{veh}(t-1)}{out(t) - out(t-1)}(w_i) k(.) \end{aligned} . \tag{5.23}$$

The partial derivative functions of the function $z_i = f(net_i)$ are derived as

$$g(.)=\frac{\partial z_i}{\partial v_i}=\frac{e_v}{2}\left(1-f^2\left(net_i\right)\right)$$
$$k(.)=\frac{\partial z_i}{\partial n_i}=\frac{1}{2}\left(1-f^2\left(net_i\right)\right) \tag{5.24}$$

Substituting the expressions (5.23) and (5.24) into the formula (5.22), the updating formulae of the weights and biases in the hidden layer are presented as

$$v_i(t+1)=v_i(t)+\frac{\eta}{2}\frac{u_{veh}(t)-u_{veh}(t-1)}{out(t)-out(t-1)}w_i(t)e_v(t)\left(1-f^2\left(net_i(t)\right)\right)$$
$$n_i(t+1)=n_i(t)+\frac{\eta}{2}\frac{u_{veh}(t)-u_{veh}(t-1)}{out(t)-out(t-1)}w_i(t)\left(1-f^2\left(net_i(t)\right)\right) \tag{5.25}$$

Once the control parameters of the MRAC controller are updated, Step 2 is repeated.

5.4 Results and discussions

5.4.1 Simulation results

The simulation was conducted within a virtual reality simulation by coupling a Falcon haptic joystick controller to the simulation of the AMC-ROV-V whose mathematical models were described in (Le et al., 2014). The simulation programs were implemented in real time using the CHAI3D cross-platform at the sampling time of 0.001s. First, the stability and the performance of the RMRAC algorithm were evaluated by applying a constant force of 2N on the joystick to manoeuvre the ROV to surge forward. Three controllers, including PID, the QFT algorithm given in transfer function (5.10) without the adaptive part, and the proposed RMRAC algorithm containing five nodes in the hidden layer with the learning rate of 0.0005, were applied to control the surge motion of the simulated ROV. Three different time-delay operating modes, i.e. 0, 0.004s and 0.01s time delay, were also applied in turn to validate the robustness of the control algorithms.

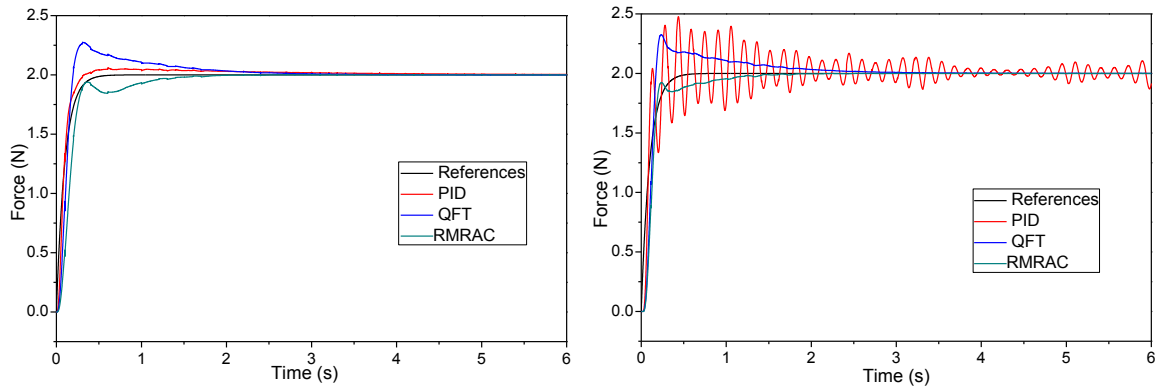

a. Zero time delay

b. 0.004s time delay

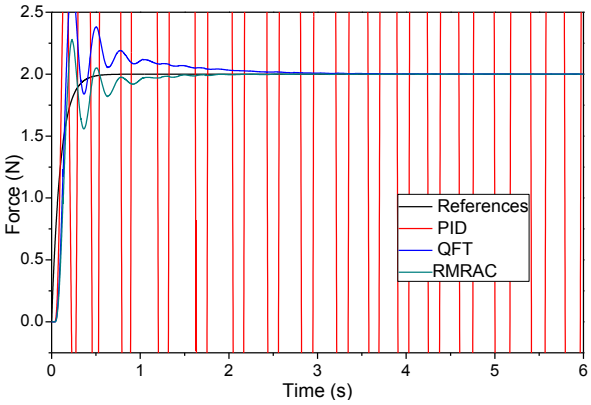

c. 0.01s time delay

Fig. 5.16. Control performance under various time delays

The results of the control algorithms with the step reference signal are shown in **Fig. 5.16**. In the zero time delay case, it is seen in **Fig. 5.16a** that all the controllers offered good performance with no steady-state error and a short settling time. The PID controller performance in the red line seems to be outstanding compared to the QFT and RMRAC algorithms as the overshoot is rather small, at 2%. Nevertheless, the robustness of the RMRAC algorithm is clearly shown in **Fig. 5.16b** and **Fig. 5.16c** as the time delay was applied to the closed-loop control system. In the 0.004s time delay case, whilst the PID performance started to oscillate, QFT and RMRAC, represented by the blue and green lines in **Fig. 5.16b**, provided almost the same control quality as in the zero time delay simulation. As the time delay was set to the maximum value, 0.01s, the PID controller failed to regulate the stability of the system, creating the large amplitude of oscillation around the reference values; however, the RMRAC performance still converged to the reference values despite the minor oscillations that occurred in the transient period. Additionally, due to the adaptive part, the tracking performance of the RMRAC controller performs with less overshoot and has a shorter settling time compared to the QFT controller, especially in the case where the time delay is large (see **Fig. 5.16c**).

To examine the influence of the learning rate, the simulations using the RMRAC controller were performed in a 0.01s time delay with the learning rate ranging from 0 to 0.001. **Fig. 5.17** shows the comparison of the error between the ROV reference model and the simulated ROV for varying learning rates. In the non-adaptive case where the learning rate is zero, there is a steady error around 0.18, while the adaptive part of the controller leads the error to converge to zero regardless of the value of the learning rate, meaning that the parasite effects were eliminated from the haptic control system due to the adaptive controller. However, the learning rate should be balanced between low and high values as the low learning rate provides a slow convergence while the high value causes oscillation around zero that can affect the stability of the system. It is seen from **Fig. 5.17** that the performance with the medium learning rate of 0.0005, represented by the blue line, is better than the

other cases due to the fast convergence and the lesser oscillation; hence this value was used for the subsequent simulations and experiments.

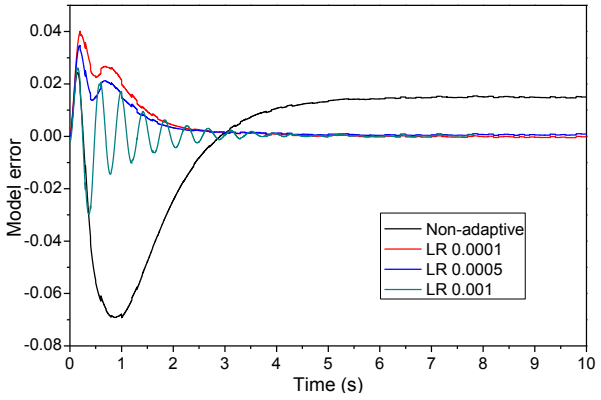

Fig. 5.17. Model reference error with different learning rate

Next, the ROV haptic drive with the RMRAC controller was validated by manoeuvring the ROV in an environment containing obstacles. The ROV with a sonar sensor was initially located in a position 10m from the obstacle and the boundary of the virtual force presented by the obstacles was set to 5m as shown in **Fig. 5.18**. A ROV pilot applied a pushing force of 2N to the joystick lever, controlling the vehicle as it moved forward and approached the obstacle.

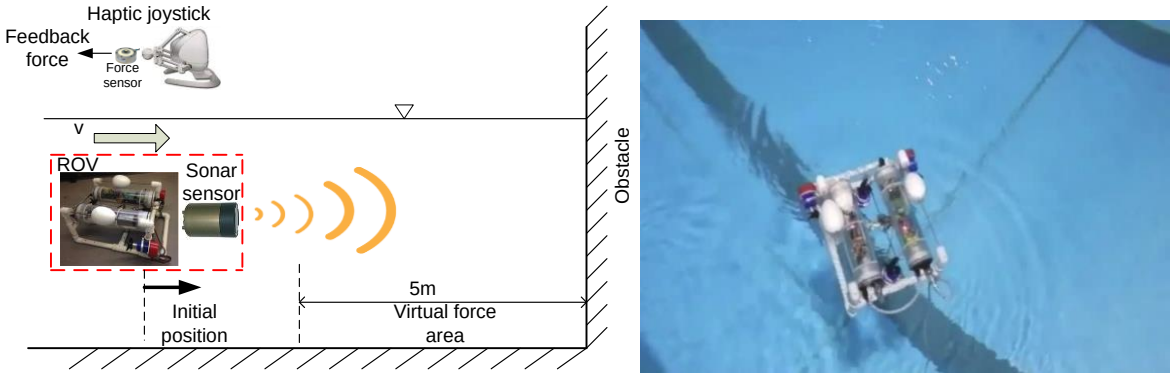

a. Testing context b. AMC-ROV-V in survival centre

Fig. 5.18. Simulation and experimental set-up

Between the 0 and 9 seconds, the ROV accelerated from 0m/s to around 0.5m/s and remained at that speed (see **Fig. 5.19b**). As the obstacle was not detected in this period, the motion of the vehicle was resisted purely by the drag force from the surrounding fluid. As the obstacle was detected in the 9th second, the virtual force started to impose on the ROV, pushing the haptic lever back and resulting in the deceleration of the ROV for between 9 and 15 seconds. The virtual force kept increasing as the ROV moved closer to the obstacles until it balanced with the input force given by the pilots, when the ROV stopped, meaning that the virtual force presented by the obstacle was large enough to keep the

ROV 3m away from the potential collision source (see **Fig. 5.19c**); hence the pilot had to provide more force on the joystick to manoeuvre the ROV in close proximity to the obstacles.

To examine the robustness of the system to unexpected change, the pilot suddenly released the haptic joystick lever in the 30th second. It is seen from **Fig. 5.19a** that the force dropped immediately from 2N to 0N without a large overshoot and fluctuation, proving that the stability of the system was maintained. As the joystick lever was pushed back due to the virtual force presented by the obstacle, the ROV surged backward from the obstacles at the speed of 0.4m/s and stopped at around the marginal boundary of the safety zone (5m away from the obstacle) when the external forces were balanced (see **Fig. 5.19c**). The error between the haptic force representing the interaction between the ROV pilot and the joystick and the feedback force representing the external force being imposed on the vehicle was relatively small, just around 0.3N (see **Fig. 5.19a**), indicating that the haptic controller has the ability to replicate the external information including hazard from obstacles and hydrodynamic interaction via the haptic feedback force to the ROV pilots.

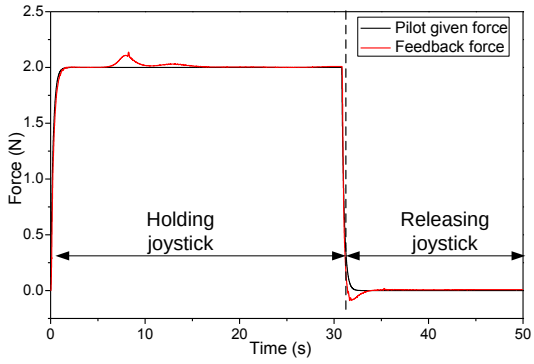

a. Force performance

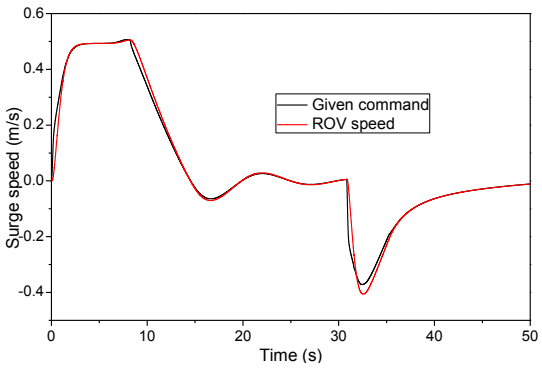

b. Surge speed performance

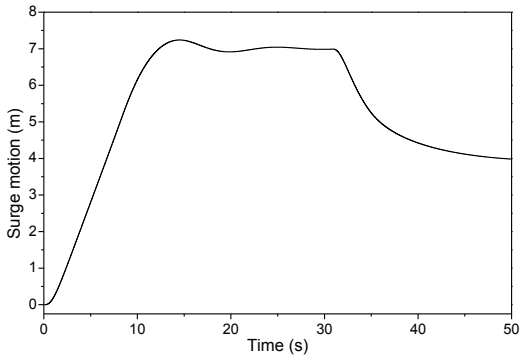

c. Surge distance

Fig. 5.19. ROV haptic drive system performance

5.4.2 Experimental results

The experiments were conducted employing the physical ROV in the survival centre of the Australian Maritime College. The experimental context was similar to that of the previous simulation with the exception that the swimming pool borders were used as the obstacles (see **Fig. 5.18**). The ROV pilot was tasked to use the haptic joystick to manoeuvre the ROV forward while maintaining a constant speed of 0.35m/s. Besides, to protect the joystick from excessive force, the maximum haptic force is limited to the value of 4.5N.

It is difficult to directly quantify the resistance created by the inertia of the ROV and the fluid interaction. It is seen from equation (5.1) that the thrust forces of the ROV thruster are equal to the total resistance forces imposed on the ROV hull. The thrust force of the propeller was indirectly determined using the estimation algorithm in (Le et al., 2014) and estimation results were combined with the virtual forces calculated from the formula (5.2) and the reading of the sonar sensor whose specification is given in **Table 5.1** for the haptic feedback information.

Fig. 5.20a showed the haptic force performance which represented the external effects on the ROV. At the beginning from 0 to 3 seconds, as the ROV accelerated from 0 to the desired speed of 0.35m/s, the ROV thrusters provided more power, resulting in the peak of the haptic force in this period. After achieving the steady speed, the ROV was mainly subjected to the drag force from the surrounding fluid, resulting in a roughly constant haptic feedback force at 0.8N between 3 and 16 seconds. The haptic force started increasing as the ROV moved in proximity to the obstacle, requiring more effort from the ROV pilot to maintain the speed of the ROV in the area: the haptic force rose from 0.8N to around 4.5N between 16 and 26 seconds. As the ROV was within 1.6m of the obstacle, the haptic force was saturated and the speed dropped to zero to avoid the collision hazard, as shown in **Fig. 5.20b** and **Fig. 5.20c**.

The experimental results on the actual ROV indicate that the proposed control algorithm is stable in the presence of time-varying delay and noise from the sonar sensor. Additionally, the errors of the force tracking results were found to be around 0.2N, which is relatively small, indicating that the RMRAC is effective to be applied in the ROV haptic control system.

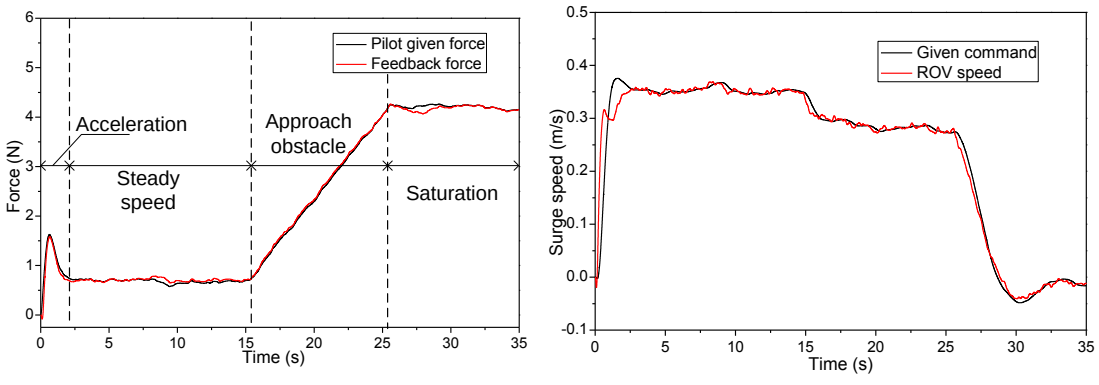

a. Force performance b. Surge speed performance

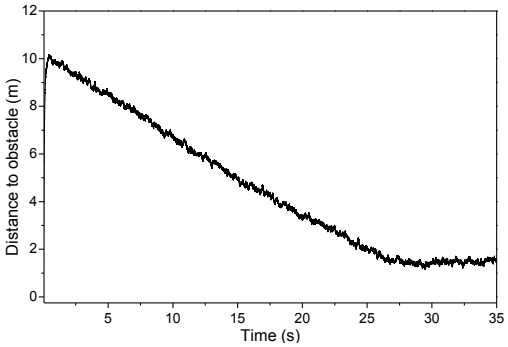

c. Surge distance

Fig. 5.20. ROV haptic drive system performance

5.5 Conclusion

This paper presented the development of the novel haptic controller named RMRAC for a ROV haptic drive system to maintain the stability and improve the system performance. By including a coupled QFT-MRAC algorithm, the proposed RMRAC algorithm has the ability not only to stabilise the system in the presence of uncertain parameters, perturbations and varying time delay but also to eliminate the parasitic force presented by the joystick dynamic model, making the haptic feedback more transparent. The effectiveness of the proposed technique has been verified by conducting both simulations and experiments of controlling the surge motion of the actual ROV by a haptic joystick. The results indicated that the coupled QFT-MRAC algorithm is sufficiently effective and robust to be applied to manoeuvre the ROV, as the error of the tracking force control performance is relatively small and the system is capable of maintaining stability even under sudden changes of the input force. Besides, the haptic feedback containing information on the inertia, hydrodynamic force and hazard of obstacles in the vicinity of the ROV provides the ROV pilot with the feeling of directly interacting with the vehicle, which improves the safety of the ROV when manoeuvring in cluttered environments.

Future work is planned to upgrade the haptic drive system to at least 3 DOFs by incorporating more sonar sensors to fully achieve safety for the ROV in a complex operating environment.

Chapter 6 Summary, conclusions and future work

This chapter provides an overall summary of the thesis, bringing together the findings of the individual chapters. It also concludes on the finding and outcomes, highlighting the implications of the findings, the limitations, significance, applicability, and the recommendations for further research.

6.1 Project summary

The focus of this project was on the application of haptic technology to control an underwater ROV in order to assist its pilots to safely manoeuvre the vehicle in hazardous environment. The main research objective was defined as, "how to apply a haptic drive system in controlling an observation class ROV?".

The project included a review of the literature relevant to ROV control systems and the application of haptic technology in providing the tactile feedback. While haptic technology is applied successfully to many operations such as tele-operation control systems of mobile robots, simulation training, and robotic manipulators; its application to underwater vehicles is minimal and is thus lacking rigorous research, design and application information in the public domain. ROV pilots are not always able to observe and identify external hazards by purely relying on visual feedback, especially when ROVs operate in environments littered with obstacles. This in extreme cases can result in collision and mission failure. Hence, a ROV drive system including both visual and tactile feedback to assist the ROV pilot to safely manoeuvre the vehicles within hazardous environments.

In addressing the main research question, the study applies the haptic technology to the ROV control systems and validates the effectiveness of the application using both numerical and experimental approaches. The ROV haptic drive system developed in this project was initially examined within a simulated environment and then applied to control a low-cost open source hardware-based ROV. The research steps consists of

- development of ROV hardware, algorithms for sensor signal processing, and ROV motion controllers (Chapters 2 and 3);
- application of the Artificial Potential Field (APF) to transmit the information on stationary and moving obstacles around the ROV to its pilot via tactile feedback (Chapter 4); and
- development of a robust adaptive control algorithm for the haptic controller to mitigate the adverse effects of time delay of the tele-communication and the inherent parasite forces due to the dynamics of the haptic joystick (Chapter 5).

6.2 Conclusions

The findings and discussion presented in the thesis lead to the following main conclusions, which are given below under the relevant areas:

6.2.1 Performance of ROV haptic drive system

- **Haptic feedback information**: The haptic feedback force emitted from the joystick represents the drag force from the surrounding fluid, the inertia of the ROV, and the potential threat from surrounding obstacles. This enables ROV pilots to 'feel' as if they are part of the

ROV and are directly interacting with the working environment. For instance, they are able to sense the effective inertia including that of the vehicle as well as the added mass component as the ROV accelerates. The same applies to the drag force due to fluid-vehicle interaction which affects the vehicles behaviour as well as a projecting a repulsive force as the ROV approaches nearby obstacles. By providing more information to pilots, the haptic drive system assists them to safely control the vehicle within cluttered and hazardous environments. However, on the flip side, the haptic drive system was found to increase the workload of ROV pilots as they have to exert more effort against the haptic force generated by the joystick, especially in cases where the pilots manoeuvre ROVs in a close proximity to obstacles for tasks such as inspections and maintenance (Chapter 4 Part B). This means that the haptic drive system does not always provide comfortable sensation to ROV pilots, suggesting that the haptic feedback gains should be adjusted according to specific tasks and working environments, for example the high gains could be set for manoeuvring task in spacious environments, and smaller gains are selected as the ROV approaches objectives.

- **Obstacle detection via haptic feedback**: The information of the relative distances and velocities between the ROV and surrounding obstacles play a crucial role in accurately generating a repulsive haptic feedback force to assist ROV pilot to avoid the obstacles. The novel APF algorithm developed within this project based on Fuzzy C-Means (FCM) and Kalman Filter (KF) algorithms has successfully modelled the potential risk presented by both stationary and moving obstacles using raw data obtained from an on-board 2-D scanning sensor. Although the performance of the coupled FCM-KF algorithm depends on the size and distance of the obstacles to the ROV, the accuracy of the algorithm is well within acceptable tolerances for most ROV operations. The accuracy of the coupled algorithm is also influenced by the resolution of the scanning sensor, thus a higher resolution sensor would improve the accuracy of the estimations and thus the calculated results. The simulation programs presented in Chapter 4 Part B, simulated the ROV haptic drive system that employed the laser-based scanning sensor with high resolution to provide high quality raw data for the APF calculation.

  The final risk avoidance vector calculated from the APF algorithm provides ROV pilots with an indication of the danger level of obstacles in the vicinity of the ROV and prompts, through the haptic joystick, the direction to be steered in order to avoid collision. Although the experimental ROV described in Chapter 5 only uses a single beam sonar sensor that is relatively low in resolution in comparison to the laser-based scanning sensor, the reading from the sensor offered adequate information on the obstacles' states to assist the pilot using haptic feedback forces generated within the joystick control to avoid the surrounding obstacles (Chapter 5). However, due to the high resolution and the full-circle scanning

capability the laser-based scanning sensor is recommended for the application to ensure the quality of the haptic feedback information, especially in complex environments containing various obstacles.

- **Robust haptic control algorithm**: The external disturbances and time delays of the communication process were found to cause adverse effects on the performance of the ROV haptic drive system in term of transparency and the stability of tele-operation control systems, resulting in ROV manipulation errors, which in extreme cases could lead to obstacle collision and mission failure. By including a coupled QFT-MRAC algorithm, the RMRAC algorithm has the ability not only to stabilise the system in the presence of uncertainty parameters, perturbations, and varying time delays but also to eliminate the parasitic forces caused by the joystick dynamic model, thus increasing the quality of the haptic feedback information. The simulation results discussed in Chapter 5 show the superior performance of the RMRAC algorithm over the PID and QFT controller as the force response generated by RMRAC algorithm provides smaller settling time and less fluctuation within the transient period, thus highlighting the effectiveness of the proposed technique. The experimental work (Chapter 5) examined the performance of the ROV haptic drive system comparing it against that of the simulations. Although noise from the sensors and external disturbances affect the signals, the RMRAC algorithm offers a stable haptic force response that is compatible to the simulation results, providing confidence in the proposed technique, and thus implying the applicability of this control algorithm to the ROV haptic drive system.

- **Using the haptic drive system to control a virtual reality ROV**: The simulation programs, where the control algorithms and haptic drive system were tested prior to applying them to the physical ROV, consisted of the mathematical model of the ROV developed in Chapter 3 and the Virtual Reality (VR) interface built within a Simulink toolbox. The quality of the simulation depends on the accuracy of the mathematical model of the ROVs and the computational resources of the host computer (including high-performing graphics cards for the required visual interface) to ensure accurate representation and adequate VR interface. To ensure the real time constraint within the simulation program, sampling times of 0.001s to 0.01s were deemed sufficient. The real time toolbox of Simulink was found to be sufficiently flexible and compatible to the haptic control library written in C++, thus allowing the haptic joystick to be incorporated into the simulation programs to control the simulated ROV.

6.2.2 Performance of low-cost observation class ROV

- **ROV modelling**: The mathematical model of the ROV including kinetics and kinematics were developed based on Fossen's theory, and used as the control objective in simulation and virtual reality programs where the control algorithms were tested before being applied to the physical ROV (Chapters 2, 3, and 4). The parameters of the ROV mathematical model consisting of damping coefficients and the added masses were determined using Computational Fluid Dynamics (CFD) methods. The simulation program was useful to tune and select the parameters for the haptic and motion controller of the ROV drive system as the performance of the simulated model was compatible with the physical ROV and its systems. The depth and haptic control experimental results described in Chapter 2 Part B and Chapter 5 showed good agreement with those of the simulation programs.

- **Control structure and ROV-control station communication**: The combination between the host-target control structure and the open source hardware proved sufficiently reliable and flexible to enable control and programing of the ROV in real time. This allowed the user to easily modify and upgrade control algorithms of the ROV at the station computer without having to re-program the microcontroller located within the ROV, which would require significantly longer time and effort. In addition, using the open source hardware also substantially reduces the ROV fabrication cost.

  The data transmission between the ROV and the control station caused a varying time delay of around 0.01s (Chapter 5), which can be neglected in the ROV motion controller such as depth and heading control as it is very small compared to the ROV's motion response time. However, the time delay adversely effected to the stability of the haptic drive system because of the high sensitivity of the force controllers incorporated within the haptic joystick (Chapter 5). Therefore, this phenomenon should be seriously taken into account when designing robust haptic controllers for ROVs.

- **Low-cost sensors performance and signal processing algorithm**: The low-cost motion sensors used in this project include: an inertial sensor, a digital compass, and a pressure sensor. The experimental results showed that the raw data from the inertial sensor and digital compass are susceptible to external noise and time-varying bias values (Chapter 3 Part A); requiring an advanced filter algorithm in order to eliminate the noise from sensor feedback signals before they are used to compute the control signals for the ROV. A two-layer Kalman filter was developed to estimate the ROV heading from the raw data of the inertial sensor and the digital compass. The experimental results showed that the effects of external accelerations and roll/pitch disturbances were effectively eliminated as the heading of ROV estimated by

the proposed algorithm were in good agreement with the results captured by the external camera system (Chapter 3 Part A). This proves that the two-layer Kalman filter is able to accurately process the raw data acquired by the low-cost sensory system to observe the states of the ROV.

- **ROV motion control algorithms**: Due to the highly nonlinear characteristics of the vehicle model and disturbances from the external environment, the linear control algorithms, (such as PD and PID with the constant control gains), are incapable of providing adequate manoeuvring performance of the ROV, resulting in large steady state errors and high fluctuation during the transient periods. Combining the PID controller with advanced algorithms, such as model-based control and self-tuning algorithms validated in Chapter 2 Part B and Chapter 3 Part B, provided significantly better performance. Although the hybrid PID and the model-based controller required the kinetics of the ROV with specific parameters, the self-tuning nonlinear PID was able to adjust the control parameters to minimise the control errors represented by the cost function without requiring the kinetic model. However, it is required to carefully select the learning rate value of the self-tuning process, as a low value slows down the convergent speed while a high value makes the system unstable and sensitive to the feedback signals. There is always the trade-off between the stability and the responsiveness of the ROV control system, hence a suitable control algorithm is required to balance these two criteria.

6.3 Applicability of the research findings

In this project, haptic technology was incorporated into the drive system of an ROV in an effort to improve the manoeuvring ability of the vehicle within hazardous environments involving obstacles and disturbances. The inherent issues of haptic control systems; including the effect of time delay, stability of system, and effective strategies to communicate surrounding environmental information to pilots via tactile feedback; were studied using both numerical and experimental approaches. The findings show that the haptic technology developed within this project has the ability to drive an observation-class ROV within environments littered with obstacles, as it provides the ROV pilot with information on both stationary and moving obstacles using APF strategy. The proposed RMRAC algorithm is able to address adverse effects such as time delays, sensor noise, and parasite forces of the haptic joystick, thus providing stable and transparent haptic feedback forces to the ROV pilot.

The results of the study offer a basis and support for the applicability of haptic technology for a safer and more reliable ROV drive system. The simulation results within the VR environments also show the possibility of adopting the haptic technology in ROV control training regimes, which provides

pilots greater understanding of the behaviour and response of their vehicles within various working environments.

The project also included development and enhancement of low-cost observation class ROV using open source hardware and the low-cost sensors. The study extends the applicability of the open source hardware by applying the host-target control structure which is able to overcome the limitation associated with the computational power of the microcontroller. This allows the programmers to develop complex algorithms and filters, such as two-layer Kalman filter and neural network-based adaptive PID control, to process the raw data from low-cost sensors and deal with the nonlinear characteristics of the vehicle, leading to effective strategies to control and monitor low-cost ROVs. The ROV control structure used in the project provides a reliable solution to develop a novel generation of low-cost ROVs using more accessible programming procedure and real time data acquisition, hence making such ROVs more accessible to researchers and enhancing the applicability of underwater vehicles in various purposes such as fish farm monitoring system and remote coastal supervision.

6.4 Future work

Based on the achievements of the study, direct extension of this work could lead to the following

- Extending the investigation into the interaction between human and haptic drive system, enabling the comparison between the haptic drive system and the conventional ROV drive systems, which purely rely on visual feedback. Several indices, such as accuracy of the ROV control, number of collision during manoeuvring, and physical/mental workload, could be employed to quantify the performance of ROV pilots using the haptic devices, allowing to optimise the haptic feedback gains of the system and to balance the trade-off between the haptic feedback intensity and workload.
- Investigating the application of the APF algorithm and scanning sensors to detect obstacles in a complete 3-D environment, thus providing greater protection for ROV using haptic technology. In addition, the adverse effects of scanning sensors such as noise, cross-talk, and diversity, could be investigated to design proper data processing algorithms.
- Further upgrading the haptic joystick system by adding more DOFs, enabling ROV pilots to use the haptic joystick to control work-class ROVs with incorporated robotics manipulators to accomplish complex tasks such as underwater welding.
- Extending the VR simulation by improving the accuracy of the numerical model of the ROV and the quality of the graphic interface, making the simulation more realistic for ROV pilot and mission training.

- Improving the electronics and communication system of the low-cost ROV, such as the replacement of the RS-485 protocol by TCP or UDP protocols in order to reduce the effects of time delays on the stability of the system.

The long term objective of the work is to develop a complete haptic drive system for ROVs, which fully assists pilots to make safe and appropriate decisions during ROV manoeuvring operations by providing full 3-D information about the operating environment. This would improve the performance and safety of systems and allow pilots to accomplish complicated missions in hazardous environments.

Bibliography

Abdossalami, A., & Sirouspour, S. (2009). Adaptive Control for Improved Transparency in Haptic Simulations. *Haptics, IEEE Transactions on, 2*(1), 2-14. doi: 10.1109/toh.2008.18

Alkhalidi, M., Neelamani, S., & Al Haj Assad, A. I. (2015). Wave forces and dynamic pressures on slotted vertical wave barriers with an impermeable wall in random wave fields. *Ocean Engineering, 109*, 1-6. doi: http://dx.doi.org/10.1016/j.oceaneng.2015.08.025

Anh, H. P. H. (2010). Online tuning gain scheduling MIMO neural PID control of the 2-axes pneumatic artificial muscle (PAM) robot arm. *Expert Systems with Applications, 37*(9), 6547-6560. doi: http://dx.doi.org/10.1016/j.eswa.2010.02.131

Antonelli, G., & Chiaverini, S. (2003). Fuzzy redundancy resolution and motion coordination for underwater vehicle-manipulator systems. *Fuzzy Systems, IEEE Transactions on, 11*(1), 109-120. doi: 10.1109/tfuzz.2002.806321

Azis, F. A., Aras, M. S. M., Rashid, M. Z. A., Othman, M. N., & Abdullah, S. S. (2012). Problem Identification for Underwater Remotely Operated Vehicle (ROV): A Case Study. *Procedia Engineering, 41*, 554-560. doi: http://dx.doi.org/10.1016/j.proeng.2012.07.211

Baser, O., Gurocak, H., & Konukseven, E. I. (2013). Hybrid control algorithm to improve both stable impedance range and transparency in haptic devices. *Mechatronics, 23*(1), 121-134. doi: http://dx.doi.org/10.1016/j.mechatronics.2012.11.006

Bessa, W. M., Dutra, M. S., & Kreuzer, E. (2008). Depth control of remotely operated underwater vehicles using an adaptive fuzzy sliding mode controller. *Robotics and Autonomous Systems, 56*(8), 670-677. doi: http://dx.doi.org/10.1016/j.robot.2007.11.004

Blain, M., Lemieux, S., & Houde, R. (2003, 22-26 Sept. 2003). *Implementation of a ROV navigation system using acoustic/Doppler sensors and Kalman filtering.* Paper presented at the OCEANS 2003. Proceedings.

Bo, Z., Blanke, M., & Skjetne, R. (2012, 27-29 June 2012). *Particle filter ROV navigation using hydroacoustic position and speed log measurements.* Paper presented at the American Control Conference (ACC), 2012.

Borghesani, C., Chait, Y., & Yaniv, O. (2003). *The QFT Frequency Domain Control Design Toolbox For Use with MATLAB*: Terasoft, Inc.

Brandt, A. M., & Colton, M. B. (2010, 10-13 Oct. 2010). *Haptic collision avoidance for a remotely operated quadrotor UAV in indoor environments.* Paper presented at the Systems Man and Cybernetics (SMC), 2010 IEEE International Conference on.

Brennen. (1982). A Review of Added Mass and Fluid Inertial Forces *A Review of Added Mass and Fluid Inertial Forces*: Department of the Navy , Port Hueneme, CA, USA.

Busquets, J., Busquets, J. V., Tudela, D., Perez, F., Busquets-Carbonell, J., Barbera, A., . . . Gilabert, J. (2012, 24-27 Sept. 2012). *Low-cost AUV based on Arduino open source microcontroller board for oceanographic research applications in a collaborative long term deployment missions and suitable for combining with an USV as autonomous automatic recharging platform.* Paper presented at the Autonomous Underwater Vehicles (AUV), 2012 IEEE/OES.

Carignan, C. R., & Cleary, R. K. (2000). Closed-loop force control for haptic simulation of virtual environments. *Haptics-e, 1*(2), 1-14.

Cetin, O., Zagli, I., & Yilmaz, G. (2013). Establishing Obstacle and Collision Free Communication Relay for UAVs with Artificial Potential Fields. *Journal of Intelligent & Robotic Systems, 69*(1-4), 361-372. doi: 10.1007/s10846-012-9761-y

Christ, R. D., & Wernli, R. L. (2013). *The ROV Manual: A User Guide for Remotely Operated Vehicles*: BUTTERWORTH HEINEMANN.

Conte, G., & Serrani, A. (1998). Robust control of a remotely operated underwater vehicle. *Automatica, 34*(2), 193-198. doi: http://dx.doi.org/10.1016/S0005-1098(97)00191-X

Corradini, M. L., & Orlando, G. (1997). A discrete adaptive variable-structure controller for MIMO systems, and its application to an underwater ROV. *Control Systems Technology, IEEE Transactions on, 5*(3), 349-359. doi: 10.1109/87.572131

Dongjun, L., Franchi, A., Hyoung Il, S., ChangSu, H., Bulthoff, H. H., & Giordano, P. R. (2013). Semiautonomous Haptic Teleoperation Control Architecture of Multiple Unmanned Aerial Vehicles. *Mechatronics, IEEE/ASME Transactions on, 18*(4), 1334-1345. doi: 10.1109/tmech.2013.2263963

Dukan, F., & Sørensen, A. J. (2014). Sea floor geometry approximation and altitude control of ROVs. *Control Engineering Practice, 29*, 135-146. doi: http://dx.doi.org/10.1016/j.conengprac.2014.04.006

Farkhatdinov, I., & Ryu, J.-H. (2010). Stability Analysis of Mobile Robot Teleoperation with Variable Force Feedback Gain. In A. L. Kappers, J. F. van Erp, W. Bergmann Tiest & F. T. van der Helm (Eds.), *Haptics: Generating and Perceiving Tangible Sensations* (Vol. 6191, pp. 177-182): Springer Berlin Heidelberg.

Feng, Z., & Allen, R. (2004). Reduced order H∞ control of an autonomous underwater vehicle. *Control Engineering Practice, 12*(12), 1511-1520. doi: http://dx.doi.org/10.1016/j.conengprac.2004.02.004

Fossen, T. I. (2011). *Handbook of Marine Craft Hydrodynamics and Motion Control*: John Wiley and Sons.

Fossen, T. I., & Blanke, M. (2000). Nonlinear output feedback control of underwater vehicle propellers using feedback form estimated axial flow velocity. *Oceanic Engineering, IEEE Journal of, 25*(2), 241-255. doi: 10.1109/48.838987

Fossen, T. I., & Perez, T. (2009). Kalman filtering for positioning and heading control of ships and offshore rigs. *Control Systems, IEEE, 29*(6), 32-46. doi: 10.1109/mcs.2009.934408

Ge, S. S., & Cui, Y. J. (2002). Dynamic Motion Planning for Mobile Robots Using Potential Field Method. *Autonomous Robots, 13*(3), 207-222. doi: 10.1023/a:1020564024509

Goheen, K. R., & Jefferys, E. R. (1990). Multivariable self-tuning autopilots for autonomous and remotely operated underwater vehicles. *Oceanic Engineering, IEEE Journal of, 15*(3), 144-151. doi: 10.1109/48.107142

Gosselin, F., Bouchigny, S., Mégard, C., Taha, F., Delcampe, P., & d'Hauthuille, C. (2013). Haptic systems for training sensorimotor skills: A use case in surgery. *Robotics and Autonomous Systems, 61*(4), 380-389. doi: http://dx.doi.org/10.1016/j.robot.2012.09.014

Gracanin, D., Valavanis, K. P., Tsourveloudis, N. C., & Matijasevic, M. (1999). Virtual-environment-based navigation and control of underwater vehicles. *Robotics & Automation Magazine, IEEE, 6*(2), 53-63. doi: 10.1109/100.774928

Guoqing, X., Li, T., Fengshui, G., Qiang, C., & Jing, L. (2009, 10-13 Feb. 2009). *Design of a hybrid controller for heading control of an Autonomous Underwater Vehicle.* Paper presented at the Industrial Technology, 2009. ICIT 2009. IEEE International Conference on.

Gupta, A., & O'Malley, M. K. (2006). Design of a haptic arm exoskeleton for training and rehabilitation. *Mechatronics, IEEE/ASME Transactions on, 11*(3), 280-289. doi: 10.1109/tmech.2006.875558

Hayward, V., Choksi, J., Lanvin, G., & Ramstein, C. (1994). Design and Multi-Objective Optimization of a Linkage for a Haptic Interface. In J. Lenarčič & B. Ravani (Eds.), *Advances in Robot Kinematics and Computational Geometry* (pp. 359-368): Springer Netherlands.

Hoang, N. Q., & Kreuzer, E. (2007). Adaptive PD-controller for positioning of a remotely operated vehicle close to an underwater structure: Theory and experiments. *Control Engineering Practice, 15*(4), 411-419. doi: http://dx.doi.org/10.1016/j.conengprac.2006.08.002

Horowitz, I. M. (1993). *Quantitative Feedback Design Theory*: QFT Publications.

Hua, M.-D. (2010). Attitude estimation for accelerated vehicles using GPS/INS measurements. *Control Engineering Practice, 18*(7), 723-732. doi: http://dx.doi.org/10.1016/j.conengprac.2010.01.016

Hwang, C., & Yang, S.-F. (2002). QFT template generation for time-delay plants based on zero-inclusion test. *Systems & Control Letters, 45*(3), 179-191. doi: http://dx.doi.org/10.1016/S0167-6911(01)00175-X

Javadi-Moghaddam, J., & Bagheri, A. (2010). An adaptive neuro-fuzzy sliding mode based genetic algorithm control system for under water remotely operated vehicle. *Expert Systems with Applications, 37*(1), 647-660. doi: http://dx.doi.org/10.1016/j.eswa.2009.06.015

Jensen, M. J., Tolbert, A. M., Wagner, J. R., Switzer, F. S., & Finn, J. W. (2011). A Customizable Automotive Steering System With a Haptic Feedback Control Strategy for Obstacle Avoidance Notification. *Vehicular Technology, IEEE Transactions on, 60*(9), 4208-4216. doi: 10.1109/tvt.2011.2172472

Jian, L., Tavakoli, M., & Qi, H. (2014a). Absolute Stability of a Class of Trilateral Haptic Systems. *Haptics, IEEE Transactions on, 7*(3), 301-310. doi: 10.1109/toh.2014.2321616

Jian, L., Tavakoli, M., & Qi, H. (2014b). Absolute Stability of Multi-DOF Multilateral Haptic Systems. *Control Systems Technology, IEEE Transactions on, 22*(6), 2319-2328. doi: 10.1109/tcst.2014.2301840

Jian, L., Tavakoli, M., & Qi, H. (2014c). Stability of cooperative teleoperation using haptic devices with complementary degrees of fr. *Control Theory & Applications, IET, 8*(12), 1062-1070. doi: 10.1049/iet-cta.2013.0522

Jong-Ho, H., Kyung-Wook, N., & Jang-Myung, L. (2012, 26-28 Nov. 2012). *PD-Fuzzy control for the velocity of mobile robot using the haptic joystick.* Paper presented at the Ubiquitous Robots and Ambient Intelligence (URAI), 2012 9th International Conference on.

Jung Keun, L., & Park, E. J. (2009). Minimum-Order Kalman Filter With Vector Selector for Accurate Estimation of Human Body Orientation. *Robotics, IEEE Transactions on, 25*(5), 1196-1201. doi: 10.1109/tro.2009.2017146

Jung Keun, L., Park, E. J., & Robinovitch, S. N. (2012). Estimation of Attitude and External Acceleration Using Inertial Sensor Measurement During Various Dynamic Conditions. *Instrumentation and Measurement, IEEE Transactions on, 61*(8), 2262-2273. doi: 10.1109/tim.2012.2187245

Ken, T., An, E., & Beaujean, P. J. (2012). A Robust Fuzzy Autonomous Underwater Vehicle (AUV) Docking Approach for Unknown Current Disturbances. *Oceanic Engineering, IEEE Journal of, 37*(2), 143-155. doi: 10.1109/joe.2011.2180058

Khatib, O. (1985, Mar 1985). *Real-time obstacle avoidance for manipulators and mobile robots.* Paper presented at the Robotics and Automation. Proceedings. 1985 IEEE International Conference on.

Khoa Duy, L., Hung Duc, N., Ranthumugala, D., & Forrest, A. (2014, 3-5 Dec. 2014). *Haptic driving system for surge motion control of underwater remotely operated vehicles.* Paper presented at the Modelling, Identification & Control (ICMIC), 2014 Proceedings of the 6th International Conference on.

Kim, J., & Chung, W. K. (2006). Accurate and practical thruster modeling for underwater vehicles. *Ocean Engineering, 33*(5–6), 566-586. doi: http://dx.doi.org/10.1016/j.oceaneng.2005.07.008

Kinsey, J. C., Eustice, R. M., & Whitcomb, L. L. (2006). *A Survey of Underwater Vehicle Navigation: Recent Advances and New Challenges.* Paper presented at the In Proceedings of the IFAC Conference of Manoeuvering and Control of Marine Craft.

Kinsey, J. C., Qingjun, Y., & Howland, J. C. (2014). Nonlinear Dynamic Model-Based State Estimators for Underwater Navigation of Remotely Operated Vehicles. *Control Systems Technology, IEEE Transactions on, 22*(5), 1845-1854. doi: 10.1109/tcst.2013.2293958

Koren, Y., & Borenstein, J. (1991, 9-11 Apr 1991). *Potential field methods and their inherent limitations for mobile robot navigation.* Paper presented at the Robotics and Automation, 1991. Proceedings., 1991 IEEE International Conference on.

Kurtz, R., & Hayward, V. (1992). Multiple-goal kinematic optimization of a parallel spherical mechanism with actuator redundancy. *Robotics and Automation, IEEE Transactions on, 8*(5), 644-651. doi: 10.1109/70.163788

Lam, T. M. (2009). *Haptic Interface for UAV Teleoperation.* (Doctor of Philosophy), Delft University of Technology.

Lam, T. M., Boschloo, H. W., Mulder, M., & van Paassen, M. M. (2009). Artificial Force Field for Haptic Feedback in UAV Teleoperation. *Systems, Man and Cybernetics, Part A: Systems and Humans, IEEE Transactions on, 39*(6), 1316-1330. doi: 10.1109/tsmca.2009.2028239

LE, K., NGUYEN, H., & RANMUTHUGALA, S. (2013b). *Development and modelling of a three-thurster remotely operated vehicle using open source hardware.* Paper presented at the Proceedings of The 17th International Conference On Mechatronics Technology, Jeju Island, Korea.

Le, K. D., Hung Duc, N., Ranthumugala, D., & Forrest, A. (2014, 3-5 Dec. 2014). *Haptic driving system for surge motion control of underwater remotely operated vehicles.* Paper presented at the Modelling, Identification & Control (ICMIC), 2014 Proceedings of the 6th International Conference on.

Le, K. D., Nguyen, H. D., & Ranmuthugala, D. (2013). *A Self-tuning Nonlinear PID Controller for a Three-Thruster Remotely Operated Underwater Vehicle.* Paper presented at the Proceedings of the Second Vietnam Conference on Control and Automation, Da Nang, Vietnam.

Le, K. D., Nguyen, H. D., & Ranmuthugala, D. (2014). Design, modelling and simulation of a remotely operated vehicle – Part 2. *Journal of Computer Science and Cybernetics, 30*(2), 106-116.

Le, K. D., Nguyen, H. D., & Ranmuthugala, D. (2015). Development and control of a low-cost, three-thruster, remotely operated underwater vehicle. *International Journal of Automation Technology, 9*(1), 67-75.

Le, K. D., Nguyen, H. D., Ranmuthugala, D., & Forrest, A. (2015). A heading observer for ROVs under roll and pitch oscillations and acceleration disturbances using low-cost sensors. *Ocean Engineering, 110, Part A*, 152-162. doi: http://dx.doi.org/10.1016/j.oceaneng.2015.10.020

Lee, S., Sukhatme, G., Kim, G., & Park, C. (2005). Haptic Teleoperation of a Mobile Robot: A User Study. *Presence, 14*(3), 345-365. doi: 10.1162/105474605323384681

Li, Y., Zhang, Y., Ye, X., & Zhang, S. (2015). An optimization method for penalty-based six-degrees-of-freedom haptic rendering system. *Signal Processing: Image Communication, 39, Part C*, 467-472. doi: http://dx.doi.org/10.1016/j.image.2015.03.011

Lin, Q., & Kuo, C. (1998). A virtual environment-based system for the navigation of underwater robots. *Virtual Reality, 3*(4), 267-277. doi: 10.1007/bf01408707

Luinge, H. J., & Veltink, P. H. (2005). Measuring orientation of human body segments using miniature gyroscopes and accelerometers. *Medical and Biological Engineering and Computing, 43*(2), 273-282. doi: 10.1007/bf02345966

Mahony, R., Hamel, T., & Pflimlin, J.-M. (2008). Nonlinear Complementary Filters on the Special Orthogonal Group. *Automatic Control, IEEE Transactions on, 53*(5), 1203-1218. doi: 10.1109/tac.2008.923738

Martin, P., & Salaün, E. (2010). Design and implementation of a low-cost observer-based attitude and heading reference system. *Control Engineering Practice, 18*(7), 712-722. doi: http://dx.doi.org/10.1016/j.conengprac.2010.01.012

Marzbanrad, A. R., Eghtesad, M., & Kamali, R. (2011, 12-15 Dec. 2011). *A robust adaptive fuzzy sliding mode controller for trajectory tracking of ROVs.* Paper presented at the Decision and Control and European Control Conference (CDC-ECC), 2011 50th IEEE Conference on.

McVicker, W., Forrester, J., Gambin, T., Lehr, J., Wood, Z. J., & Clark, C. M. (2012, 11-14 Dec. 2012). *Mapping and visualizing ancient water storage systems with an ROV — An approach based on fusing stationary scans within a particle filter.* Paper presented at the Robotics and Biomimetics (ROBIO), 2012 IEEE International Conference on.

Meli, L., Pacchierotti, C., & Prattichizzo, D. (2014). Sensory Subtraction in Robot-Assisted Surgery: Fingertip Skin Deformation Feedback to Ensure Safety and Improve Transparency in Bimanual Haptic Interaction. *Biomedical Engineering, IEEE Transactions on, 61*(4), 1318-1327. doi: 10.1109/tbme.2014.2303052

Metni, N., Pflimlin, J.-M., Hamel, T., & Souères, P. (2006). Attitude and gyro bias estimation for a VTOL UAV. *Control Engineering Practice, 14*(12), 1511-1520. doi: http://dx.doi.org/10.1016/j.conengprac.2006.02.015

Moreira, L., & Soares, C. G. (2008). H2 and H infinity Designs for Diving and Course Control of an Autonomous Underwater Vehicle in Presence of Waves. *Oceanic Engineering, IEEE Journal of, 33*(2), 69-88. doi: 10.1109/joe.2008.918689

Morgado, M., Oliveira, P., Silvestre, C., & Fernandes Vasconcelos, J. (2014). Embedded Vehicle Dynamics Aiding for USBL/INS Underwater Navigation System. *Control Systems Technology, IEEE Transactions on, 22*(1), 322-330. doi: 10.1109/tcst.2013.2245133

Nag, A., Patel, S. S., & Akbar, S. A. (2013, 22-23 March 2013). *Fuzzy logic based depth control of an autonomous underwater vehicle.* Paper presented at the Automation, Computing, Communication, Control and Compressed Sensing (iMac4s), 2013 International Multi-Conference on.

Nair, R. R., Behera, L., Kumar, V., & Jamshidi, M. (2014). Multisatellite Formation Control for Remote Sensing Applications Using Artificial Potential Field and Adaptive Fuzzy Sliding Mode Control. *Systems Journal, IEEE, PP*(99), 1-11. doi: 10.1109/jsyst.2014.2335442

Nakao, M., Oyama, H., Komori, M., Matsuda, T., Sakaguchi, G., Komeda, M., & Takahashi, T. (2002). Haptic reproduction and interactive visualization of a beating heart for cardiovascular surgery simulation. *International Journal of Medical Informatics, 68*(1-3), 155-163.

Natori, K., Tsuji, T., Ohnishi, K., Hace, A., & Jezernik, K. (2010). Time-Delay Compensation by Communication Disturbance Observer for Bilateral Teleoperation Under Time-Varying Delay. *Industrial Electronics, IEEE Transactions on, 57*(3), 1050-1062. doi: 10.1109/tie.2009.2028337

Nguyen, H. D., Malalagama, S., & Ranmuthugala. (2012). *Modelling and Simulation of a Remotely Operated Vehicle*. Paper presented at the Vietnam Conf. on Mechatronics, Vietnam.

Nguyen, H. D., Malalagama, S., & Ranmuthugala, D. (2013). Design, Modelling and Simulation of a Remotely Operated Vehicle-Part 1. *Journal of Computer Science and Cybernetics, 29*(4), 299-312.

Nguyen Trong, T., & Kyoung Kwan, A. (2012). Output Feedback Direct Adaptive Controller for a SMA Actuator With a Kalman Filter. *Control Systems Technology, IEEE Transactions on, 20*(4), 1081-1091. doi: 10.1109/tcst.2011.2158435

Oblak, J., Cikajlo, I., & Matjacic, Z. (2010). Universal Haptic Drive: A Robot for Arm and Wrist Rehabilitation. *Neural Systems and Rehabilitation Engineering, IEEE Transactions on, 18*(3), 293-302. doi: 10.1109/tnsre.2009.2034162

Pe, x, rez-D'Arpino, C., Vigouroux, D., Medina, M., x, . . . pez, G. (2011, 11-12 April 2011). *Development of a low cost inertial measurement unit for UAV applications with Kalman Filter based attitude determination.* Paper presented at the Technologies for Practical Robot Applications (TePRA), 2011 IEEE Conference on.

Petrich, J., & Stilwell, D. J. (2011). Robust control for an autonomous underwater vehicle that suppresses pitch and yaw coupling. *Ocean Engineering, 38*(1), 197-204. doi: http://dx.doi.org/10.1016/j.oceaneng.2010.10.007

Podobnik, J., & Munih, M. (2007). Haptic Interaction Stability With Respect to Grasp Force. *Systems, Man, and Cybernetics, Part C: Applications and Reviews, IEEE Transactions on, 37*(6), 1214-1222. doi: 10.1109/tsmcc.2007.905816

Polushin, I. G., & Hasan, M. Z. (2014). L2 stability of haptic systems with projection-based force reflection. *Haptics, IEEE Transactions on, 7*(3), 405-410. doi: 10.1109/toh.2014.2305437

Poty, A., Melchior, P., & Oustaloup, A. (2004, 2004). *Dynamic path planning for mobile robots using fractional potential field.* Paper presented at the Control, Communications and Signal Processing, 2004. First International Symposium on.

Roberts, A., & Tayebi, A. (2013). A new position regulation strategy for VTOL UAVs using IMU and GPS measurements. *Automatica, 49*(2), 434-440. doi: http://dx.doi.org/10.1016/j.automatica.2012.10.009

Roberts, G. N., & Sutton, R. (2006). *Advances in unmanned marine vehicles*. London, United Kingdom: Institution of Engineering and Technology.

Rösch, O. J., Schilling, K., & Roth, H. (2002). Haptic interfaces for the remote control of mobile robots. *Control Engineering Practice, 10*(11), 1309-1313. doi: http://dx.doi.org/10.1016/S0967-0661(02)00153-3

Ryu, D., Song, J.-B., Cho, C., Kang, S., & Kim, M. (2010). Development of a six DOF haptic master for teleoperation of a mobile manipulator. *Mechatronics, 20*(2), 181-191. doi: http://dx.doi.org/10.1016/j.mechatronics.2009.11.003

Sangyoon, L., Sukhatme, G., Jounghyun, K., & Chan-Mo, P. (2002, 2002). *Haptic control of a mobile robot: a user study.* Paper presented at the Intelligent Robots and Systems, 2002. IEEE/RSJ International Conference on.

Saravanakumar, S., & Asokan, T. (2013). Multipoint potential field method for path planning of autonomous underwater vehicles in 3D space. *Intell. Serv. Robot., 6*(4), 211-224. doi: 10.1007/s11370-013-0138-2

Sastry, S. S., & Isidori, A. (1989). Adaptive control of linearizable systems. *Automatic Control, IEEE Transactions on, 34*(11), 1123-1131. doi: 10.1109/9.40741

Scaradozzi, D., Conte, G., & Sorbi, L. (2012, 3-6 July 2012). *Assisted guidance system for Micro ROV in underwater data gathering missions.* Paper presented at the Control & Automation (MED), 2012 20th Mediterranean Conference on.

Schirmbeck, E. U., Haßelbeck, C., Mayer, H., Nágy, I., Knoll, A., Freyberger, F. K. B., . . . Bauernschmitt, R. (2005). Evaluation of haptic in robotic heart surgery. *International Congress Series, 1281,* 730-734. doi: http://dx.doi.org/10.1016/j.ics.2005.03.037

Siegwart, R., Nourbakhsh, I. R., & Scaramuzza, D. (2011). *Introduction to Autonomous Mobile Robots*: MIT Press.

Smallwood, D. A., & Whitcomb, L. L. (2004). Model-based dynamic positioning of underwater robotic vehicles: theory and experiment. *Oceanic Engineering, IEEE Journal of, 29*(1), 169-186. doi: 10.1109/joe.2003.823312

Snyder, J. (2010, 20-23 Sept. 2010). *Doppler Velocity Log (DVL) navigation for observation-class ROVs.* Paper presented at the OCEANS 2010.

Srisertpol, J., & Khajorntraidet, C. (2009, 17-19 June 2009). *Estimation of DC motor variable torque using adaptive compensation.* Paper presented at the Control and Decision Conference, 2009. CCDC '09. Chinese.

Steinke, D. M., & Buckham, B. J. (2005, 2005). *A Kalman filter for the navigation of remotely operated vehicles.* Paper presented at the OCEANS, 2005. Proceedings of MTS/IEEE.

Suh, Y.-S., Park, S.-K., Kang, H.-J., & Ro, Y.-S. (2006). Attitude Estimation Adaptively Compensating External Acceleration. *JSME International Journal Series C Mechanical Systems, Machine Elements and Manufacturing, 49*(1), 172-179. doi: 10.1299/jsmec.49.172

Tao, G. (2004). *Adaptive Control Design and Analysis*: John Wiley & Sons.

Thanh, T. U. D. C., & Ahn, K. K. (2006). Nonlinear PID control to improve the control performance of 2 axes pneumatic artificial muscle manipulator using neural network. *Mechatronics, 16*(9), 577-587. doi: http://dx.doi.org/10.1016/j.mechatronics.2006.03.011

Vasconcelos, J. F., Cardeira, B., Silvestre, C., Oliveira, P., & Batista, P. (2011). Discrete-Time Complementary Filters for Attitude and Position Estimation: Design, Analysis and Experimental Validation. *Control Systems Technology, IEEE Transactions on, 19*(1), 181-198. doi: 10.1109/tcst.2010.2040619

Vlachos, K., & Papadopoulos, E. (2006). Transparency maximization methodology for haptic devices. *Mechatronics, IEEE/ASME Transactions on, 11*(3), 249-255. doi: 10.1109/tmech.2006.875561

Wang, J.-S., & Lee, C. S. G. (2003). Self-adaptive recurrent neuro-fuzzy control of an autonomous underwater vehicle. *Robotics and Automation, IEEE Transactions on, 19*(2), 283-295. doi: 10.1109/tra.2003.808865

Warsi, F. A., Hazry, D., Ahmed, S. F., Joyo, M. K., Tanveer, M. H., Kamarudin, H., & Razlan, Z. M. (2014, 7-9 March 2014). *Yaw, Pitch and Roll controller design for fixed-wing UAV under uncertainty and perturbed condition.* Paper presented at the Signal Processing & its Applications (CSPA), 2014 IEEE 10th International Colloquium on.

Yoerger, D. R., Newman, J., & Slotine, J. J. E. (1986). Supervisory control system for the JASON ROV. *Oceanic Engineering, IEEE Journal of, 11*(3), 392-400. doi: 10.1109/joe.1986.1145191

Young-Soo, S. (2010). Orientation Estimation Using a Quaternion-Based Indirect Kalman Filter With Adaptive Estimation of External Acceleration. *Instrumentation and Measurement, IEEE Transactions on, 59*(12), 3296-3305. doi: 10.1109/tim.2010.2047157

Yun, X., & Bachmann, E. R. (2006). Design, Implementation, and Experimental Results of a Quaternion-Based Kalman Filter for Human Body Motion Tracking. *Robotics, IEEE Transactions on, 22*(6), 1216-1227. doi: 10.1109/tro.2006.886270

Zhang, X., Li, L., & Yang, J. (2014). Study on Underwater Dual-Laser Structured-Light System for ROV Guiding. *International Journal of Automation Technology, 8*(4), 584-591.

Zhenying, G. (2012). *3D locomotion Biomimetic Robot Fish with Haptic Feedback.* (Research doctorate), Deakin University.

Appendix I: Development and Modelling of a Three-Thruster Remotely Operated Vehicle Using Open Source Hardware

The appendix provides the supporting information for Chapter 2 - Part A. The appendix has been published in the Proceedings of the 17th International Conference on Mechatronics Technology (2013). The citation for the research article is

Le, KD and Nguyen, HD and Ranmuthugala, SD, *Development and modelling of a three-thruster remotely operated vehicle using open source hardware*, Proceedings of The 17th International Conference On Mechatronics Technology, 15-18 October 2013, Jeju Island, Korea, pp. 1-6. (2013)